UNIVERSITA' DEGLI STUDI DI NAPOLI FEDERICO II

Ph. D. thesis in Chemical Engineering

(XXIII cycle)

FUEL PROCESSOR - PEM FUEL CELL SYSTEMS FOR ENERGY GENERATION

Tutors:

Prof. Piero Salatino

Ing. Marino Simeone

Ph.D. Student:

Ing. Laura Menna

Scientific Commitee

Prof. Gennaro Volpicelli

Prof. Andrea D'Anna

Prof. Riccardo Chirone

The Ph.D. Research Program will focus on pure hydrogen production for clean energy generation on small and medium scale. During the first year of the Ph.D. a detailed analysis of literature on the processes available for pure hydrogen production was performed, identifying the main issues, both in the experimental and modeling field. The second year was dedicated to system analysis of hydrogen production units coupled with PEM fuel cells. The third year has been employed to develop a detailed mathematical model of catalytic reactors integrated with high selective hydrogen membranes for pure hydrogen production.

Summary

In the last few years, increasing attention has been paid to fuel cell, as alternative energy generation system; the increasing energy demand and the depletion of fossil fuels, indeed, have pushed researchers' effort toward the development of new energy systems and fuel cell represent sustainable and valid way for high quality energy generation in a wide range of applications, from portable and residential scale to stand-alone and automotive applications.

Of all the fuel cell systems, PEM fuel cells fed with hydrogen are the most promising device for decentralized energy production, both in stationary and automotive field, thanks to high compactness, low weight (high power-to-weight ratio), high modularity, good efficiency and fast start-up and response to load changes. The high efficiencies that can be obtained with a PEM fuel cell, however, require a high purity hydrogen feed at the anode. Hydrogen, though, is not a primary source, but it is substantially an energy carrier, that can be stored, transported and employed as gaseous fuel, however, it needs to be produced from other sources. The main hydrogen source is actually represented by hydrocarbons, through classical Steam Reforming or Partial Oxidation process.

However, hydrogen distribution from industrial production plants to small-scale users meets some limitations related to difficulties in hydrogen storage and transport. For its chemical and physical properties, indeed, the development of an

hydrogen infrastructure seems to be not feasible in short term, while more reasonable seems to be the concept of decentralized hydrogen production; in this way, the hydrogen source, such as methane, is distributed through pipelines to the small-scale plant, installed nearby the users, and the hydrogen produced in situ is fed directly to the energy production system, avoiding hydrogen storage and transportation. In this sense, research is oriented toward the optimization of the decentralized hydrogen production unit, generally named as fuel processor, for residential and automotive applications, for achieving fuel conversion into hydrogen with high efficiencies and high compactness.

The fuel processors and the integration of fuel processor with a PEM fuel cell is widely studied since there are different configurations, a large variability of operating parameters and the possibility of recovering heat in various sections of the plant, thus increasing system efficiency and/or compactness.

Since the efficiency of the integrated fuel processor – fuel cell system strongly depends on system configuration and on the heat integration, a system analysis of the most promising configurations is performed, in order to identify the best solution for energy production in a PEM fuel cell system. Analysis of global system efficiency of fuel processor – PEM fuel cell systems is performed by means of the software AspenPlus®, with identification of best configuration and best operating conditions.

Moreover, since the application of fuel processor – PEM fuel cell system is foreseen for small and medium scale, an important characteristic that must me associated to the high efficiency is the compactness of the system. The PEM fuel cell, indeed, is generally characterized by high efficiency and compactness, therefore, in order to keep its standard, also the fuel processor coupled with it must be efficient and as compact as possible. The system analysis performed in the first part of the work allows to determine the best configurations in terms of high efficiency, but is based on a thermodynamic approach, imposing that all the units that characterize the fuel processor reach their thermodynamic equilibrium. In order to have an idea of the encumbrance of the reactors, a detailed mathematical model for fixed bed reactors was developed in this work, in order to

size and compare conventional fixed bed reactor and membrane catalytic reactors. The software employed was Mathematica®.

This thesis is organized as it follows:

Chapter 1 - Introduction: details on the PEM fuel cell and on various sections of conventional and membrane-based fuel processors. In particular, section 1.1 describes the fuel cells and gives details on PEM fuel cell, section 1.2 is dedicated to conventional fuel processors, with details on the reforming technologies and on typical CO clean-up technique; section 1.3 is dedicated to membrane reactor technology. The state of art on system analysis and on mathematical model is also presented in section 1.4, followed by the aim of the work.

Chapter 2 – Methodology for the system analysis performed with AspenPlus: description of the fuel processor – PEM fuel cell systems investigated and main hypothesis made to perform the analysis, with details on the evaluation of the energy efficiency and on the simulation of the membrane reactors.

Chapter 3 – Results on the system analysis of the fuel processor – PEM fuel cell systems: this chapter will show the results of the thermodynamic analysis on various configuration of PEM fuel cell systems, investigating the effect of the main operating parameters on the energy efficiency.

Chapter 4 – Results on the system analysis of the fuel processor – PEM fuel cell system fed with ethanol: due to the increasing interest in producing hydrogen from renewable sources, the system analysis was also performed when the fuel is bio-ethanol, in order to have an idea of the effect of the fuel quality on system performance.

Chapter 5 – Development of the mathematical model of fixed bed reactor in Mathematica: details on the development of the model for sizing the reactors that constitute the fuel processor, introduction of the terms and balances related to hydrogen permeation through the membrane and validation of the model both for traditional and membrane reactor.

Chapter 6 – Sizing of the fuel processor: results of the Mathematica model on the sizing of the CO clean-up section for conventional and innovative fuel processor, with the investigation of the main operating parameters and an extensive and detailed comparison of results achieved with AspenPlus.

INDEX

Introduction

1.1 Fuel Cells for energy generation

In the last few years energy generation units based on fuel cells have been extensively studied as valid alternative to common energy generation systems, thanks to their high energy efficiency and high power densities [1].
Despite the high cost, these systems result to be really interesting in the energy field, allowing to generate energy on portable scale, on small and medium scale (cars, boats, domestic) and also on large scale, for distributed power generation.
Fuel cells are electrochemical devices that directly convert chemical energy to electrical energy. They consist of an electrolyte medium sandwiched between two electrodes (Figure 1.1).

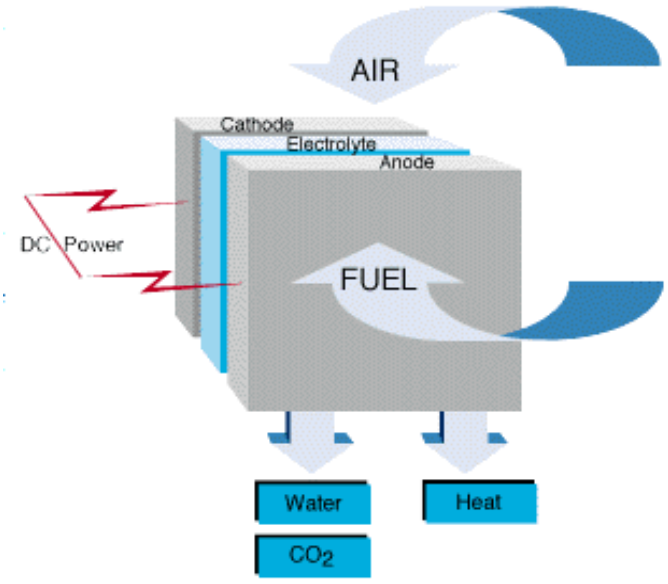

Figure 1.1 Fuel Cell

One electrode (called the anode) facilitates electrochemical oxidation of fuel, while the other (called the cathode) promotes electrochemical reduction of oxidant. Ions generated during oxidation or reduction are transported from one electrode to the other through the ionically conductive but electronically insulating electrolyte. The electrolyte also serves as a barrier between the fuel and oxidant. Electrons generated at the anode during oxidation pass through the external circuit (hence generating electricity) on their way to the cathode, where they complete the reduction reaction. The fuel and oxidant do not mix at any point, and no actual combustion occurs. The fuel cell therefore is not limited by the Carnot efficiency and can yield very high efficiency values. Fuel cells are primarily classified according to the electrolyte material. The choice of electrolyte material also governs the operating temperature of the fuel cell. Table 1.1 lists the various types of fuel cells along with electrolyte used, operating temperature, and electrode reactions.

Fuel Cell	Electrolyte	T (°C)	Reactions
Polymer Electrolyte	Polymer membrane	60 – 140	Anode: $H_2 \rightarrow 2H^+ + 2e^-$ Cathode: $1/2O_2 + 2H^+ + 2e^- \rightarrow H_2O$
Direct Methanol	Polymer membrane	30 – 80	Anode: $CH_3OH + H_2O \rightarrow CO_2 + 6H^+ + 6e^-$ Cathode: $3/2O_2 + 6H^+ + 6e^- \rightarrow 3H_2O$
Alkaline	Potassium Hydroxide	150 – 200	Anodoe: $H_2 + 2OH^- \rightarrow 2H_2O + 2e^-$ Cathode: $1/2O_2 + 2H^+ + 2e^- \rightarrow 2OH^-$
Phosphoric Acid	Phosphoric Acid	180 – 200	Anode: $H_2 \rightarrow 2H^+ + 2e^-$ Cathode $1/2O_2 + 2H^+ + 2e^- \rightarrow H_2O$
Molten Carbonate	Lithium/Potassium Carbonate	600-1000	Anode: $H_2 + CO_3^{2-} \rightarrow H_2O + CO_2 + 2e^-$ Cathode: $1/2O_2 + CO_2 + 2e^- \rightarrow CO_3^{2-}$
Solid Oxide	Yittiria Stabilized Zirconia	1000	Anode: $H_2 + O^{2-} \rightarrow H_2O + 2e^-$ Cathode: $1/2O_2 + 2e^- \rightarrow O_2$

Table 1.1 Classification of fuel cells

The application field and the main advantages of each fuel cell type are reported in Figure 1.2. Each type of fuel cell has its own advantages and disadvantages. For example, alkaline fuel cells allow the use of non precious metal catalysts because of easy oxygen reduction kinetics at high pH conditions, but they suffer for the problem of liquid electrolyte management and electrolyte degradation. Similarly, molten carbonate fuel cells can tolerate high concentrations of carbon monoxide in the fuel stream (CO is a fuel for such fuel cells), but their high operating temperature precludes rapid start-up and sealing remains an issue. Solid oxide fuel cells offer high performance, but issues such as slow start-up and interfacial thermal conductivity mismatches must be addressed. High cost is an issue that affects each type of fuel cell.

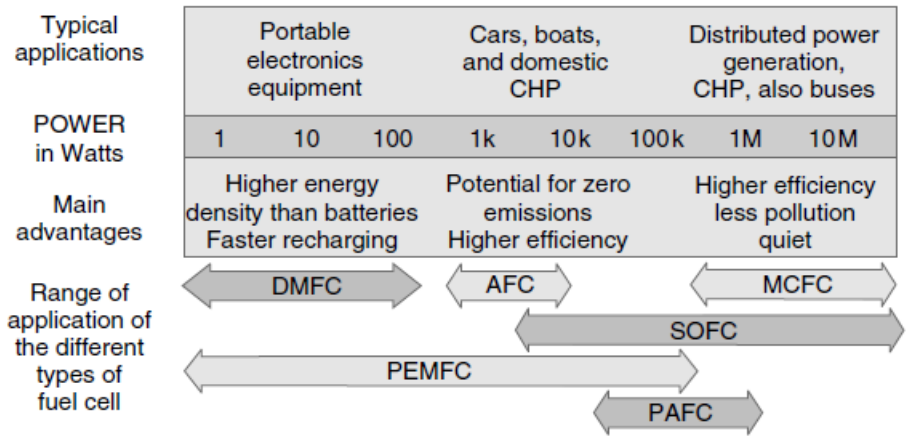

Figure 1.2 Applications and main advantages of fuel cells of different types and in different applications

PEM fuel cell

The PEM fuel cell is unique since it is the only kind of low temperature fuel cell that uses a solid electrolyte, usually a polymer electrolyte membrane (PEM) and it has been extensively studied for its simplicity and its high efficiency; as for the other fuel cells, PEM fuel cell shows a very high energy efficiency when the fuel fed to the anode is represented by pure hydrogen.

In a PEMFC unit, hydrogen is supplied at one side of the membrane where it is split into hydrogen protons and electrons, at anode electrode:

$H_2 \rightarrow 2H^+ + 2e^-$

The protons permeate through the polymeric membrane to the reach the cathode electrode, where oxygen is supplied and the following reactions takes place.

$O_2 + 4H^+ + 4e^- \rightarrow 2H_2O$

Electrons circulate in an external electric circuit under a potential difference.
The electric potential generated in a single unit is about 0.9V. To achieve a higher voltage, several membrane units need to be connected in series, forming a fuel cell stack. The electrical power output of the fuel cell is about 60% of its energy generation, the remaining energy is released as heat.
Generally, oxygen is fed to the cathode as an air stream; in practical systems, an excess of oxygen is fed to the cathode to avoid extremely low concentration at the exit. Frequently, a 50% or higher excess with respect to the stoichiometric oxygen is fed to the cathode.
For the anode, instead, it is not typically the stoichiometric ratio, but rather the amount of hydrogen converted to the fuel cell as a percentage of the hydrogen present in the feed that is specified. This amount is named as the hydrogen utilization factor U_f; when pure hydrogen is fed to the PEMFC, this factor can be assumed equal to unity. For PEMFC systems running on reformate produced in a conventional fuel processor, this factor can be assumed equal to 0.8. This implies that not all gas fed to the anode is converted and unconverted hydrogen and the rest of the reformate is purged off as a stream named as Anode Off-Gas (AOG). This stream presents a heating value due to the presence of hydrogen and methane, therefore, it can be used in the burner of the conventional fuel processor to eventually supply heat to the process.

1.2 Development of energy systems based on PEM fuel cell

As already said, the PEM fuel cell shows high efficiency when fed with pure hydrogen. This represents substantially the main disadvantage of the PEM fuel cell.

Hydrogen, indeed, is not a primary source, but it is substantially an energy carrier, that needs to be produced from other fuels. On industrial scale, hydrogen production is a mature technology, based on Steam Reforming of low molecular weight hydrocarbon or on Partial Oxidation of high molecular weight hydrocarbon.

For small scale energy generation, a system of storage and transportation of hydrogen should be designed and associated to the fuel cell energy system; however, although there are studies related to the optimization of hydrogen transportation techniques, the chemico-physical properties of hydrogen hinder the possibility of diffusing the PEM fuel cell systems for energy generation in the short-term market.

For this reason, a more reasonable solution is represented by decentralized hydrogen production, with a hydrogen generation system placed near-by the PEM fuel cell. The hydrogen generation system must be a compact and efficient unit, or a series of units, that process a fuel, such as methane, to produce hydrogen with low CO content to send to the PEM fuel cell.

The hydrogen generation systems for decentralized hydrogen production are extensively studied in literature and are generally named as fuel processors.

Consequently, a PEM fuel cell energy generation system for decentralized energy production consists not only of the fuel cell and of its auxiliary units, but also of the fuel processor. Therefore, the optimization of the energy generation system must take into account both units and their interaction.

It is worth noting that, in the short term, the easier hydrogen source is represented by fossil fuels, thanks to the extensive market and to the existing pipelines that allow their transport; on a longer term and to further reduce the utilization of fossil fuels, it would be interesting to employ renewable sources to produce hydrogen in the fuel processor. This solution is under development and many studies are performed on the fuel processors fed with methanol or ethanol produced from biomasses. Of course, improvements in treatment and conversion of biomasses must be done in order to make this solution competitive on the market.

As regards the fuel processors, there are substantially two kinds of fuel processors in literature: a conventional fuel processor and an innovative one. The details of each kind is reported in the following paragraphs.

1.3 Conventional Fuel Processors

Figure 1.3 shows the scheme of a conventional fuel processor for hydrogen production from methane, that consists of a desulfurization unit (Des), a syngas production section and a CO clean-up section.

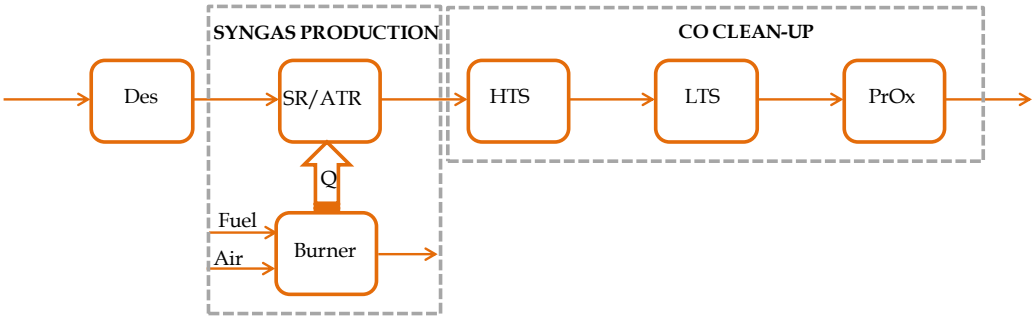

Figure 1.3 Conventional Fuel Processor

In the following, the detailed description of the syngas production technologies and of the conventional CO clean-up section is reported. In order to complete the picture of the fuel processor, a brief paragraph on the Desulfurization section is also reported, although it was not considered in this work.

1.3.1 Desulfurization unit

Sulfur is a poison for nickel steam reforming catalysts and for the platinum anode catalyst in the fuel cell. Tipically, the levels need to be reduced to 0.2 ppm or lower [2].

There are two basic approaches for fuel desulfurization:

1. Passive adsorption
2. Catalytic transformation, followed by adsorption

The passive adsorption approach uses zeolites, metal impregnated carbons, and aluminas to remove the organic and inorganic sulfur compounds at ambient

pressure and temperature [3]. Its simplicity is attractive since it requires little up front capital investment in the reformer design. However, sulfur adsorption capacities are low, typically less than 2 g S/100 g adsorbent for natural gas and less than 1 g S/100 g for Liquefied Petroleum Gas LPG. This requires large adsorption inventories and frequent change-outs. Also, since they accumulate heavier hydrocarbons, the spent adsorbents are hazardous and require special handling. The catalytic-adsorption approach is attractive because of the lower maintenance costs and size. This is due to its greater sulfur adsorption capacities. However, it does require higher up-front capital investment to accommodate the required reagent addition and heating of the fuel. The catalytic-adsorption approach most often used is hydrodesulfurization (HDS). This is where hydrogen added to the fuel reacts with the sulfur compounds to form H_2S. The process uses a HDS catalyst, typically Ni-Mo/Al_2O_3 or Co-Mo/Al_2O_3, followed by H_2S adsorption on zinc oxide at a temperature of 300–400 °C. For HDS of liquid fuels, hydrogen partial pressures of 1000 to 2000 kPa and temperatures of 300–400 °C are required. Because the sulfur compounds in natural gas and LPG are non-aromatic and of low molecular weight, HDS can be performed at lower H_2 partial pressures, 1 to 10 kPa, and temperatures of 200–400 °C depending on the catalyst and the sulfur speciation. Zinc oxide adsorption capacities for H_2S in industrial applications are reported to be high, typically 15–20 g S/100 g adsorbent. This is higher than passive adsorbents, thus lowering inventories of adsorbent and decreasing adsorbent replacement frequency. HDS requires adding hydrogen, which is recycled from one of the post-reformer points in the process. An additional drawback is the nature of the catalysts themselves. HDS catalysts require activation using a H_2S–H_2 mixture, and they contain priority pollutant metals (e.g. Ni, Co, and Mo) that require special handling and disposal. Engelhard [2] has developed a new catalytic-adsorption fuel desulfurization technology (Selective Catalytic Oxidation SCO) that does not require hydrogen recycle and whose by-products are non-hazardous. This technology combines the fuel with a sub-stoichiometric amount of oxygen (from air) and uses a sulfur tolerant monolith catalyst to oxidize selectively the sulfur compounds to sulfur oxides

(SO_2 and SO_3) that are then adsorbed downstream by an inexpensive high capacity particulate adsorbent.

This technology, though, is still in development, and conventional fuel processors foresees sulfur elimination through HDS technology. In particular, Li et al. [4] reported a study on ZnO performance with typical fuel processor operating conditions, placing the adsorbent unit downstream the syngas production unit. In this way, the unit where S is converted to H_2S is absent, since it is integrated inside the syngas production unit. The authors found that the adsorbent bed must be operated in a temperature range of 250-350 °C, depending on feed composition, as a balance between kinetics and thermal deactivation.

1.3.2 Syngas production unit

As described earlier, there are essentially three main syngas production technologies:

- ✓ Steam Reforming (SR)
- ✓ Partial Oxidation (PO)
- ✓ Autothermal Reforming (ATR)

When heavier hydrocarbons are used, industrial scale syngas production is made by feeding the hydrocarbon and oxygen in adiabatic reactor, without using catalysts. In this way, hydrocarbon feedstock is oxidized to produce CO and H_2 through exothermic reactions, meaning that no indirect heat is required for the reactions to take place. In industrial plants, catalysts are not required due to high temperature being reached. In recent years many researchers have given their attention to catalytic partial oxidation (CPO) for decentralized hydrogen production. Operating with catalysts, it is possible to conduct partial oxidation at lower temperature than thermal partial oxidation, allowing the use of air instead of oxygen, and with reactors of reduced size, since the reaction rate highly increases thanks to catalyst action.

Autothermal Reforming technology, instead, is conducted in adiabatic reactors, by adding steam to the PO mixture; generally, oxygen is furnished by feeding air, since an oxygen separation plant would require high cost and would increase too

much the fuel processor size. In autothermal process, there is a first zone where exothermic reactions take place, followed by a catalytic zone where reforming endothermic reactions take place. As for PO, the heat required for sustaining the process is generated inside the reactor itself.

The main characteristics of the three existing reforming technologies are reported in the following section, since the syngas production unit represents the first and most important step for hydrogen generation, both in terms of size and of energy demand. Therefore, extensive thermodynamic analysis performed in hydrogen production processes are present in literature, in order to analyze the equilibrium product composition, maximizing hydrogen yield and minimizing the CO one.

Steam Reforming

The Steam Reforming process is the most common industrial and small scale technology for hydrogen production, in particular when light hydrocarbons, such as methane, are used as hydrogen sources [5-8]. SR is made by feeding methane and steam to a Ni-based catalyst, where hydrogen is generated according to the following reactions:

$CH_4 + H_2O = CO + 3H_2$ $\quad\quad$ $\Delta H^o_R = 49$ Kcal/mol CH_4

$CO + H_2O = CO_2 + H_2$ $\quad\quad$ $\Delta H^o_R = -9.8$ Kcal/mol CO

$CH_4 = C + 2H_2$ $\quad\quad$ $\Delta H^o_R = 18$ Kcal/ mol CH_4

The process is globally endothermic and happens with an increase in mole number; thus, a thermodynamic analysis shows that hydrogen production is promoted at high temperature (T), low pressures (P) and high steam to methane ratio (S/C). Due to endothermicity of SR reaction, an external energy input is required; this imposes the employment of heat-exchange reactors: in industrial plants, methane and steam are fed into catalyst filled tubes, placed inside large combustion chambers, where methane combustion release the heat for the endothermic SR reaction; generally, methane and air are fed to the burners in co-current with respect to the SR feeding mixture; in this way, temperatures not above 800 °C are allowed for the process.

Steam Reforming process has got a number of disadvantages in terms of high cost and low compactness, for the presence of the external combustion chamber and of many heat exchangers for heat recovery. Moreover, the SR reactor requires high residence times for methane conversion to approach to equilibrium values. However, higher syngas yields are obtained with respect to autothermal processes, since heat generation is external to the reactor.

Steam Reforming thermodynamic is regulated substantially by two main parameters, that is operating temperature and steam to methane ratio (S/C); this parameters must be optimized in order to obtain high hydrogen yields, high methane conversion and absence of coke formation. Even if high temperature would let practically complete methane conversion, a general goal is to achieve a conversion which is as high as possible within allowable operating conditions; in many cases, if the conversion approaches a value of 1, this could damage the durability of the reactor system. The durability of the reformer is governed by thermal durability of the reforming catalysts and the deactivation of catalyst by coke formation. For this reason, SR temperatures generally don't exceed 750-800 °C.

A work of Y.S. Seo et al. [9] describes the effect of reformer temperature and of S/C on process performance, trough Aspen Plus^{TM} software. The temperature and S/C values that maximize hydrogen production and reduce CO formation are determined, imposing equilibrium at the reactor outlet; the following species are present at equilibrium conditions: CH_4, CO, H_2, C, H_2O, CO_2, where C refers to solid carbon (graphite), while radicals are not considered because the concentration of radicals is found to be negligible compared with those of other products. The authors found that reactor temperature significantly affects equilibrium compositions; as the reactor temperature is raised from 600 °C to 800 °C, the conversion increases from 0.56 to 0.9. If the operating temperature of the reactor is limited to less than 800 °C in order to guarantee thermal durability of the catalyst, it is difficult to obtain conversions higher than 0.99. Reactor temperature also affects the formation of solid carbon; results show that coke formation can be avoided by operating with S/C greater than 1.4. Moreover, an increase in S/C generate and increase in hydrogen flux, with a decrement in CO

production. Though, an increase in S/C means an increase in costs and reactor size. A conversion of 0.99 at 800 °C without carbon formation can be attained by operating at S/C>1.9.

As described earlier, conventional fuel processors for residential applications are based on Steam Reforming technology, since the low compactness due to the external burner presence is compensated for the high efficiencies attainable thanks to high hydrogen content in the reformate stream and to the possibility of recycling the Anode Off-Gas.
In literature, a high number of studies is present on catalyst formulation for improving thermal stability of Ni catalyst, as well as its resistance to sulfur poisoning [12-14]. Many works, instead, focus on the reactor configuration, in order to reduce the system size, though the external heat adduction cannot be avoided [10, 15-17].

Partial Oxidation

Since the SR process is highly endothermic, heat for sustaining the process is generated in an external apparatus, making steam reforming a major energy consumer in the chemical industry and resulting in significant emissions of combustion gases. A main problem of steam reforming is that only about half of the heat generated on the combustion side is transferred to the reaction. At a large industrial site, the remaining waste heat can be integrated in the energy network, thus minimizing overall energy losses. This is not possible for decentralized processes, thus limiting the efficiency of SR for hydrogen production. However, this problem can be avoided if the partial oxidation (PO) process is chosen for producing syngas. The PO reaction is mildly exothermic, which opens the possibility for an autothermal process without the support of an additional combustion reaction. The reaction can be conducted non-catalitically, as a pure gas-phase reaction between methane and oxygen, fed in a ration that allows to operate in adiabatic conditions. In the first part of the reactor the oxidative processes take place, generating heat and steam for the subsequent development

of reforming reactions in the second part of the reactor, until thermodynamic equilibrium is reached.

The main parameter in the partial oxidation process is the O_2/CH_4 ratio; methane and oxygen can react as follows:

$$CH_4 + 0.5O_2 = CO + 2H_2$$
$$CH_4 + 2\ O_2 = CO_2 + 2H_2O$$

If the O_2/CH_4 ratio is about 0.5, partial oxidation products are promoted compared to total combustion product, however the achievement of high temperature levels in autothermal operation is hampered; in this way, unreacted methane doesn't react with water, but remains unconverted of tends to form coke. This causes a low syngas yield. In order to reach high temperatures in autothermal mode and, thus, high syngas yields, it is necessary to operate with O_2/CH_4 ratios higher than 0.5; this allows the development of total combustion reactions, with a decrease in selectivity, but also with an increase in reactor temperature level. With the partial oxidation process is possible to solve the problem of external heat adduction, however this process is generally employed only with high hydrocarbons, since there are problems related to high costs of the air separation section, to coke deposition and to the reaction control. This makes PO process unpratical and uneconomical for small-scale applications.

In the work of Y.S. Seo et al. of 2002 [9], a study on PO thermodynamic is presented, with O_2/CH_4 ratio varied over the range 0-1.2; the air ratio is defined as half of the oxygen to methane ratio.

Figure 1.4 shows products equilibrium compositions as a function of air ratio, at feed preheating temperature of 200 °C and a reactor pressure of 1atm.

A coking boundary is present, infact for oxygen to methane ratios higher than 0.6 there is no formation of coke; as it can be observed, hydrogen concentration increases steeply with increasing air ratio, while solid carbon C(s) increases to a peak near an air ratio of 0.1, reduces gradually and finally drops to zero at an air ratio of 0.3. for an air ratio of 0.3, however, the H_2 concentration reduces rapidly with increasing air ratio, which leads to increase in H_2O concentration.

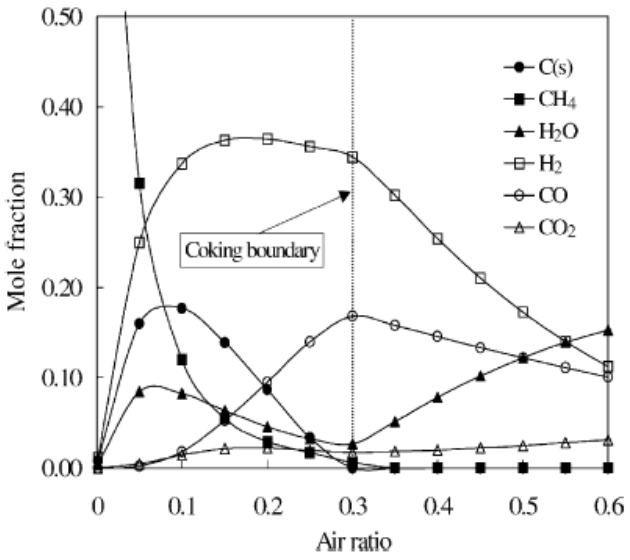

Figure 1.4 Effect of air ratio on product compositions for the PO process. Preheating Temperature = 200 °C, P = 1 bar

The CO also reduces with increasing air ratio, but its decreasing rate is lower than H_2 decreasing rate. The decrease of H_2 and CO is contrary to the original aim of converting methane completely to syngas, therefore operation of PO reactor with an air ratio greater than 0.3 is clearly undesiderable.

Figure 1.5 reports hydrogen yield, methane conversion and adiabatic temperature in the reactor as a function of the air ratio. At the coking boundary (air ratio of 0.3) the behavior of both H_2 yield and adiabatic temperature drastically changes. The H_2 yield increases steadily with the air ratio in the region with the coking, while it decreases for air ratios higher than 0.3, resulting in a lower quality of the reformate stream, that should contain as much hydrogen as possible. The adiabatic temperature rises with increasing air ratio, with a more steeply increase in the region without coke formation.

In recent years many researchers have given their attention to catalytic partial oxidation (CPO) [18-26]. Operating with catalysts, it is possible to conduct partial oxidation at lower temperature than thermal partial oxidation, allowing the use of air instead of oxygen, and with reactors of reduced size, since the reaction rate highly increases thanks to catalyst action.

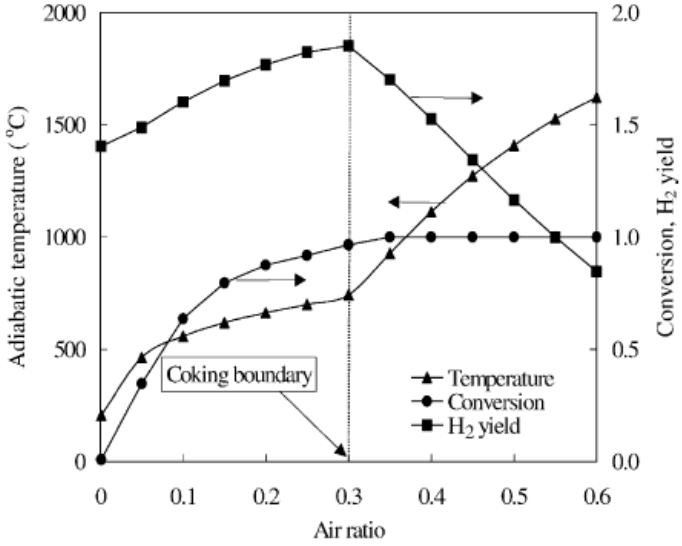

Figure 1.5 Adiabatic temperature, methane conversion and hydrogen yield as a function of air ratio in the PO process. Preheating Temp. = 200 °C; P = 1 bar

Autothermal Reforming

Decentralized hydrogen production and high efficiency due to internal heating supply of autothermal process have pushed researchers effort toward the optimization of the Autothermal Reforming. This process couples catalytic Steam Reforming and Partial Oxidation by feeding methane, water and air to a catalyst bed; in this way, the heat for endothermic reforming reactions is supplied by partial oxidation reactions.

The catalytic ATR, indeed, has received much attention in research during the recent years as a viable process for hydrogen generation for fuel cell systems. It offers advantages of small unit size and low operational temperature, easier start-up, and wider choice of materials. Moreover, ATR has low energy requirements, high gas hourly space velocity (GHSV = Inlet flowrate/Catalyst Volume, hr^{-1}) – at least one order of magnitude relative to SR – and lower process temperature than PO, higher H_2/CO ratio, and easily regulated H_2/CO ratio by the inlet gas composition. Recent works report detailed ATR analysis, in particular for small scale application. Many authors [27-35] have shown than water addition to the PO mixture allows an increase in hydrogen yield together with a decrease in operating temperature (lower thermal stress for the catalyst bed).

In the work of Seo et al. [9], a thermodynamic analysis on autothermal reforming is also presented.

In Figure 1.6 conversion of methane, x, and temperature, T, as a function of air ratio and water to methane ratio S/C are reported. The air ratio significantly affects the conversion and the adiabatic temperature; conversion rapidly increases with the air ratio and reaches 1.0 at an air ratio of 0.3. For air ratios greater than 0.3, the adiabatic temperature continues to increase, although the conversion remains at 1.0; this is due to oxidation of H_2 and CO to H_2O and CO_2 by excessive O_2 supply.

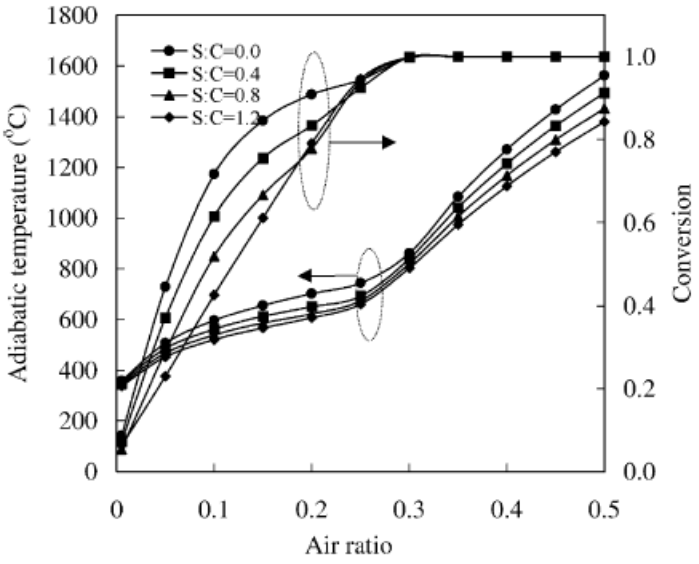

Figure 1.6 Effect of air ratio and S/C ratio on adiabatic reactor temperature and methane conversion in a ATR reactor. Preheating Temp. = 400 °C, P = 1 bar

Results on coke formation show that the coking boundary shifts to lower air ratios when S/C is increased. As an example, the coking boundary moves from an air ratio of 0.3 to an air ratio of 0.2 if S/C is increased from 0.0 to 0.1. For an S/C of 1.2, no coke is generated at any value of the air ratio.

Figure 1.7 shows the effects of air ratio and S/C ratio on product composition. The molar flow rates of H_2 and CO present a peak at an air ratio of 0.25 and 0.3, respectively; as S/C increases, the hydrogen molar flow rates increases, but conversely the CO molar flow rate decreases. This demonstrates that a higher S/C

ratio causes the H_2/CO ratio to increase. On the other hand, if the air ratio is increased above 0.25, the H_2 molar flow drops more steeply than CO molar flow decrement, for the faster oxidation rate of H_2 than CO in the region of high air ratio.

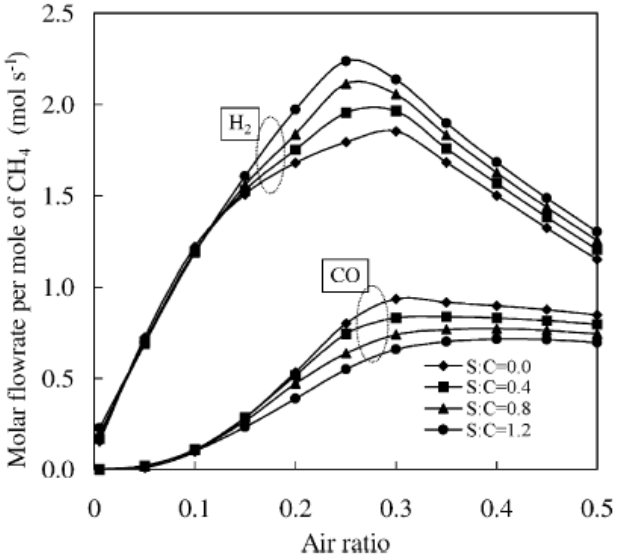

Figure 1.7 Effect of air ratio and S/C ratio on H_2 and CO outlet molar fractions in a ATR reactor. Preheating Temp. = 400 °C; P = 1 bar

1.3.3 CO clean-up section

Concerning to the CO clean-up section, in conventional fuel processors as well as in industrial plants, the first section is represented by Water Gas Shift (WGS) unit. The WGS process is a well-known technology, where the following reaction takes place:

$$CO + H_2O = CO_2 + H_2 \qquad \Delta H^o_R = -9.8 \text{ Kcal/mol CO}$$

WGS is realized in two stages with inter-cooling; in the first high temperature stage (HTS), generally a Fe-Cr based catalyst is employed, active at 380-420 °C; in the second low temperature stage (LTS), a Cu-ZnO catalyst active at 200°C allows further conversion of CO to CO_2. The The necessity of operating the WGS in two stages depends on the conflict between kinetics on catalyst and thermodynamic. Since the reaction is exothermic, an increase in reaction

temperature would shift equilibrium conversion toward the reactants. When the Fe-Cr catalyst is used, since it is not active under 350 °C, the maximum CO conversion attainable would be too low; when Cu-ZnO catalyst is used, feeding the syngas at 200 °C would let a outlet temperature of about 300 °C, due to the heat released from WGS reaction, causing irreversible damages to catalyst itself. Consequently, in industrial plants most of CO is converted in the HTS stage, lowering CO concentration to 3-5%, and the remaining CO is converted in the LTS stage, by cooling the mixture to 200 °C, so a 20-30 °C increment is attained in this stage. The outlet temperature is, therefore, compatible with thermal stability of the LTS catalyst. Even if this technology is quite mature, a number of studies is present in literature, principally on new catalyst formulations based on Au, zeolites, Pt and on monoliths [36-41] for increasing thermal stability and chemical resistance.

The outlet CO concentration is about 0.2-0.5%, thus, a further CO conversion stage must be present before feeding the mixture to a PEM fuel cell. In conventional fuel processors, the CO content lowering to less than 50 ppm is made in the preferential CO Oxidation (PrOx) stage. The reactor is generally adiabatic, and the catalyst and operating temperature choice must be effectuated carefully, in order to promote CO conversion without hydrogen consumption in presence of oxygen. This CO purification technology is mature and well defined, although it has got disadvantage in terms of compactness and catalyst deactivation. A number of studies on PrOx is nowadays oriented toward the development of high active and high selective catalysts [52-51], for reducing H_2 consumption in presence of oxygen and increasing CO oxidation kinetics at low temperature.

1.4 Innovative Fuel Processors

Innovative Fuel Processors are characterized by the employment of a membrane reactor, in which a high selective hydrogen separation membrane is coupled with a catalytic reactor to produce pure hydrogen.

A typical membrane reactor is constituted by two co-axial tubes, with the internal one being the hydrogen separation membrane; generally, the reaction happens in the annulus and the permeate hydrogen flows in the inner tube.

The stream leaving the reaction is named retentate and the stream permeated through the membrane is named permeate.

Membrane reactor is illustrated in Figure 1.8 for the following generic reaction:

$$A + B = C + H_2$$

The membrane continuously removes the H_2 produced in the reaction zone, thus shifting the chemical equilibrium towards the products; this allows to obtain higher conversions of reactants to hydrogen with respect to a conventional reactor, working in the same operating conditions.

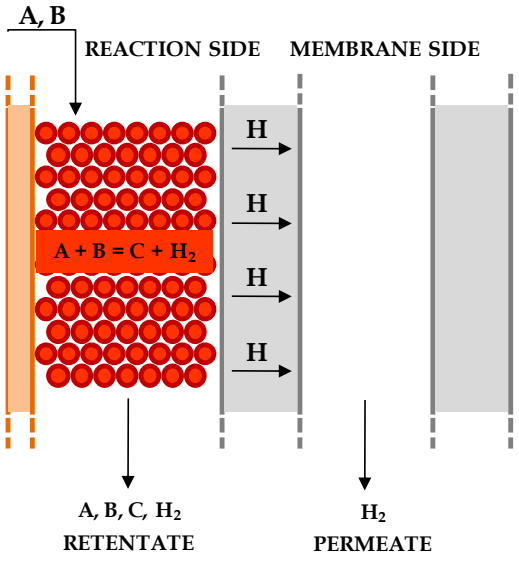

Figure 1.8 Membrane Reactor

A typical membrane used to separate hydrogen from a gas mixture is a Palladium or a Palladium alloy membrane [52]; this kind of membrane is able to separate hydrogen with a selectivity close to 100%. Hydrogen permeation through Palladium membranes happens according to a solution/diffusion mechanism and the hydrogen flux through the membrane, J_{H2} is described by the following law:

$$J_{H2} = \mu_{H2} \cdot \frac{A}{\delta} \cdot \left(\sqrt{P_{H2,R}} - \sqrt{P_{H2,P}} \right)$$

where μ_{H2} is the permeability coefficient [mol/(m^2 s Pa$^{0.5}$)], A is the membrane surface area [m^2], δ is the membrane thickness [m] and $P_{H2,R}$ and $P_{H2,P}$ are hydrogen partial pressures [kPa] on the retentate side and on the permeate side of the membrane, respectively. Eq. 1 is known as Sievert's law and it is valid if the bulk phase diffusion of atomic hydrogen is the rate limiting step in the hydrogen permeation process.

The hydrogen permeability generally follows an Arrhenius law, therefore it is expressed as it follows:

$$\mu_{H2} = \mu^0_{H2} \cdot e^{-E_P/RT}$$

where μ^0_{H2} is the pre-exponential factor and E_P is an activation energy of permeation. An example of the trend of hydrogen permeation (volume of hydrogen that permeates the membrane per unit of membrane area and of time, cm^3/cm^{2}min) as a function of the hydrogen separation driving force is reported in Figure 1.9.

To increase the separation driving force, usually the retentate is kept at higher pressure than the permeate. In common applications, permeate pressure is atmospheric and retentate pressure is in the range 10-15 atm (compatibly with mechanical constraints).

A possible way to further increase the separation driving force is to reduce hydrogen partial pressure in the permeate ($P_{H2,P}$) by diluting the permeate stream with sweep gas (usually superheated steam).

Sievert's law shows that an increase of the hydrogen flux is achieved with reducing membrane thickness. Palladium membranes should not be far thinner than 80-100 μm due to mechanical stability of the layer and to the presence of defects and pinholes that reduce hydrogen selectivity. To overcome this problem, current technologies foresee a thin layer (20-50 μm) of Pd deposited on a porous ceramic or metal substrate [52,53].

Another important issue of Pd membranes (pure or supported) is thermal resistance. Temperature should not be less than 200 °C, to prevent hydrogen embrittlement and not higher than 600 °C ca. to prevent material damage.

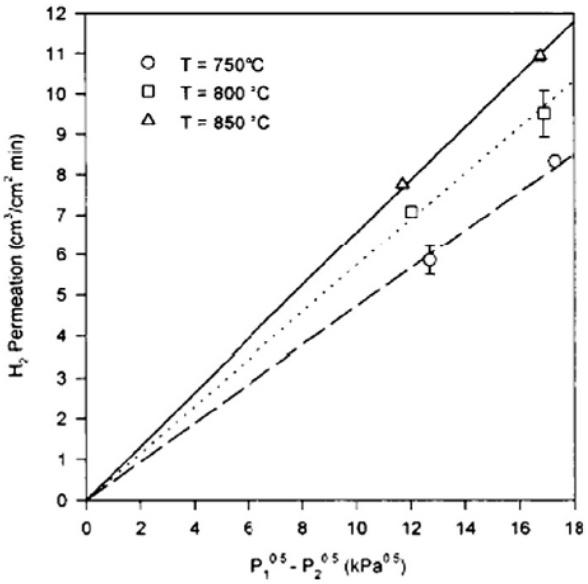

Figure 1.9 Hydrogen permeation as a function of the difference between the square roots of the hydrogen partial pressures on the retentate and permeate sides of the membrane [53]

Innovative fuel processors can be realized by combining the membrane either with the reforming unit, generating the fuel processor reported in Figure 1.10a (FP.1), or with a water gas shift unit, generating the fuel processor reported in Figure 1.10b (FP.2).

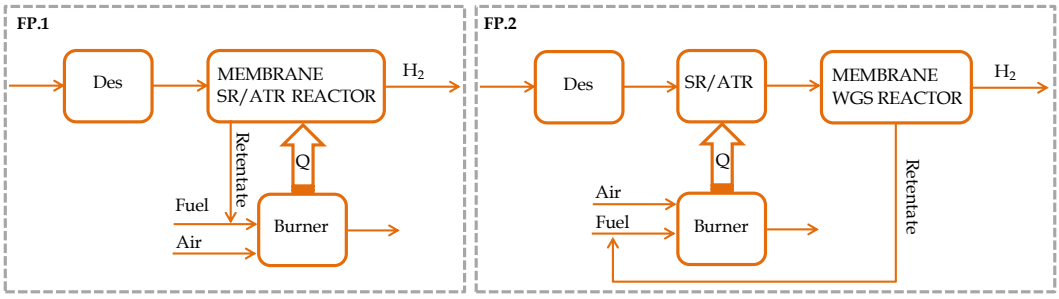

Figure 1.10 Innovative Fuel Processors

FP.1 consists of a desulfurization unit followed by a membrane reforming reactor, with a burner. This solution guarantees the highest compactness in terms of number of units, since it allows to totally suppress the CO clean-up section; indeed, when the membrane is integrated in the reforming reactor, the permeate stream is pure hydrogen, that can be directly fed to a PEMFC.
However, this solution limits the choice of the operating temperature of the process that must be compatible with the constraints imposed by the presence of a membrane.
FP.2 consists of a desulfurization unit followed by a reforming reactor and a membrane water gas shift reactor. In this case, the membrane is placed in the low temperature zone of the fuel processor, operating at thermal levels compatible with its stability. This solution, although less compact than the previous one, allows to operate the syngas production section at higher temperature.

Hydrogen separation membranes

Dense phase metallic and metallic alloy membranes have attracted a great deal of attention largely because they are commercially available. These membranes exist in a variety of compositions and can be made into large-scale continuous films for membrane module assemblies. For hydrogen, so far there has been some limited number of metallic membranes available that are effective. These are primarily palladium (Pd) based alloys exhibiting unique permselectivity to hydrogen and generally good mechanical stability [54-49]. Originally used in the form of relatively thick dense metal membranes, the self-supporting thick membranes (50–100μm) have been found unattractive because of the high costs, low permeance and low chemical stability. Instead, current Pd-based membranes consist of a thin layer (<20μm) palladium or palladium alloy deposited onto a porous ceramic or metal substrate [52, 60-62]. The alloying elements are believed to improve the membrane's resistance to hydrogen embrittlement [63-64] and increase hydrogen permeance [65]. For example, in Pd-Ag membranes, hydrogen permeability increased with silver content to reach a maximum at around 23 wt% Ag. Alloying Pd with Ag decreases the diffusivity but this is compensated by an increase in hydrogen solubility. Such alloyed membranes have good stability and

lower material costs, offering higher hydrogen fluxes and better mechanical properties than thicker metal membranes.

In general, dense phase metallic or alloy membranes (with Pd being the best precious metal for high permeability), offer very high selectivity for hydrogen. The permeance of hydrogen with thick self-supporting Pd membranes tends to be higher than supported thin film membranes, primarily because the very large grain size in these films. However, Pd membranes can undergo phase transformation which lead to cracks in the metal film due to expansion of the metal lattice. These phase changes are very pressure and temperature dependent. In the 1960s commercially manufactured Pd diffusers were used to extract H_2 from waste process gas streams, but within one year of their operation, pinholes and cracks developed and thus the operation was terminated [66]. In order to minimize operational problems, the current research effort focuses on deposition of Pd alloys to mesoporous supports. Relatively thicker films are required to minimize defects, so flux is limited. Other means to tackle the Pd embrittlement issue includes use of low cost amorphous alloys such as Zr, Ni, Cu and Al, but being a more recent technology is still in need of development toward practical operation [67]. It has also been reported that Pd-based membranes are prone to be poisoned by impurity gases such as H_2S, CO and deposition of carbonaceous species during the application [68-69].

Another problem associated with the metal membranes is the deposition of carbonaceous impurities when an initially defect free palladium composite membrane is used in high temperature catalytic applications. The further diffusion of these deposited carbonaceous impurities into the bulk phase of the membrane can lead to defects in the membrane [70].

1.5 Modeling of Fuel Processor - PEMFC systems

Optimization of energy efficiency and of system compactness of a fuel processor PEMFC system is a central issue in actual research studies. Since the efficiency of the PEMFC can be assumed as a constant equal to 60%, the efficiency of the entire system depends on fuel processor efficiency and on the integration between the fuel processor and the PEMFC. The same considerations can be done on

compactness: one of the main advantages of PEM fuel cells is their high power to weight ratio and their compactness, therefore this characteristic must be imposed to the development of the fuel processors.

The literature analysis on fuel processors – PEM fuel cell systems is rich of elements, from experimental works [71-75] to theoretical ones. As regards theoretical works, many works are available for conventional fuel processors, both on their optimization and on the modelling of the reactor. For the innovative fuel processor, moreover, there are many works on the detailed model of the membrane reactor, both in the case of syngas production reactor and of Water Gas Shift reactor.

The optimization of conventional hydrocarbon-based fuel processors has been tackled by several authors who have identified the most favourable operating conditions to maximize the reforming efficiency [9, 76-77].

As a general outcome, SR-based fuel processors provide the highest hydrogen concentration in the product stream, whereas the highest reforming efficiency is reached with ATR-based fuel processors, due to the lower energy loss represented by the latent heat of vaporization of the water that escapes with the combustion products [77].

In particular, data reported from Ahmed [77] in Table 1.2 for steam reforming and autothermal reforming of methane show that hydrogen percentage in SR reformer products is 80%, whereas it is 53.9% in the ATR case.

The reforming efficiency, defined as the ratio between the lower heating value of the hydrogen produced and the lower heating value of fuel employed, is higher in the ATR than in the SR case, taking also into account the fuel sent to the burner in the SR case.

However, as the system grows in complexity, due to the presence of the fuel cell, optimization of the global energy efficiency must also take into account the recovery of the energy contained in the spent gas released at the cell anode (anode off-gas).

Ersoz et al. [78] performed an analysis of global energy efficiency on a fuel processor – PEMFC system, considering two different fuels (natural gas and

diesel) as the fuel and steam reforming, partial oxidation and autothermal reforming as alternative processes to produce hydrogen.

	Steam Reforming	**Autothermal Reforming**
Fuel: Methane, n = 1, m = 4, p = 0		
LHV of fuel, cal/mol	191758	191758
Reformer feeds (mol)		
Methane, y	0.760	1.0
Oxygen		0.44
Nitrogen		1.66
Water	1.521	1.115
Reformer product, %		
Hydrogen	80	53.9
Carbon dioxide	20	17.3
Nitrogen	0.0	28.8
Total	100	100
Heat required for reforming (cal)	45974	
Fuel (methane) combusted, 1-y (mol)	0.2397	
Oxygen to burner (mol)	0.4795	
Combustion products (mol)		
Steam	0.4795	
Carbon dioxide	0.2937	
Hydrogen produced (mol)	3.04	3.11
Fuel used (mol)	1.00	1.00
Oxygen/fuel molar ratio, x	0.479	0.443
LHV of hydrogen (cal)	175764	180031
LHV of fuel used (cal)	191758	191758
$H_2/C_nH_mO_p$ (mol/mol)	3.04	3.11
Reforming efficiency	91.7	93.9

Table 1.2 Comparison of hydrogen yields and reforming efficiencies for steam reforming and autothermal reforming from methane conversion [77]

The results of Ersoz on the comparison of different fuels (natural gas NG, gasoline/diesel) in the steam reforming (SREF), autothermal reforming (ATR) and partial oxidation (POX) case are reported in Table 1.3.

The results show that the steam reforming process is more efficient than the ATR one, both in terms of reforming efficiency (η_{FP}) and of net electrical efficiency of the fuel processor – PEM fuel cell system ($\eta_{net,el}$). Moreover, it is possible to observe a strong difference in the efficiencies value in the steam reforming case when heat integration is performed in the system. Hence, heat integration system studies are of utmost importance along with the development of novel reforming

catalysts, clean-up systems and PEMFC components if on-board hydrogen production is desired.

Fuel	Process	Efficiency (η)	With heat integration	Without heat integration
NG	SREF (S/C = 3.5)	η_{FP}	98	89
		$\eta_{net,el}$	48	39
Gasoline Diesel	SREF (S/C = 3.5)	η_{FP}	86	-
		$\eta_{net,el}$	42	-
	ATR (S/C = 2.5) (O/C = 0.5)	η_{FP}	86	-
		$\eta_{net,el}$	37	-
	POX	η_{FP}	74	-
		$\eta_{net,el}$	31	-

Table 1.3 Overall fuel processor and net electric efficiency [78]

Since the steam reforming process resulted to give high system efficiencies, a huge number of studies is reported in literature on fuel processor – PEM fuel cell systems based on the SR process.

In particular, Colella [79] analyzed the effect of the afterburner conditions for the heat recovery of the Anode Off-Gas, showing how the energy efficiency of the system depends both on the temperature at the outlet of the burner and on the hydrogen utilization factor. The control of the afterburner sub-system is crucial to the performance of the overall system. This sub-system (1) determines the extent of thermal energy recovered from the system, up to 55% of fuel energy input; (2) establishes the rate limiting step in the control of the overall system based on its response time; and (3) impacts upstream mass and energy flows strongly, such as the system's overall water balance.

Gigliucci et al [80] performed an analysis of a fuel processor – PEM fuel cell system, showing how the efficiency of the system depends on the system configuration (Figure 1.11). From the basic configuration investigated, the increased heat recovery from the exhaust gases (1st improvement) showed to

increase the efficiency of the system, as well as the increase of the hydrogen utilization factor up to 85% (2nd improvement).
The same results were found by Hubert et al [81], that analyzed the effect of the system design and of the operating parameters on system performance. The system efficiency showed an increase with increasing the hydrogen utilization factor up to 75%, and with increasing the heat recovery in the system.

As far as membrane-based fuel processor is concerned, only few contributions which address the behavior of the entire system are available, that include not only the membrane-based fuel processor, but also the fuel cell, the auxiliary power units and the heat exchangers [82-86]. Most of these studies refer to liquid fuels and only few contributions are available when methane is employed.

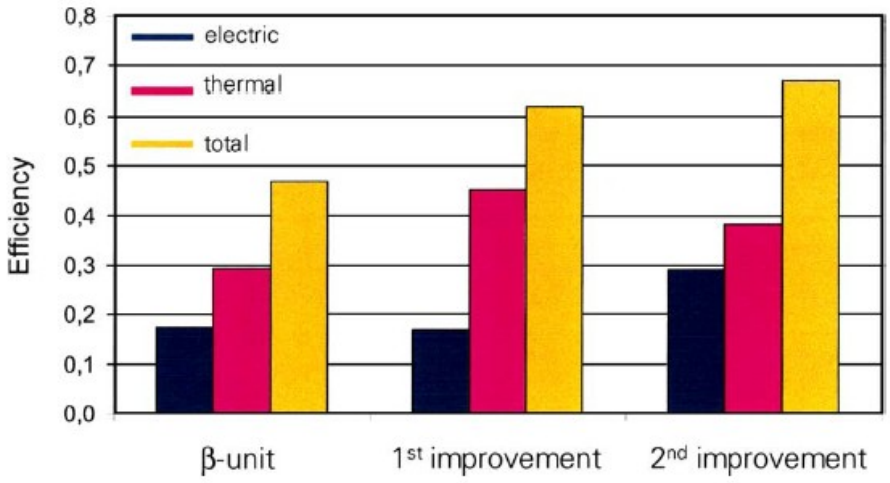

Figure 1.11 System global performances following to improvement actions [80]

In particular, Campanari et al. [85] analyzed an integrated membrane SR reactor coupled with a PEMFC, showing that a higher global energy efficiency can be achieved, with respect to conventional fuel processors, if a membrane reactor is employed (see data in Table 1.4).
The net electric efficiency for the SR solution is about 33%, while the ATR-based solution achieves a 0.3% higher net electric efficiency. The innovative membrane reformer solution yields a substantially better result, reaching an electric

efficiency of 43%, about 10 percentage points above the two conventional technologies.

	SR	ATR	MREF
Net electric efficiency, η_{el} (LHV) %	33.32	33.60	43.00
Thermal efficiency, η_{th} (LHV) %	68.28	67.31	57.60
Total, η_{tot} (LHV) %	101.60	100.91	100.60

Table 1.4 Efficiencies of three PEM fuel cell systems based on conventional SR and ATR and on a membrane SR [85]

The total efficiency for all the solutions is above 100%, higher for the SR and ATR fuel processors due to a lower exhaust flow rate and slightly lower mechanical and electrical losses. As a counterpart, due to the more complex cogeneration loop, the power consumed by the water pump in these two cases is twice than in the MREF case. Such high values of the total efficiency are reached thanks to the low stack temperatures (30 °C) allowed by low temperatures of heat recovery loops that make possible to recover a large fraction (about 85%) of latent heat in the exhaust gases.

Lyubovsky et al. [86] analyzed a methane ATR-based fuel processor – PEMFC system, with a membrane unit placed downstream the WGS unit and operating at high pressure, by means of the software AspenPlus. The flowsheet employed to perform the study is reported in Figure 1.12. The system foresees the feed of fuel, air and water required by the ATR reactor and takes into account the auxiliary units for compression of reactants, the ATR and WGS reactor, the separation unit that simulates the membrane, the burner for the retentate stream leaving the membrane and a turbine for recovering the enthalpy of the exhaust gases from the burner.

The analysis allows to conclude that a high global energy efficiency can be obtained if the power released by the turbine is introduced in the system to generate additional power from the expansion of the hot gases produced by the combustion of the membrane retentate stream. This solution, however, limits system compactness and is generally avoided in small-scale system. Therefore,

the interest in the research field is in the optimization of membrane based systems without the introduction of the turbine.

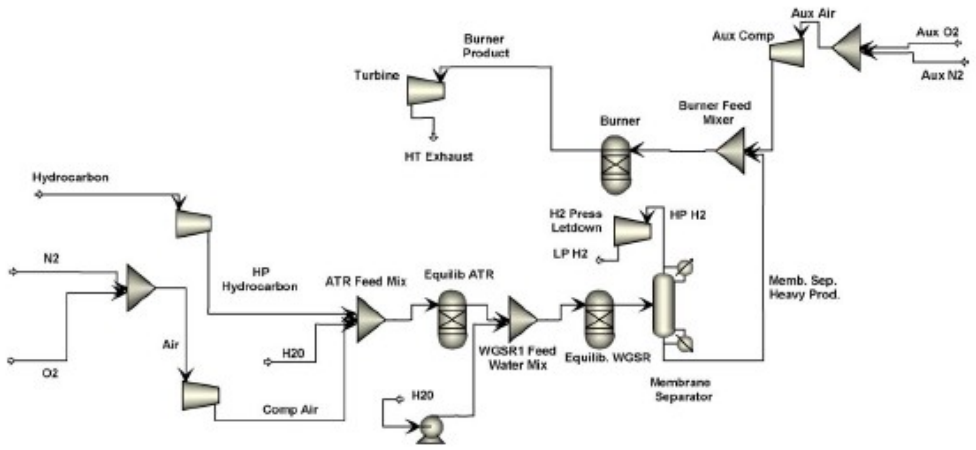

Figure 1.12 Flowsheet of the fuel processor – PEM fuel cell system [86]

Sjardin et al. [87] report an analysis of membrane reactor for hydrogen production for energy generation, considering also the CO_2 capture. The analysis of thermodynamic of the process shows the high performance of the reactor, whereas the economical analysis highlights the high costs still related to the employment of this kind of reactor; however, the scale of the process is 0.1 – 1.0 MW, higher than what generally studied for the residential energy system.

As regards the sizing of the reactors, in literature there are many reactor models and the fixed bed reactor models is well described in a huge number of works [88-91]. The membrane reactors model is also widely reported, in particular for Steam Reforming membrane reactors [85,82-99]. The works explore the operating variables, such as pressure and sweep gas, in order to increase hydrogen flux through the membrane and to increase fuel conversion.
Bottino et al. [98] analyzed the performance of a membrane reactor for methane Steam Reforming, simulating it as a series of reaction and separation stages. They showed the high performance of the reactor and also give some idea of the membrane area required to perform the operation.

The integration of the membrane in the reformer allows to increase the hydrogen flux and the methane conversion (Figure 1.13) with respect to the conventional case.

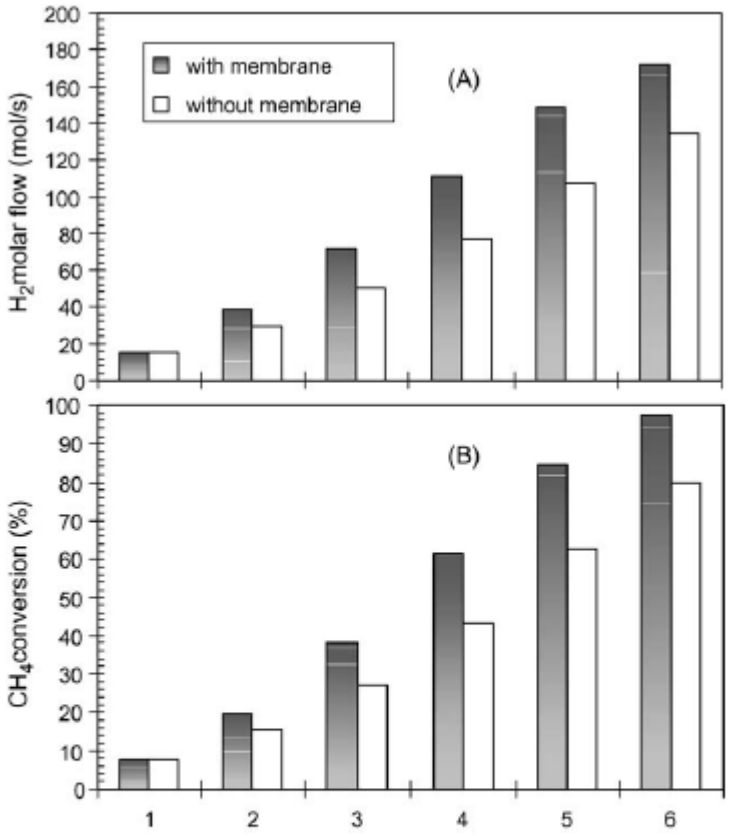

Figure 1.13 Comparison between equilibrium conventional methane steam reformer and membrane steam reformer. (A) Total H_2 produced in the single stages and (B) methane conversion [98]

The detailed model of the reactor with the effect of reactor size on performance was reported by Gallucci et al [99]. Simulation results show that different parameters affect methane conversion, such as the operating pressure, the temperature, and the membrane thickness, as well as the membrane reactor length. The effect of operating pressure seems to be not obvious, since it is combined with the effect of other parameters. In particular, in a traditional system an increase in the operating pressure always causes a decrease in methane conversion. Vice versa, for a membrane-aided reaction system an increase of the operating pressure corresponds either to an increase or to a decrease in methane

conversion, depending on the combination of pressure, temperature, membrane thickness, and reactor length (Figure 1.14).

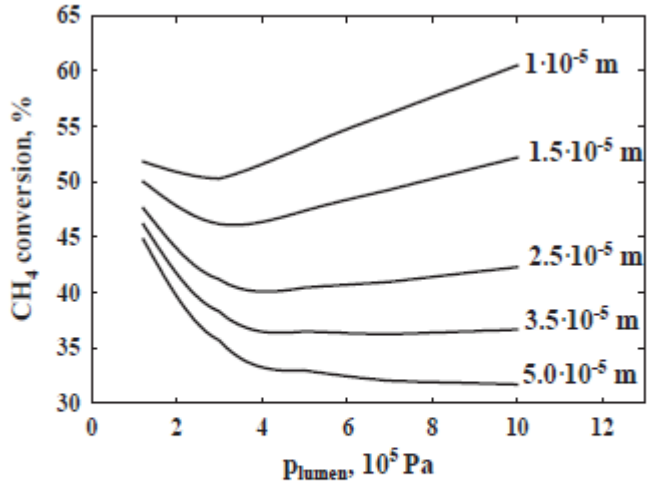

Figure 1.14 Methane conversion versus retentate side pressure for the membrane reactor at different membrane thickness [99]

The increase of reactor performance when the membrane is integrated in the reactor was also showed by Basile et al. [100] for the Catalytic Partial Oxidation Process. They demonstrated that the autothermal process reaches the methane conversion values of the conventional fixed bed reactor but at lower temperature (Figure 1.15), thanks to the shift in the equilibrium for the continuous hydrogen removal along reactor axis.

The importance of the operating parameters, such as membrane thickness, sweep gas flow rate, retentate pressure, was reported by other authors [95, 101-103] for the SR membrane reactor.

Since the high selective hydrogen membranes present some limitations related to the operating temperature, there is an interest also in the study of membrane Water Gas Shift reactors, that operates in a temperature range more compatible with membrane thermal stability.

The traditional Water Gas Shift reactor models for the size of the reactor are widely discussed in literature.

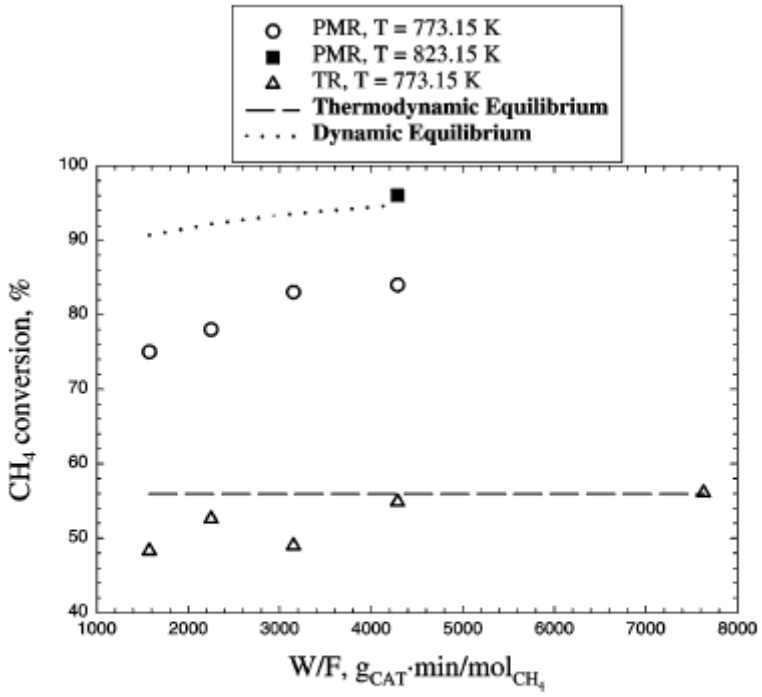

Figure 1.15 Methane conversion as a function of time factor for traditional (TR) and membrane reactor (PMR) [100]

Choi et al [104] performed a study of reaction kinetic of WGS, showing how the Langmuir – Hinshelwood model fits well the experimental data (Figure 1.16).

The effect of the main parameters, such as reaction temperature and gas hourly space velocity, GHSV, was investigated, showing how the increase of GHSV (that is, a reduction of the residence time) leads to a decrease of the CO conversion, as well as an increase of reaction temperature.

A detailed two dimentional model of the WGS reactor was developed by Adams et al. [105] that performed an analysis not only of the reactor performance, but also of the response to load changes since the model was dynamic. They found that if start-up occurs from a warm, empty state, the peak catalyst core temperatures can reach as much as 100 K above the maximum expected steady-state value. This effect, which cannot be detected by looking at steady-state conditions alone, could potentially cause sintering or damage to the catalyst, severely reducing the activity and lifetime of the catalyst. Such factors must be considered in the design of a plant. A sensitivity analysis showed that the parameters of the rate law equations used in the model have the biggest impact on

the overall results, and therefore, good experimental data is required to minimize the error in determining these parameters.

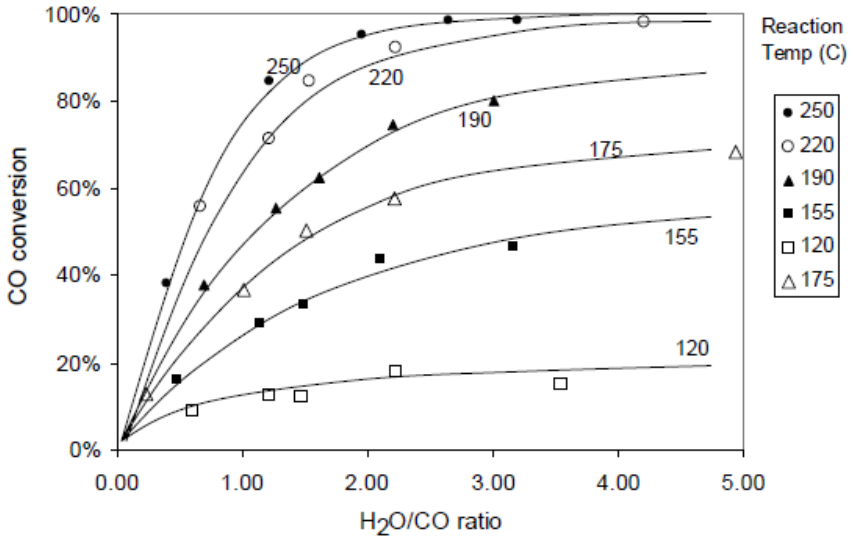

Figure 1.16 CO conversion as a function of the inlet H_2O/CO ratio parametric in reaction temperature. P = 1 atm, GHSV = 6100 hr^{-1} [104]

The works on mathematical models of membrane Water Gas Shift reactors, instead, are in a few number [64, 106-111], and most of them are isothermal. Moreover, the range of parameter investigated is in some cases limited and the results are often not reported in terms of hydrogen recovery [64,106].

Basile et al [64] developed an isothermal mathematical model of a membrane WGS reactor and analyzed the effect of the main operating parameters on reactor performance; they showed the resistance to hydrogen permeation is represented not only by the presence of the membrane, but also by the gaseous film at the interface with the membrane, that sees a drop of hydrogen partial pressure. The kinetic model employed in the work was the Temkin model, that was found to better fit the shift of the equilibrium due to hydrogen removal. Indeed the Langmuir-Hinshelwood mechanism (H-L model) was found to underestimate the CO conversion with respect to the experimental value (Figure 1.17).

The data shows that the membrane reactor gives better performance than the conventional reactor. The results are presented in terms of CO conversion and no

information are given on the hydrogen recovery or on the quality of the produced streams.

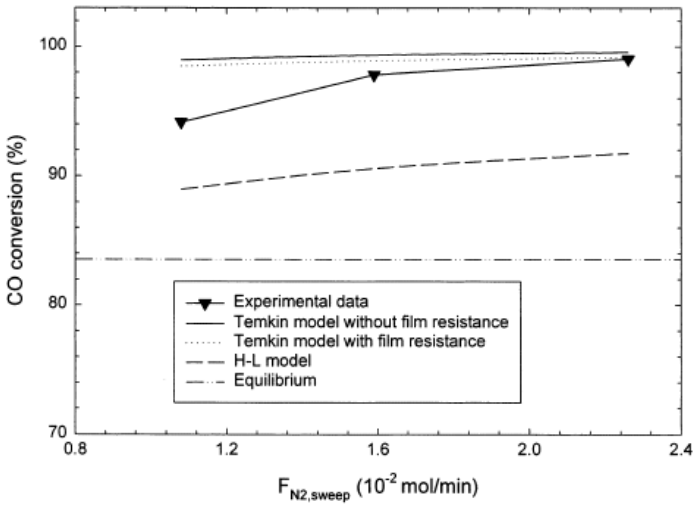

Figure 1.17 Effect of sweep gas flow rate on CO conversion for a Pd-based membrane [64]

Basile et al [108] performed a model analysis on the sweep gas configuration in the membrane WGS reactor. They found that the counter-current flow mode allows to obtain a better distribution of the hydrogen separation driving force than the co-current one, but no big differences are showed by reactor performance when the hydrogen permeance is high. Moreover, the counter-current mode allows to increase the hydrogen recovery at reactor outlet.

Brunetti et at [109] also performed an analysis of a membrane WGS reactor, in particular studying the variation of the inlet flow rate and pressure, showing how the pressure increase would allow to reduce the reactor volumes (Figure 1.18).

1.6 Aim of the work

From literature analysis, it appears evident that the PEM fuel cell energy systems are really promising and that a good design of the integrated fuel processor – PEM fuel cell system would allow to reach high efficiency levels. The introduction of

the membrane in the fuel processor should increase the reactors performance, but the effect on the overall efficiency of the system is not easily predictable.

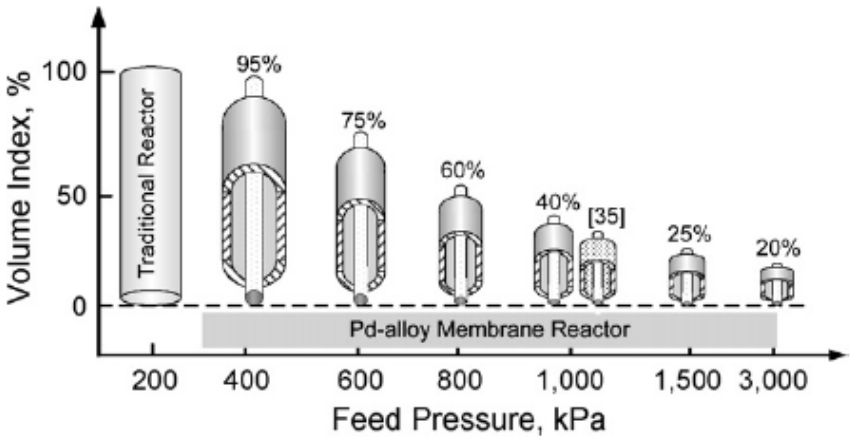

Figure 1.18 Volume reduction as a function of feed pressure [109]

Moreover, a huge number of study is present on conventional fuel processors, based on SR and on ATR, but the analysis of membrane-based fuel processor – PEM fuel cell system is more limited.

The literature analysis also showed the importance on reactor size, since the application of the system on small scale requires to satisfy the characteristics of compactness; the size of reactors is generally performed by means of mathematical models, that allow to investigate the effect of parameters on reactor performance.

The aim of this work is the optimization of fuel processor – PEM fuel cell systems in terms of efficiency and size.

In order to have a complete vision of the effect of system configuration and of operating parameters on fuel processor – PEMFC systems efficiency, a comprehensive analysis of different configurations will be presented; in particular, methane will be considered as fuel and SR and ATR as reforming processes; the focus of the discussion will be about the following fuel processor (FP) configurations, each coupled with a PEMFC:

FP.A) SR reactor, followed by two WGS reactors and a PROX reactor.

FP.B) ATR reactor, followed by two WGS reactors and a PROX reactor.

FP.C) Integrated membrane-SR reactor.

FP.D) Integrated membrane-ATR reactor.

FP.E) SR reactor followed by a membrane WGS reactor

FP.F) ATR reactor followed by a membrane WGS reactor

Each system configuration is investigated by varying operating parameters, such as steam to methane and oxygen to methane inlet ratios, reforming temperature, as well as pressure; the effect of the addition of steam as sweep gas on the permeate side of the membrane reactors will be also presented and discussed.

Since there is a huge number of units and of operating parameter, a first analysis was performed with AspenPlus, that allowed to determine the most promising configuration in terms of energy efficiency; later, a more detailed analysis for the sizing of the system was performed by developing a mathematical model in Mathematica in order to study the effects of parameters on system dimension. Therefore, the determination of the optimal configuration was made on the basis of both efficiency and compactness factor.

Moreover, since the interest in this system is dictated not only by the possibility of increasing energy generation efficiency, but also by the employment of new energy sources, a comparison with the efficiency obtained employing ethanol as fuel is also reported.

System analysis: Methods

This chapter reports the detail on the simulation performed with the commercial software AspenPlus® [112] on fuel processor – PEM fuel cell systems.
The simulations were performed in stationary conditions and the property method was Peng-Robinson; the component list was restricted to CH_4, O_2, N_2, H_2O, CO, H_2 and CO_2.
Methane (CH4) was considered as fuel, fed at 25 °C and 1 atm, with a constant flow rate of 1 kmol/h. Feed to the system was completed with a liquid water stream (H2O, 25 °C and 1 atm) both in SR and ATR-based FPs; an air stream (AIR, 25 °C and 1 atm) is also present in the ATR-based FPs.
AspenPlus® was used to calculate product composition throughout the plant as well as energy requirements of each unit.
The configurations simulated (flowsheets) are presented in the following sections, where the assumptions and the model libraries used to simulate the process are presented. Section 2.1 is dedicated to conventional fuel processors, whereas membrane-based fuel processors are described in section 2.2.
The quantities employed to calculate energy efficiency are defined in section 2.4.

2.1 Conventional fuel processor –fuel cell systems

Figure 2.1 reports the flowsheet of a conventional SR-based fuel processor coupled with a PEM fuel cell (FP.A). The fuel processor consists of a reforming and a CO clean-up section.
The reforming section is an isothermal reactor (SR), modelled by using the model library ***RGIBBS*** (Figure 2.2). This kind of reactor is an equilibrium reactor, that performs chemical and phase equilibrium by Gibbs energy minimization. The

input data required by this reactor are pressure and temperature or heat duty. In the case of SR reactor, the temperature is assigned.

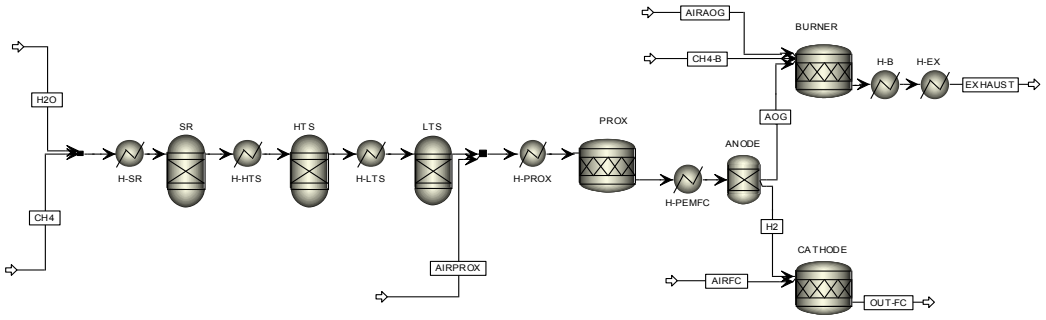

Figure 2.1 Flowsheet of fuel processor FP.A coupled with a PEM fuel cell

The CO clean-up section consists of a high (HTS) and low (LTS) temperature water gas shift reactor followed by a PROX reactor. HTS and LTS were modeled by using model library ***RGIBBS***; the reactors were considered as adiabatic and methane was considered as an inert in order to eliminate the undesired methanation reaction, kinetically suppressed on a real catalytic system.

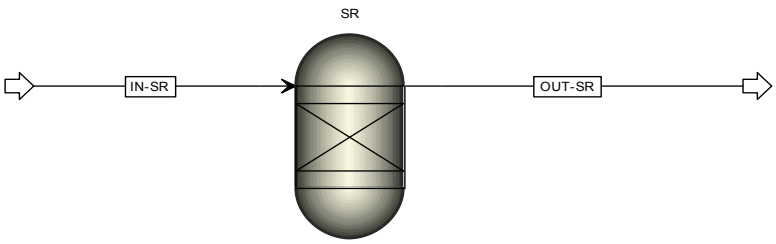

Figure 2.2 RGIBBS reactor

The inlet temperature to the HTS reactor was fixed at 350 °C, while the inlet temperature to the LTS one was of 200 °C. The PROX reactor was modeled as an adiabatic stoichiometric reactor, ***RSTOIC*** (Figure 2.3); this kind of reactor models a stoichiometric reactor with specified reaction extent or conversion; in the case of PROX, two reactions were considered: oxidation of CO to CO_2 with complete

conversion of CO and oxidation of H_2 to H_2O; the air fed to the PROX reactor (AIR-PROX) was calculated in order to achieve a 50% oxygen excess with respect to the stoichiometric amount required to convert all the CO to CO_2. The ***RSTOIC*** specifics were completed with the assignment of total conversion of CO and O_2. The inlet temperature to the PROX reactor was fixed at 90°C.

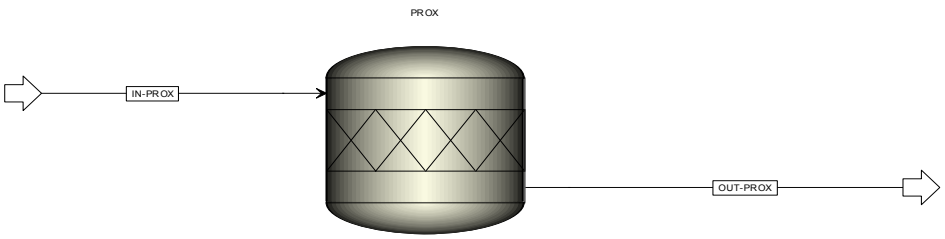

Figure 2.3 RSTOIC reactor

The PEM fuel cell section is reported in Figure 2.4; it is simulated as the sequence of the anode, modeled as an ideal separator, ***SEP***, and the cathode, modeled as an isothermal stoichiometric reactor, ***RSTOIC.*** The presence of the ***SEP*** unit allows to model a purge gas (anode off-gas, AOG) required for mass balance reasons, whenever the hydrogen stream sent to the PEM fuel cell is not 100% pure.

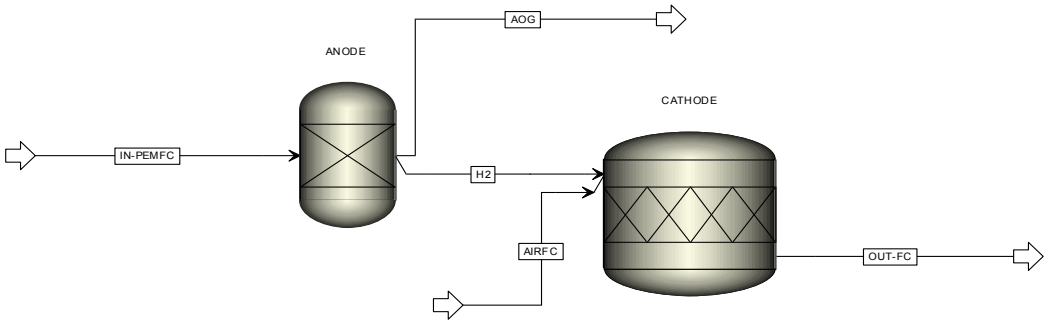

Figure 2.4 PEM fuel cell section

In agreement with the literature, the hydrogen split fraction in the stream H_2 at the outlet of the ***SEP*** is fixed at 0.75 [113-114], whereas the split fractions of all the other components is equal to 0.

The ***RSTOIC*** unit models the hydrogen oxidation reaction occurring in the fuel cell. The reactor specifics were completed by considering an operating temperature of 80 °C and pressure of 1 atm; the inlet air at the cathode (AIR-FC) was fed at 25 °C and 1 atm and its flow rate guarantees a 50% excess of oxygen. In agreement with the literature [115], these conditions were considered as sufficient to assign total hydrogen conversion in the reactor. The anode off-gas is sent to a burner, modeled as an adiabatic ***RSTOIC***, working at atmospheric pressure with 50% excess air (AIR-B).

The temperatures throughout the plant were regulated by means of heat exchangers (H), modeled by using model library ***HEATER***. In particular, the heat required by the SR reactor working at temperature T_{SR} is supplied by the heat released by the outlet gases from the burner (OUT-B) in the heat exchanger H-B, modeled as a ***HEATER***, where they are cooled until $T > T_{SR}$. An additional methane stream (CH4-B) is sent to the burner to eventually supply the heat demand of the SR reactor.

The heat available in the other heat exchangers, that is H-HTS, H-LTS, H-PROX, H-PEMFC and H-EX, is employed to pre-heat the reactants in H-SR, in order to reduce or to eliminate the flow of methane to the burner. As far as H-EX is concerned, 100 °C was chosen as the minimum exhaust gas temperature, when compatible with the constraint of a positive driving force in all the heat exchangers present in the plant.

All the reactors were considered as operating at constant pressure, therefore zero pressure drop was always assigned.

Figure 2.5 reports the flowsheet of a conventional ATR-based fuel processor (FP-B) coupled with a PEM fuel cell.

For the sake of simplicity, the description of the flowsheets will be carried out by indicating the differences with respect to the flowsheet of Figure 2.1. The differences between the two fuel processors are concentrated only in the reforming section; in this case, the reforming section is constituted by an adiabatic reactor (ATR), modeled by using the model library ***RGIBBS***. Being the reactor adiabatic, the hot gases from the burner are employed only for feed pre-heating.

The inlet temperature to the ATR reactor is fixed at 350 °C, and is regulated by means of the heat exchanger H-ATR.

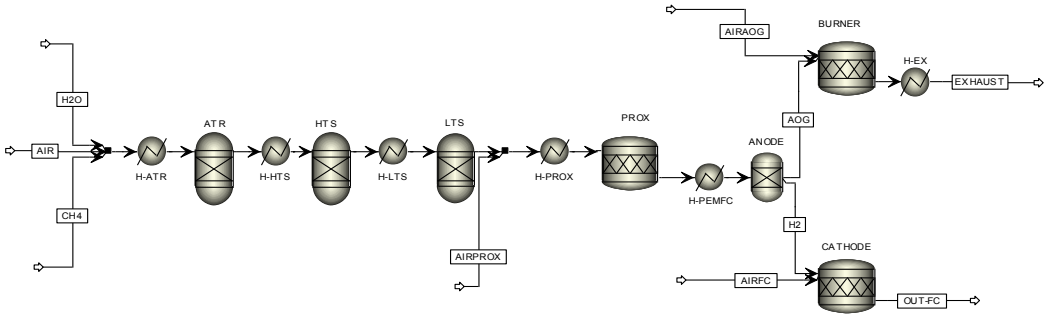

Figure 2.5 Flowsheet of fuel processor FP.B coupled with a PEM fuel cell

2.2 Membrane-based fuel processor – fuel cell systems

In this section the fuel processor – fuel cell systems based on membrane technology for hydrogen separation are described; the membrane-base fuel processors investigated are the following:

FP.C) Membrane SR reactor
FP.D) Membrane ATR reactor
FP.E) SR reactor followed by a membrane WGS reactor
FP.F) ATR reactor followed by a membrane WGS reactor

Figure 2.6 and Figure 2.7 report the flowsheet of FP.C and FP.D coupled with a PEM fuel cell, respectively.
The system with FP.D has got the same flowsheet of the one with FP.C, unless the absence of air in the feed and the presence of the heat-exchanger H-B downstream the burner, for sustaining the SR reactor, as described for FP.A.

The integrated membrane reactor couples the reaction with the separation in the same unit and is simulated by discretizing the membrane reactor into N reactor-separator units. In the discrete approximation, reactors are assumed to reach equilibrium, therefore they are simulated as ***RGIBBS***. The separator units are

simulated as described later on in the paragraph, where the equations are specified for each separation stage.

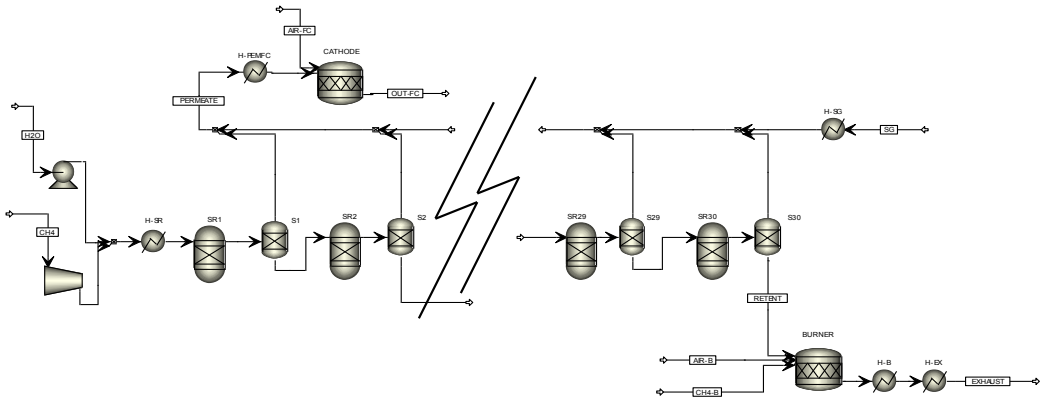

Figure 2.6 Flowsheet of fuel processor FP.C coupled with a PEM fuel cell

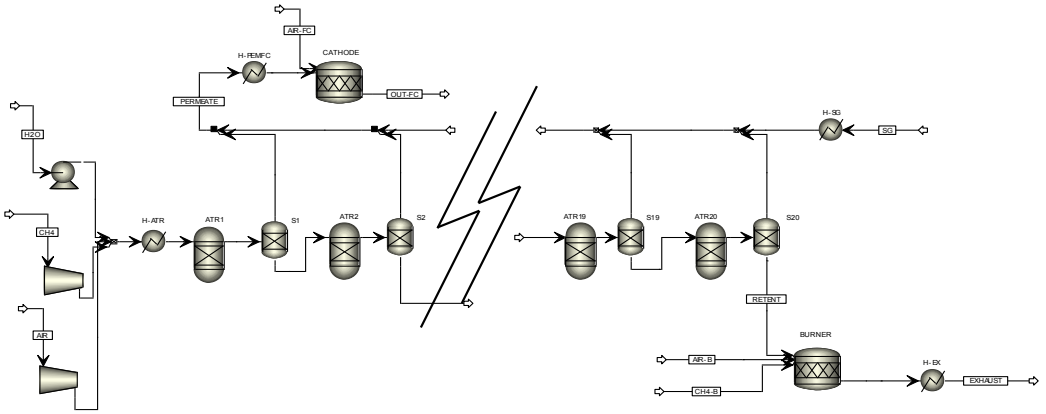

Figure 2.7 Flowsheet of fuel processor FP.G coupled with a PEM fuel cell

The membrane reactor was discretized into 30 units for FP.C and into 20 units for FP.D;

The number of units required for modelling the integrated membrane reactor was assessed by repeating the simulations with an increasing number of reactor-separator units and was chosen as the minimum value above which global efficiency remains constant within ± 1%.

The membrane is simulated as an ideal separator, ***SEP*** (Figure 2.8), whose output is given by a stream of pure hydrogen (permeate stream, PERMEATE) and a stream containing all the balance (retentate stream, RETENT).

The amount of hydrogen separated from the reformate ($n_{H2,P}$) is calculated assuming equilibrium between the partial pressure in the retentate and permeate side:

$$P_R \cdot \left(\frac{n_{H2,R} - n_{H2,P}}{n_R - n_{H2,P}} \right) = P_{H2,P}$$

where P_R is the pressure in the retentate side of the membrane, equals to the reformate pressure; $n_{H2,R}$ is the mole flow of hydrogen in the retentate stream; n_R is the total mole flow of the retentate stream; $P_{H2,P}$ is hydrogen partial pressure in the permeate side of the membrane, calculated as:

$$P_{H2,P} = \frac{n_{H2,P}}{n_{H2,P} + n_{SG}} \cdot P_P$$

where P_P is the pressure in the permeate side of the membrane, taken as 1 atm in all the simulations, and n_{SG} represents the molar flow rate of steam sweep gas (SG), which is introduced to increase the separation driving force in the membrane.

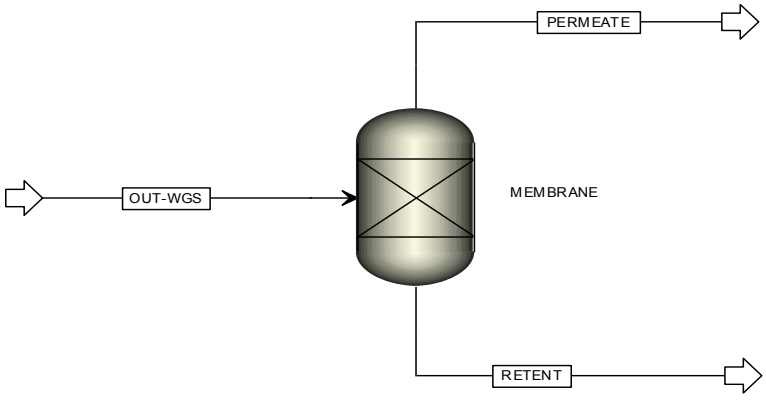

Figure 2.8 Hydrogen separation membrane, modelled as a SEP

The liquid water used to produce the sweep gas is fed at 25 °C and 1 atm to the heat exchanger H-SG, where it is vaporized and superheated, then the sweep gas is sent to the membrane. The sweep gas temperature at the outlet of H-SG was fixed at 600 °C both in the SR and in the ATR case.

The permeate stream is cooled in a heat exchanger until 80 °C and then sent to the PEM fuel cell. The high hydrogen purity of the stream sent to the PEM fuel cell got in the membrane based fuel processor, allows to take as zero the anode off-gas, simplifying the model of the PEM fuel cell, reported in conventional fuel processor description, to the cathode side (***RSTOIC***) only.

The effect of sweep gas on the performance of a system with integrated membrane reactor was assessed by considering two sweep gas flow modes, as reported in Figure 2.9. The first sweep gas flow mode, illustrated in Figure 2.9a, simulates a membrane reactor in which the sweep gas and the reacting stream flow co-currently. The second flow mode (Figure 2.9b), corresponds to a membrane reactor in which the sweep gas and the reacting stream flow counter-currently.

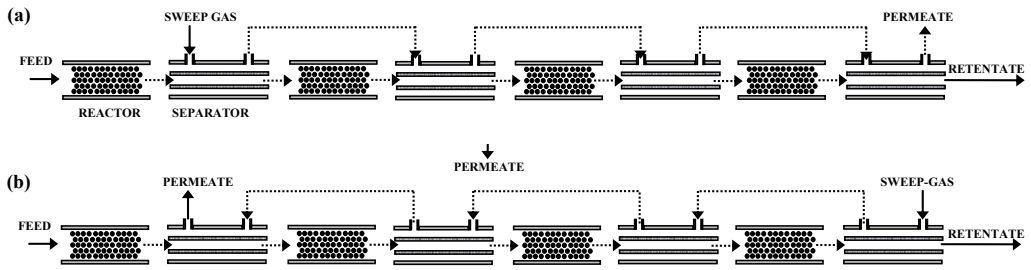

Figure 2.9 Schematic representation of the sweep gas flow modes investigated for FP.D: (a) co-current sweep mode; b) counter-current sweep mode mode.

Figure 2.10 and Figure 2.11 report the flowsheets used to simulate the fuel processors FP.E and FP.F coupled with a PEM fuel cell, respectively.

As for the membrane based systems described above, the two flowsheets are substantially the same, unless the absence of air in the feed and the presence of the heat-exchanger H-B downstream the burner, for sustaining the SR reactor, as described for FP.A.

The membrane WGS reactor was discretized into 10 units in both cases.

The inlet temperature to the membrane WGS reactor was fixed at 300 °C, as well as the sweep gas temperature at the outlet of H-SG.

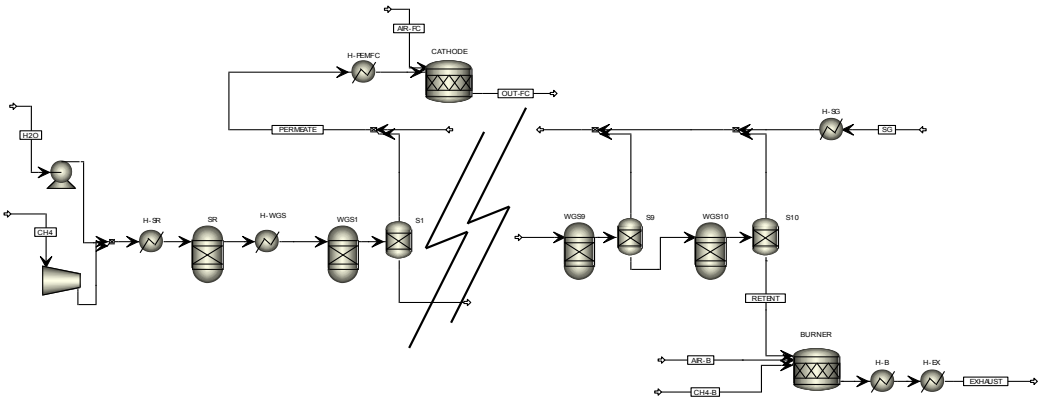

Figure 2.10 Flowsheet of fuel processor FP.E coupled with a PEM fuel cell

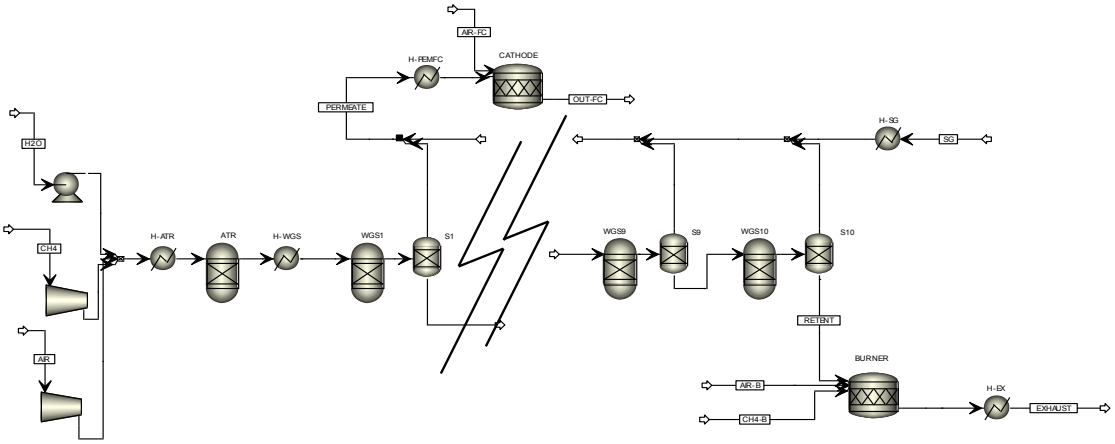

Figure 2.11 Flowsheet of fuel processor FP.F coupled with a PEM fuel cell

As for system with FP.A, the systems with FP.C and FP.E (SR based systems) foresee a heat exchanger H-B where the exhaust gases from the burner release their heat content for sustaining the endothermic SR reactions; the exhaust gases leave H-B at a temperature higher than T_{SR}, and further heat can be recovered in H-EX. The retentate stream (RETENT) from the last separation unit (S30 or S10) is sent to the burner where it can react with air (AIR-B); an additional methane stream to the burner (CH4-B) is considered if necessary.

In the systems with FP.D and FP.F (ATR based systems), the exhaust gases are sent directly to H-EX since the ATR reactor is adiabatic and autothermal for the presence of air in the feed; for the rest, the flowsheets are analogous to the one with FP.C and FP.E, respectively.

In the membrane based system, auxiliary power units for compression of the reactants fed to the reformer where considered, since pressure was explored as an operation variable. In particular, a pump is foreseen for water compression, with an efficiency of 0.95, and two compressor for methane and air are considered; a polytropic compression efficiency of 0.85 is imposed in Aspen, while the mechanical efficiency was taken as 1.

It is worth mentioning that the assumptions made to model the system are the same for all the configurations investigated and do not affect the conclusions drawn in this comparative analysis.

2.3 Heat exchanger network

In this study, for each fuel processor - fuel cell systems a suitable heat exchanger network was identified to maximize the use of heats available in the various sections of the system without temperature cross-over in the heat exchangers.
The model library ***HEATEX*** (Figure 2.12) is used to exchange heat between the cold reactants and the hot streams in various sections of the plant.

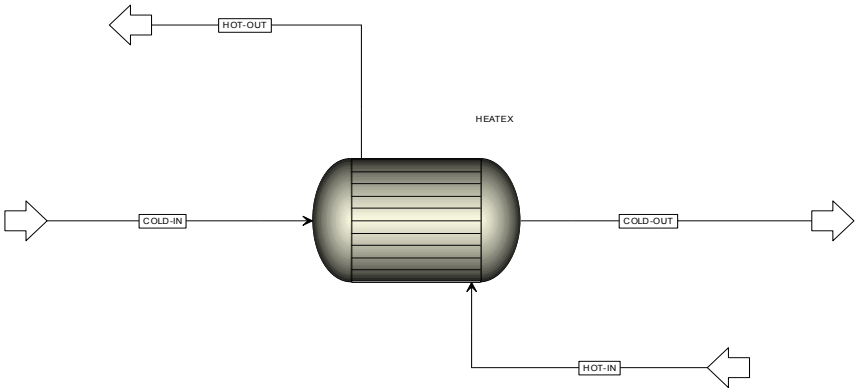

Figure 2.12 HEATEX

The heat exchanger network for each system was determined by fixing the temperature of the outlet stream from the fuel cell at 80 °C, while the temperature of the exhaust gas stream (EXHAUST) was allowed to vary, depending on the optimization of the use of the heats.

2.4 System efficiencies

Energy efficiency, η, was defined according to:

$$\eta = \frac{P_e - P_a}{(n_{CH4,F} + n_{CH4,B}) \cdot LHV_{CH4}}$$

where P_a is the electric power required by the auxiliary units for compression of methane, air and water, $n_{CH4,F}$ is the inlet molar flow rate of methane to the reactor, $n_{CH4,B}$ is the molar flow rate of methane fed to the burner, LHV_{CH4} is the lower heating value of methane and P_e is the electric power generated by the fuel cell, calculated as:

$$P_e = n_{H2} \cdot LHV_{H2} \cdot \eta_{FC}$$

where n_{H2} is the molar flow rate of hydrogen that reacts in the fuel cell, LHV_{H2} is the lower heating value of hydrogen, η_{FC} is the electrochemical efficiency of the cell, taken as 0.6 [116].

In the membrane-based fuel cell systems, an important parameter is the global hydrogen recovery (HR), defined as:

$$HR = \frac{\sum_{i=1}^{N} n^i_{H2,P}}{n_{H2,R} + \sum_{i=1}^{N} n^i_{H2,P}}$$

where $n^i_{H2,P}$ is the molar flow rate of hydrogen separated by the i-th membrane unit, $n_{H2,R}$ is the molar flow rate of hydrogen in the RETENT stream at the exit of the last separator and N is the number of separators.

According to the definitions given above, η can be expressed as it follows:

$$\eta = \text{HR} \cdot \eta_R \cdot \eta_{FC} - \text{a}$$

where f_a is the fraction of inlet methane required to run the auxiliary units, defined as:

$$f_a = \frac{P_a}{n_{CH4,F} \cdot LHV_{CH4}} \cdot (1 - \text{e}$$

where α is the ratio between methane flow rate fed to the burner and total methane flow rate fed to the system, defined as:

$$\alpha = \frac{n_{CH4,B}}{n_{CH4,F} + \text{CH4,B}}$$

η_R is the hydrogen production energy efficiency, defined as:

$$\eta_R = \frac{\left(\text{H2,R} + \sum_{i=} \text{I2,P} \right) LHV_{H2}}{n_{CH4,F} \cdot LHV_{CH4}} \cdot (1 - \text{e}$$

2.5 Model Analysis Tools

The Calculator Tool was used to calculate the amount of hydrogen separated by the membrane unit, by introducing the relation defined for hydrogen separation for each separation stage; it was also used to calculate the air flows required by the PROX reactor, by the PEM fuel cell and by the burner, respecting the 50% oxygen excess specific.

The Sensitivity Tool was used to evaluate energy efficiency, with varying the operating parameters.

The Design Specification Tool was used to determine the amount of methane fed to the burner. For SR-based fuel processors, the mole flow of methane fed to the

burner is evaluated imposing that the heat duty of the heat exchanger H-B is equal to sum of the heat duties of the SR reactors and eventually of the heat required for superheating of the sweep gas in H-SG.

For ATR-based fuel processors, the mole flow of methane fed to the burner, eventually required, is evaluated imposing that the inlet temperature to the ATR reactor is 350 °C.

System analysis: Results - Methane

In this chapter, the results of a simulative energy efficiency analysis performed on innovative fuel processor - PEM fuel cell systems is reported; hydrogen is produced via methane Reforming processes, in particular via Steam Reforming and via Autothermal Reforming; in the fuel processors investigated, hydrogen is purified either with conventional technique (with a series of Water Gas Shift and Preferential CO oxidation reactors) or with a membrane unit, coupled with a Water Gas Shift reactor or with the Reforming reactor; hydrogen is then converted into electric energy by means of a PEM fuel cell.
This report presents three basic fuel processor configurations, coupled with a PEM fuel cell:

i) Conventional fuel processor: Reforming reactor (SR or ATR), followed by two WGS reactors and a PROX reactor.
ii) Integrated membrane-reforming reactor (SR or ATR)
iii) Reforming reactor (SR or ATR), followed by a WGS reactor and a hydrogen separation membrane or by an integrated membrane-WGS reactor.

Simulation where performed by varying the main operating parameters for each system. The parameters investigated and the ranges explored are reported in Table 3.1. For conventional systems (FP.A and FP.B) pressure was fixed at 1 atm since reforming processes are inhibited by pressure increase, whereas the WGS and PROX processes are independent of pressure. The operating ranges of H_2O/CH_4 and T_{SR} for the system with membrane SR reactor (FP.C) are chosen in order to guarantee thermal stability of the membrane and to avoid coke formation. The pressure range investigated for the innovative systems was chosen in order to guarantee the mechanical resistance of the membrane. The operating ranges of

H_2O/CH_4 and of O_2/CH_4 for the ATR systems are chosen in order to avoid coke formation and to guarantee the autothermicity of the process [9].

	Case	H_2O/CH_4	O_2/CH_4	T_{SR} [°C]	SG/CH_4	P [atm]
SR	FP.A	2.0 – 6.0	-	600 - 800	-	1
	FP.C	2.5 – 6.0	-	500 - 600	0 – 3.0	3 – 15
	FP.E	2.0 – 6.0	-	600 - 800	0 – 3.0	3 – 15
ATR	FP.B	1.2 – 4.0	0.3 – 1.0	-	-	1
	FP.D	1.2 – 4.0	0.3 – 1.0	-	0 – 3.0	3 – 15
	FP.F	1.2 – 4.0	0.3 – 1.0	-	0 – 3.0	3 – 15

Table 3.1 Range of operating parameters investigated

Section 3.1 is dedicated to system analysis of conventional fuel processor – PEM fuel cell systems; the effect of membrane addition in the reforming reactor is reported in paragraph 3.2; section 3.3 describes the systems with the membrane WGS reactor placed downstream the reforming reactor.

3.1 Conventional Fuel Processors

Simulations on the conventional systems were performed at 1 atm. For the SR-based fuel processor (FP.A), the operative parameters explored were the molar ratio between water and methane at reactor inlet (H_2O/CH_4) and Steam Reforming reactor temperature (T_{SR}); for the ATR-based fuel processor (FP.B), water to methane (H_2O/CH_4) and oxygen to methane (O_2/CH_4) inlet ratios were considered as operating parameters.

Figure 3.1 reports the flowsheet of the system with FP.A that allows to obtain the highest efficiency; as mentioned in chapter 2, a careful research of the best configuration was conducted in order to identify the heat exchanger network that maximizes global efficiency.

Methane and air are mixed and preheated recovering the heat available at the outlet of the PROX, LTS, HTS and SR reactor, then they are sent to the SR reactor; the heat for sustaining the endothermicity of the SR reactions is supplied

by the gases that exit from the b urner; the heat available in this stream is also employed for preheating methane and air fed to the burner.

The flowsheet for the system with FP.B is reported in Figure 3.2 and the heat exchanger network is analogous to the one found for FP.A, under the heat exchanger for preheating the feed to the burner.

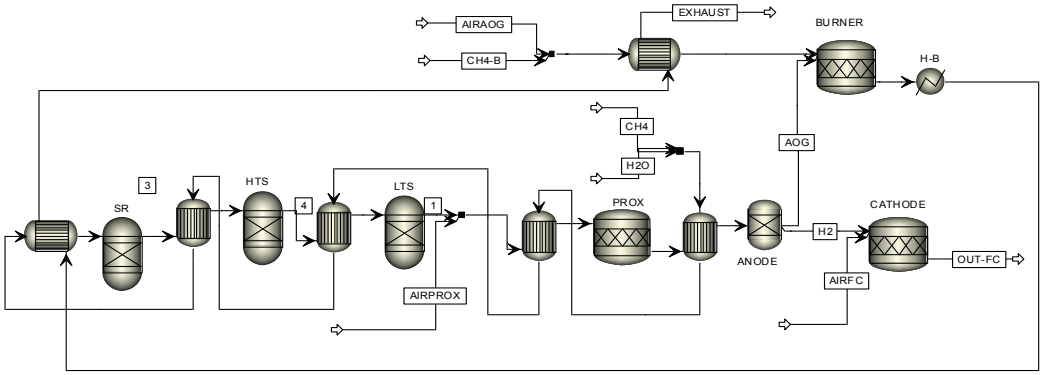

Figure 3.1 Flowsheet of fuel processor FP.A coupled with a PEM fuel cell

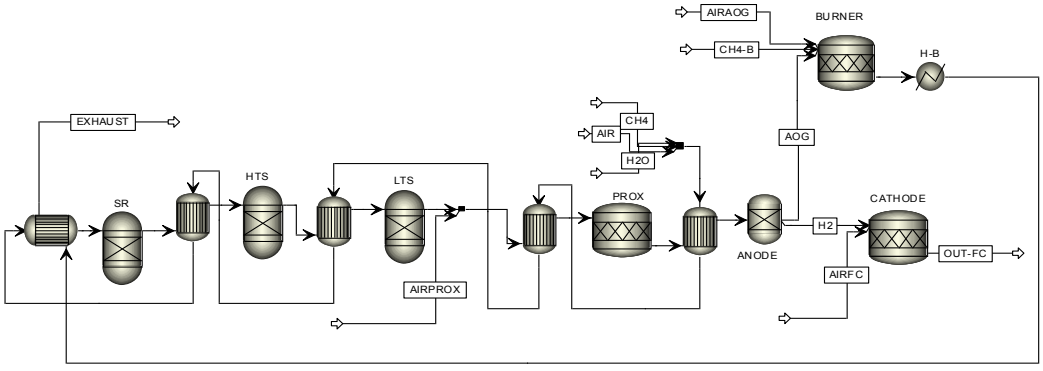

Figure 3.2 Flowsheet of fuel processor FP.B coupled with a PEM fuel cell

Figure 3.3 shows the trend of energy efficiency η, methane conversion x_{CH4}, reforming factor f_R and the fraction of total inlet methane that is sent to the burner α as a function of H_2O/CH_4, parametric in the steam reforming reactor temperature.

For all the temperatures investigated, an increase of water content in the feed has a positive effect on methane conversion x_{CH4} and on the reforming factor f_R. This well note trend is due to the fact that water is a reactant of reforming reactions.

For each temperature and until a certain value of H_2O/CH_4, the value of α is equal to zero. For higher H_2O/CH_4, the increase of this ratio leads to an increase of α; indeed, the increase of H_2O/CH_4 causes an increase of the heat required to sustain the reforming process, moreover the improvement of reforming reactor performance with H_2O/CH_4 causes a reduction of the heating value of the AOG stream, thus an increase of the quantity of methane that needs to be sent to the burner for sustaining the endothermicity of the process.

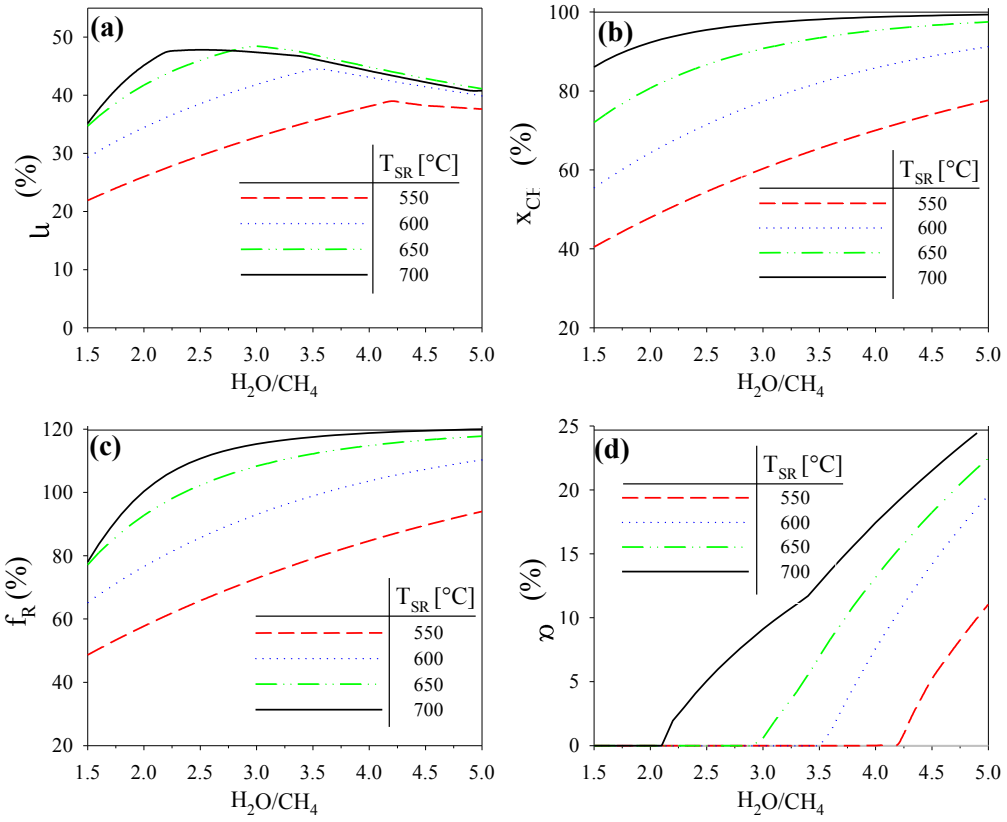

Figure 3.3 η (a), x_{CH4} (b), f_R (c), α (d) in function of H_2O/CH_4 parametric in T_{SR}

As described in the System efficiency Section, the energy efficiency is a combination of f_R and of α; indeed, η shows a non monotone trend as a function of H_2O/CH_4 because, although an increase of water content causes a continuous

increase of reforming reactor performance, the amount of methane sent to the burner also increases with H_2O/CH_4.

For all the H_2O/CH_4 investigated, the increase of reforming reactor temperature (T_{SR}) causes an increase of x_{CH4}, f_R and α. Energy efficiency η shows a different trend on the basis of the weight of these factors: for low H_2O/CH_4, η shows a continuous increase with T_{SR} in the range investigated, whereas, for high H_2O/CH_4, η shows a non monotone trend with T_{SR}.

Figure 3.4 shows the trend of energy efficiency η, methane conversion x_{CH4}, reforming factor f_R for conventional ATR-based fuel processor – PEMFC systems (systems with FP.B), as a function of O_2/CH_4 parametric in H_2O/CH_4.

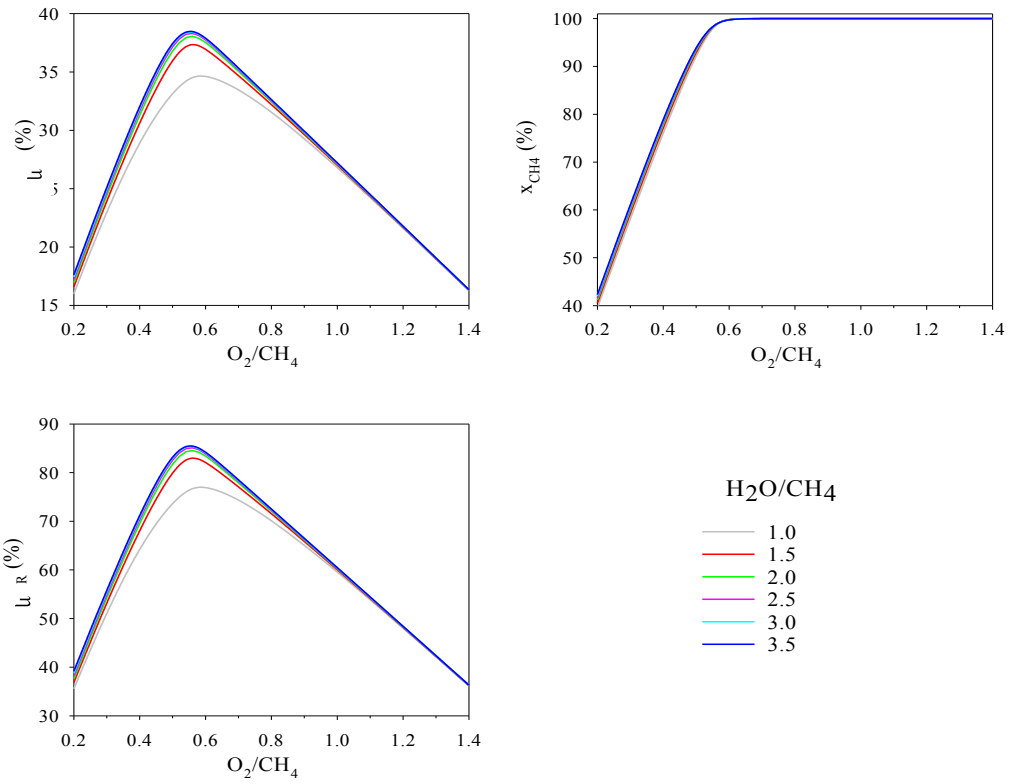

Figure 3.4 η (a), x_{CH4} (b), f_R (c) as a function of O_2/CH_4 parametric in H_2O/CH_4

Methane conversion shows a monotone increase as a function of O_2/CH_4. The effect of water addition on methane conversion is positive in case x_{CH4} is far lower

than unity, whereas this effect can be considered as negligible when the conversion approaches to unity.

Reforming factor shows a non monotone trend as a function of O_2/CH_4; indeed, for low O_2/CH_4 values the process cannot reach the temperature values that favour the reforming reactions, whereas for high O_2/CH_4 values, although the reforming temperature result to be strongly increased, the hydrogen and methane oxidation reactions are favourite, with subsequent reduction of the amount of hydrogen produced and, thus, of the f_R.

The addition of water leads to an increase of f_R, being water a reactant of the reforming reactions; this increase becomes negligible for H_2O/CH_4 values higher than 2.

For all the O_2/CH_4 and H_2O/CH_4 values investigated, α remains equal to zero, therefore, the trend of energy efficiency results to be the same of the reforming factor; moreover, there is a waste of heat from the system, related to the autothermic nature of the process, that hinders the possibility of recovering the energy content of the AOG.

Table 3.2 reports the simulation results and the value of the operative parameters given as simulation input that maximize the energy efficiency η, for FP.A and for FP.B, respectively.

Simulation results				
	x_{CH4}	**α**	**η**	**T_{EX} (°C)**
FP.A (SR)	91.0	0.0	48.0	226
FP.B (ATR)	98.8	0.0	38.5	444
Simulation Input				
	P (atm)	**H_2O/CH_4**	**O_2/CH_4**	**T_{SR} (°C)**
FP.A (SR)	1	2.5	-	670
FP.B (ATR)	1	4.0	0.56	-

Table 3.2 Conventional SR/ATR-based Fuel Processor

FP.A shows the highest global efficiency (48.0%) at T_{SR}=670 °C and H_2O/CH_4=2.5. It should be noticed that, in the optimal conditions, methane

conversion (x_{CH4}) is lower than unity; however, the non converted methane is not energetically wasted, since it contributes to the energy content of the AOG, used to sustain the endothermicity of the SR reactor. In this conditions, no addition of methane to the burner is needed (α=0). According to the flowsheet of FP.A, the minimum exhaust gas temperature achievable is 226 °C. Further heat recovery is hindered by temperature cross over in the heat exchangers.

FP.B shows the highest global efficiency (38.5%) at O_2/CH_4=0.56 and H_2O/CH_4=4.0; the value of η is significantly lower than what achieved with FP.A, mainly due to the autothermal nature of the ATR process, that limits the possibility to recover the energy content of the AOG. This reflects into a higher exhaust gas temperature in FP.B (444 °C) than in FP.A (226 °C).

3.2 Fuel Processors with membrane reforming reactor

The simulations on the systems with integrated membrane reactors (FP.C and FP.D) were performed considering pressure and sweep gas to methane inlet ratio (SG/CH_4) as operative parameters to be optimized in the range 3-15 atm and 0-2, respectively.

Simulations with varying pressure and SG/CH_4 ratio were performed in order to achieve the minimum exhaust gas temperature of 100 °C, and this was possible only by varying heat exchanger network configuration when necessary; moreover, in some cases it was not possible to recover all the heat available in the exhaust gases, that leave the system at temperatures higher than 100 °C for the problem of temperature cross-over in the heat exchangers, with a consequent waste of heat in the system. In particular, Figure 3.5 reports the flowsheet of system with FP.C at the conditions that gave the maximum energy efficiency.

Water for the Steam Reforming reactions and for the sweep gas production is preheated by exchanging heat with the stream sent to the PEM fuel cell. After a split, the water for the SR is mixed with methane and preheated in HX-SR; the sweep gas, instead, is produced by sending water to HX-SG1 and HX-SG2, where it exchanges heat with the PERMEATE stream and with exhaust gases that exit from H-B, respectively.

Figure 3.6 reports the flowsheet of system with FP.D with the heat exchanger network that maximize system efficiency.

Water is preheated with the heat available in the stream sent to the PEM fuel cell and in the exhaust gases that exit from HX-ATR, then it is mixed with methane and air and the stream is preheated until 350 °C in HX-ATR, exchanging heat with the stream that exit from the burner. The sweep gas is produced by preheating and vaporizing liquid water with the heat available from the PERMEATE.

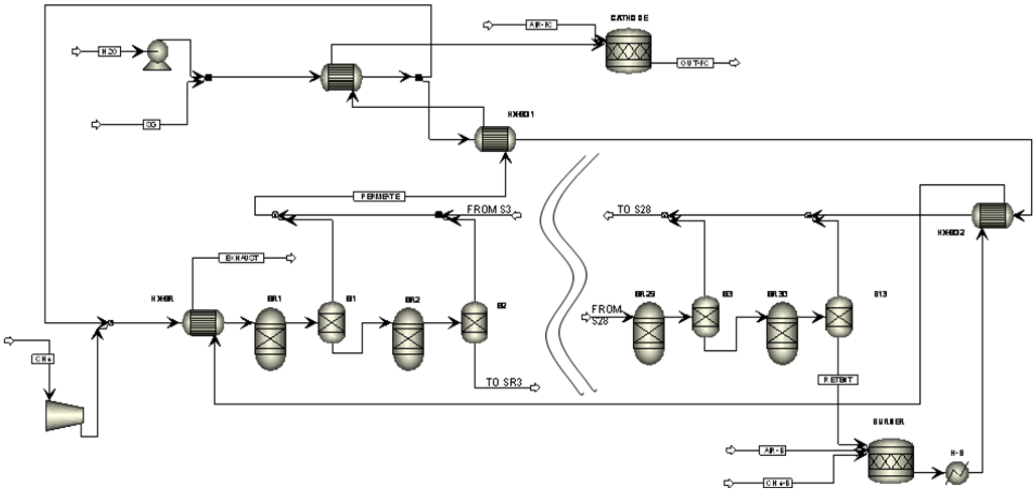

Figure 3.5 Flowsheet of fuel processor FP.F coupled with a PEM fuel cell.

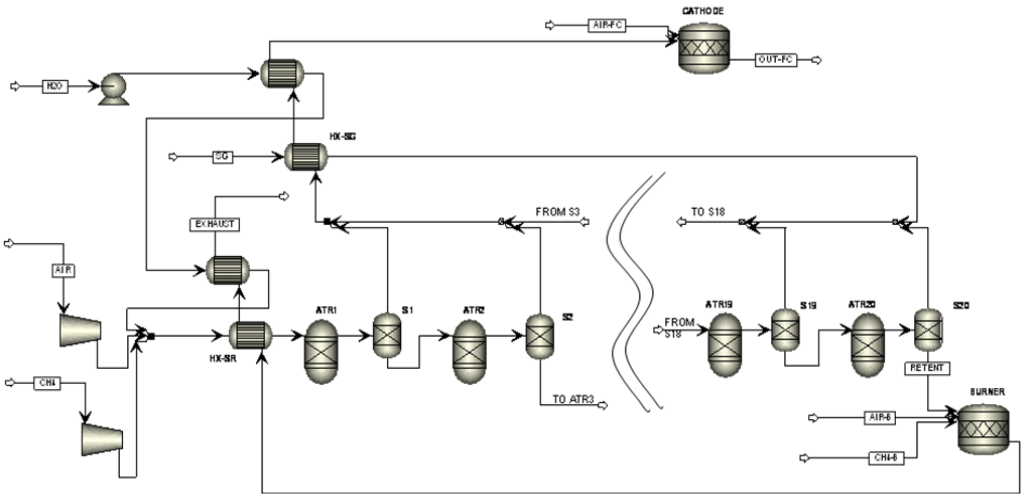

Figure 3.6 Flowsheet of fuel processor FP.F coupled with a PEM fuel cell

Figure 3.7 reports the energy efficiency of system with FP.C as a function of pressure.

Energy efficiency rapidly increases with pressure in the range 3-5 atm, where no methane addition to the burner is required to sustain the endothermic steam reforming reaction.

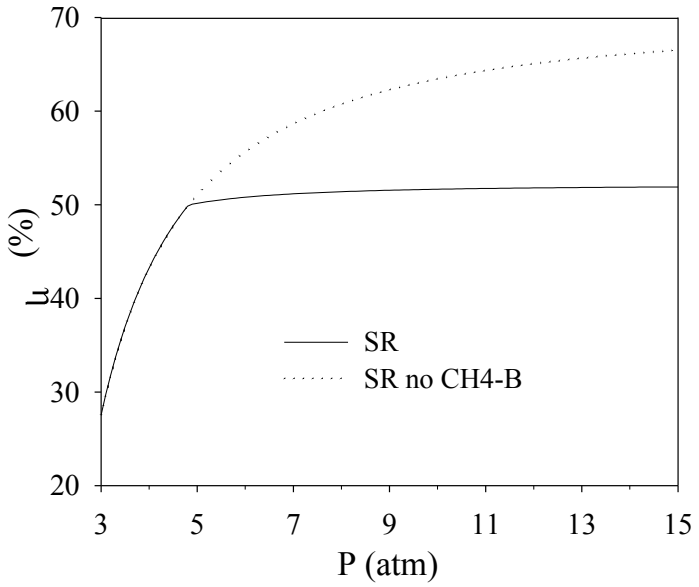

Figure 3.7 η as a function of pressure for system with FP.C. T_{SR} = 600 °C, H_2O/CH_4 = 2.5, SG/CH_4 = 0

As pressure increases above 5 atm ca., η continues to grows with pressure, but at a lower rate, because methane addition to the burner becomes necessary. The dotted line, superimposed to Figure 3.7 as an aid to this discussion, represents the value of η that would be calculated if the methane sent to the burner was not factored in the computation.

The trend of η vs P is the combined effect of hydrogen recovery (HR), reforming factor (f_R), the power of the auxiliary units (related to f_a), whose values are reported in Table 3.3 together with the value of methane conversion (x_{CH4}) and fraction of methane sent to the burner (α)

In particular, HR increases with pressure due to the increase of hydrogen separation driving force through the membrane; f_R increases with pressure because it is positively influenced by the trend of HR with pressure, due to the

positive effect on reaction equilibrium of increasing hydrogen separation. f_a increases with pressure, due to increasing compression ratios. To complete the picture, it should be kept in mind that the heating value of the retentate decreases with pressure, as a consequence of higher x_{CH4} and HR. This, in turn, influences the quantity of methane sent to the burner to sustain the endothermic steam reforming reaction.

P (atm)	x_{CH4}	α	T_{EX} (°C)	HR	fa	f_R	η
3	70.6	0	803.8	58	0.5	80.4	27.5
5	86.3	1.8	100	85.9	0.7	100.5	50.2
7	91.8	12.8	100	91.9	0.9	108.0	51.2
9	94.5	17.2	100	94.4	1.1	111.8	51.5
12	96.6	20.4	100	96.2	1.3	114.9	51.8
15	97.6	22	100	97.1	1.4	116.7	51.9

Table 3.3 Result for system with FP.C. T_{SR} = 600 °C, H_2O/CH_4 = 2.5, SG/CH_4 = 0

In the low pressure range, the positive effect of HR and f_R on energy efficiency overrules the negative effect of f_a and α. The plateau value reached at higher pressure indicates that the drawback of f_a and α compensates the positive effect of HR and f_R.

Figure 3.8 reports the effects of SG/CH_4 on system efficiency of FP.C parametric in pressure, at a fixed outlet exhaust gases temperature of 100 °C. Simulation details for P = 10 atm are reported in Table 3.4.

It is possible to observe that η shows a maximum as a function of SG/CH_4 ratio, which shifts leftwards and upwards as pressure increases. For each pressure value investigated, hydrogen recovery is enhanced by the presence of the sweep gas, as a consequence of reduced hydrogen partial pressure in the permeate side; this leads also to an increase of f_R thanks to the positive effect of hydrogen removal on reactions equilibrium.

However, the production of sweep gas is always coupled with addition of methane to the burner, with an increment of α that can overrule the increment of HR and f_R.

For this reason, being η combination of f_R, HR and α, after an initial small increment, it decreases with addition of sweep gas.

The effect of pressure depends on the SG/CH_4 value. For low SG/CH_4, an increase of pressure causes an increase of η, whereas a decreasing trend of the η with pressure is observed at high SG/CH_4. This is due to the fact that the increment of pressure increases both HR and f_a; when SG/CH_4 is high, HR becomes close to 100% already at low pressure values, therefore an increase of pressure only causes an increase of f_a, with a lowering of η.

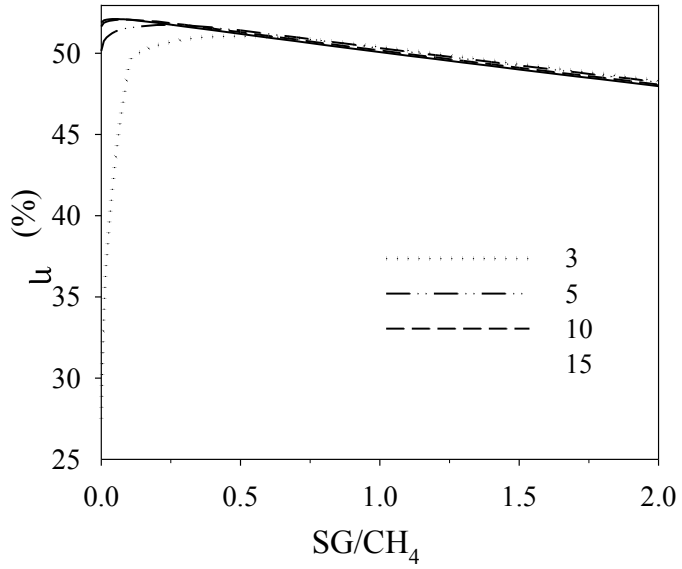

Figure 3.8 η as a function of SG/CH_4 parametric in pressure for system with FP.C. Operating conditions: T_{SR} = 600 °C, H_2O/CH_4 = 2.5

SG/CH_4	**x_{CH4}**	**α**	**T_{EX} (°C)**	**HR**	**fa**	**f_R**	**η**
0.0	95.4	18.6	100.0	95.1	1.1	113.1	51.6
0.1	99.8	25.7	100.0	99.1	1.1	119.8	52.1
0.5	100.0	28.5	100.0	100.0	1.1	121.4	51.3
1.0	100.0	30.0	100.0	100.0	1.1	121.3	50.2
1.5	100.0	31.5	100.0	100.0	1.2	121.3	49.1
2.0	100.0	33.0	100.0	100.0	1.2	121.5	48.1

Table 3.4 Result for system with FP.C. T_{SR} = 600 °C, H_2O/CH_4 = 2.5, P = 10 atm

Table 3.5 report the detail of the simulation results and value of the operating parameters given as simulation input that maximize the energy efficiency η, for FP.C.

The best way to operate a membrane SR system is to increase the pressure without addition of sweep gas.

It is possible to observe that the energy efficiency of a SR-based system is increased if a membrane reactor is used (FP.C), in place of a conventional reactor. This is due to the possibility to recover a higher amount of heat in FP.C than in FP.A. Indeed the heat exchanger network needed in FP.A has to satisfy the temperature requirements of the Shift and PROX reactors resulting in a higher exhaust gas temperature (226 °C), while in FP.C the heat exchanger network allows to cool the exhaust gas to 100 °C (as chosen in the methodology), without any temperature cross over.

Simulation results						
	f_R	**α**	**HR**	**f_a**	**η**	**T_{EX} (°C)**
FP.C (SR)	120.0	25.6	99.2	1.3	52.2	100.0
Simulation Input						
		P (atm)	**H_2O/CH_4**	**T_{SR} (°C)**	**SG/CH_4**	
FP.C (SR)		15	2.5	600	0.1	

Table 3.5 System with FP.C

Figure 3.9 reports energy efficiency of system with FP.D as a function of pressure. As for the case of FP.C, η shows a continuous increase with pressure, but the values are significantly lower, due to limited recovery of the energy contained in the retentate stream and to the negative contribution of the compressor (see T_{ex} and f_a in Table 3.6).

It should be noted that, in FP.D, the maximum value of η (37.2%) is even lower than what is obtained with the conventional ATR reactor (η = 38.5%). This should be attributed to the fact that, notwithstanding the absence of the AOG stream, the dilution of the reacting mixture with nitrogen reduces HR (affecting,

in turn, also x_{CH4}) leading to a retentate with relatively high amount of methane and hydrogen, whose heating value cannot be totally recovered.

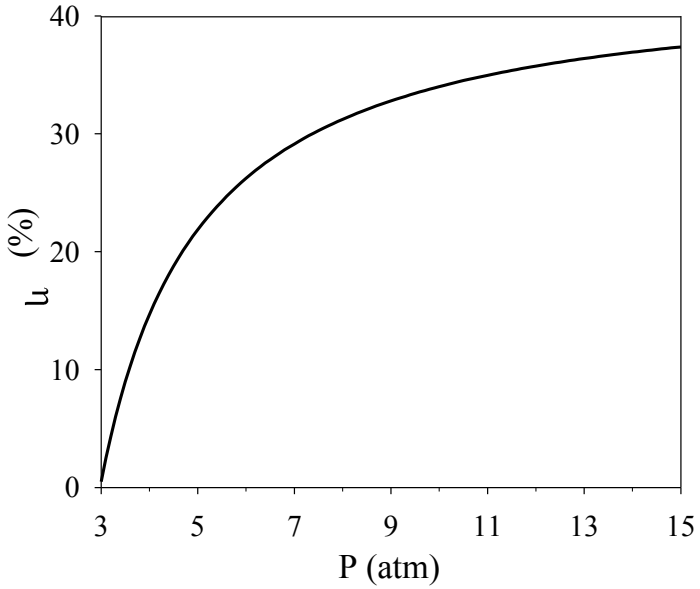

Figure 3.9 η as a function of pressure for system with FP.D. Operating conditions: $O_2/CH_4 = 0.48$, $H_2O/CH_4 = 1.15$, $SG/CH_4 = 0$

It should be pointed out that, due to the exothermic nature of the reactions, no additional methane to the burner is required, i.e. α=0, and the exhaust gas stream leaves the plant at quite high temperatures. Data are reported in Table 3.6.

P (atm)	x_{CH4}	α	T_{EX} (°C)	HR	fa	f_R	η
3.0	85.2	0.0	1369.1	5.8	1.6	60.1	0.5
5.0	88.4	0.0	1248.1	60.2	2.6	67.6	21.8
7.0	90.0	0.0	1178.1	75.6	3.3	71.4	29.1
9.0	90.9	0.0	1132.7	82.7	3.9	73.8	32.7
12.0	91.8	0.0	1089.8	88.0	4.6	76.2	35.6
15.0	92.4	0.0	1063.6	90.9	5.2	77.8	37.2

Table 3.6 Result for system with FP.D. O_2/CH_4=0.48, H_2O/CH_4=1.15, SG/CH_4=0

Fig. 3.10 reports the energy efficiency of system with FP.D as a function of SG/CH_4 parametric in pressure. Simulation details for P = 10 atm are reported in Table 3.7.

The trend of η with SG/CH_4 and pressure is similar to the one observed for the system based on SR. However, it is important to note that for each pressure value investigated, the SG/CH_4 value that maximize energy efficiency is higher than the corresponding one in the SR-based fuel processor.

This is due to the fact that in an ATR-based system, there is an excess energy due to the autothermic nature of the process, that allows a consistent sweep gas production without methane addition to the burner, i.e. α = 0.

Moreover, it is worth noting that energy efficiency of FP.D is highly improved by adding sweep gas, increasing from 34.0% (SG/CH_4 = 0) to 50.3% (SG/CH_4 = 1.0).

Table 3.8 reports the detail of the simulation results and value of the operating parameters given as simulation input that maximize the energy efficiency η, for FP.D. The best way to operate an autothermal reforming membrane system is to moderately increase pressure and to employ some sweep gas to improve HR (the maximum η is reached for P = 7 atm and SG/CH_4 = 1.0, as reported in Table 3.7).

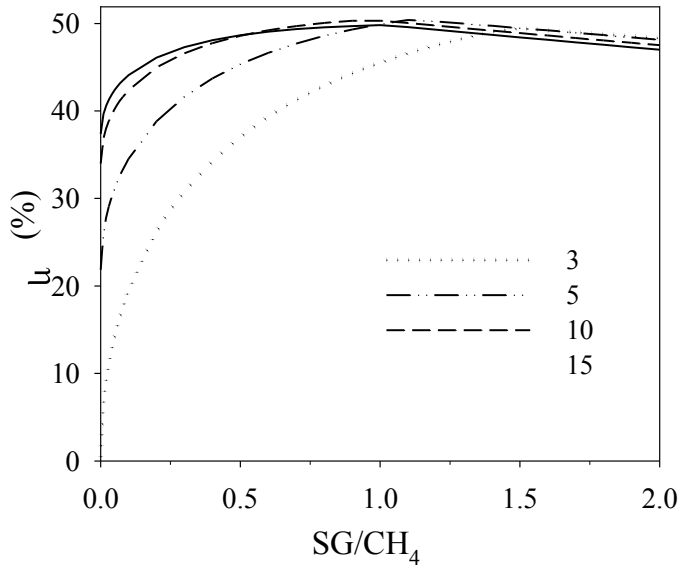

Figure 3.10 η as a function SG/CH_4 parametric in pressure for system with FP.D. O_2/CH_4 = 0.48, H_2O/CH_4 = 1.15

SG/CH_4	x_{CH4}	α	T_{EX} (°C)	HR	fa	f_R	η
0.0	91.3	0.0	1115.9	84.9	4.1	74.8	34.0
0.1	95.1	0.0	894.7	95	4.1	81.5	42.4
0.5	99.1	0.0	463.8	99.1	4.1	88.6	48.6
1.0	100	0.4	100.0	99.9	4.1	91.2	50.3
1.5	100	4.0	100.0	100.0	4.1	91.8	48.9
2.0	100	7.0	100.0	100.0	4.1	91.9	47.5

Table 3.7 Results for system with FP.D. O_2/CH_4=0.48, H_2O/CH_4=1.15, P=10 atm

The lower value of pressure that maximize η with respect to SR system is due to the higher power required by the auxiliary units, needed essentially to compress the air in the feed.

Simulation results						
	f_R	α	HR	f_a	η	T_{EX} (°C)
FP.D	90.2	0.0	99.6	3.3	50.6	100.0
Simulation Input						
		P (atm)	H_2O/CH_4	O_2/CH_4	SG/CH_4	
FP.D (ATR)		7	1.2	0.5	1.0	

Table 3.8 System with FP.D

Finally, it should be noted that the addition of sweep gas in system with FP.D allows to reach energy efficiency values significantly higher than the optimum value of the conventional system (38.5%) and similar to the energy efficiency of SR based systems.

It should be kept in mind that, due to limited thermal stability of the highly selective membranes, membrane units should not be exposed to temperatures higher than 600 °C. While FP.C always meets this constraint (since reactor temperature is fixed at 600 °C), FP. D does not. Indeed, in the optimal conditions, the first reactors reach temperatures as high as 720 °C. Therefore, the actual realization of an integrated membrane reactor would require significant improvements of membrane compatibility with high temperatures. A more realistic configuration of an ATR based membrane reactor should consider a first

ATR reactor, where most of the methane oxidation takes place, followed by a membrane reactor, interposing between the two units a heat exchanger to cool down the temperature before entrance into the membrane reactor, so that the membranes are never exposed to temperatures higher than 600 °C. With this configuration, energy efficiency becomes 48.5% and the best operating conditions are P = 7 atm; $O_2/CH_4 = 0.5$; $H_2O/CH_4 = 1.7$; $SG/CH_4 = 1.0$.

3.3 Fuel Processors based on membrane WGS reactor

Optimization performed for systems based on membrane WGS reactors (FP.E for SR and FP.F for ATR) followed the same criteria of what reported for systems based on membrane reforming reactors. Although quantitatively different, the trend of performance with operating parameters were similar to what reported for the systems with membrane reforming reactors, therefore data are not reported for the sake of brevity.

Table 3.9 reports the simulation results and the value of the operating parameters given as simulation input that maximize the energy efficiency η, for FP.E and for FP.F, respectively.

It is possible to observe that the introduction of the membrane in the WGS reactor allows to obtain higher energy efficiencies than what achieved in the conventional systems.

Simulation results						
	f_R	**α**	**HR**	**fa**	**η**	**T_{EX} (°C)**
FP.E (SR)	110.9	18.4	96.8	0.5	52.2	141.5
FP.F (ATR)	83.0	0.0	99.4	1.9	47.6	100.0
Simulation Input						
	P (atm)	**H_2O/CH_4**	**O_2/CH_4**	**SG/CH_4**	**T_{SR} (°C)**	**T_{WGS} (°C)**
FP.E (SR)	3	2.0	-	0.2	800	300
FP.F (ATR)	3	1.2	0.6	1.9	-	300

Table 3.9 Innovative systems based on membrane WGS reactor

As far as system with FP.E is concerned, the temperature value required for system optimization corresponds to the highest value investigated; this is due to the positive effect of temperature on the SR reactor, and thus on the membrane WGS reactor, that overcomes the negative effect of temperature increase on α.

The maximum efficiency value is limited by the problem of a not complete heat recovery of the exhaust gases (T_{EX}>100 °C); this is due to the problem of temperature cross-over that can arise in the heat exchangers when the system works at high SR temperatures.

Since the endothermic nature of the process imposes the necessity of operating with additional methane to the burner, the amount of sweep gas required to optimize the system is small (SG/CH_4=0.2).

It is also possible to observe that the pressure value required for system optimization corresponds to the lowest value investigated; this is due to the negative effect of pressure on the SR reactor, that overcomes the positive effect of pressure increase on the membrane WGS reactor. This one, indeed, allows to reach a high HR, notwithstanding the low pressure value, thanks to the high hydrogen concentration achieved at the outlet of the SR reactor, that positively acts on the driving force.

As far as system with FP.F is concerned, it is possible to observe that the value of H_2O/CH_4 that maximize the energy efficiency is by far lower than what required for the conventional case. For the ATR systems, indeed, the autothermal nature of the process allows to have an excess heat in the system that can be used to produce steam. In the conventional system, the steam can be used only as reactant, with only moderate improvement of energy efficiency for H_2O/CH_4>3, thus making further steam production useless. In the innovative system, the steam can be used as reactant as well as sweep gas and the energy efficiency resulted to be favoured more by an increase of SG/CH_4 than by an increase of H_2O/CH_4.

The autothermal nature of the process allows to operate with no additional methane to the burner and the high amount of sweep gas allows the system to operate at low pressure values, favoring the conditions in the ATR reactor.

Although working at the same pressure, the fraction of inlet methane required to run the auxiliary unit is higher in the ATR case than in the SR case, for the presence of air in the feed (f_a=0.5 for FP.E and 1.9 for FP.F).

It is also possible to note that the introduction of the membrane in the WGS reactor not only allows to reach efficiency values higher than what achieved in the conventional systems, but also makes the SR and ATR based systems similar in terms of energy efficiency (the difference between SR and ATR in the conventional case is ca. 20%, whereas in this case it is only ca. 8%).

3.4 Final considerations

As a general conclusion on system analysis, the optimum of each fuel processor – PEMFC system and the corresponding operating parameters are reported in Table 3.10.

It is possible to observe that the SR-based processes always show a higher energy efficiency than the corresponding ATR-based processes, with a marked difference in the case of conventional systems (FP.A and FP.B have a difference of about 21% in the energy efficiency value). However, the introduction of the membrane allows to obtain energy efficiency values of the ATR system closer to the efficiency levels reached in the SR ones (differences between SR and ATR based systems of ca. 7% when the membrane is introduced in the reforming reactor and of ca. 9% when the membrane is introduced in the WGS reactor).

	Case	**H_2O/CH_4**	**O_2/CH_4**	**T_{SR} [°C]**	**SG/CH_4**	**P [atm]**	**η %**
SR	FP.A	2.5	-	670	-	1	48.0
	FP.C	2.5	-	600	0.1	15	52.1
	FP.E	2.0	-	800	0.2	3	52.2
ATR	FP.B	4.0	0.56	-	-	1	38.5
	FP.D	1.7	0.5	-	1.0	7	48.5
	FP.F	1.2	0.6	-	1.9	3	47.6

Table 3.10 Comparison of FP – PEMFC systems in correspondence of operating conditions that maximize system performance

The comparison between the steam reforming based systems (innovative systems with FP.C and FP.E vs conventional system with FP.A) showed that the employment of a membrane reactor can increase system efficiency from 48.0% to values above 52.0%. Such an efficiency increase requires almost no addition of sweep gas due to the endothermic nature of the process.

The pressure that optimizes the energy efficiency of the two membrane-based system is different; the system with integrated reforming reactor (FP.C) requires to operate at high pressure value (15 atm), whereas the system with membrane WGS reactor (FP.E) at low pressure value (3 atm). This is due to the fact that the SR reactor is negatively influenced by the pressure increase, therefore the system is optimized by increasing the hydrogen recovery in the membrane WGS reactor by increasing hydrogen concentration at the inlet of the WGS reactor more than by increasing pressure.

As regards temperature, all systems require to operate at the highest possible temperature compatible with material stability.

However, although the limit on temperature imposed to the system with membrane reforming reactor is more tighten, energy efficiency results to be the as high as the value reached in the system with membrane WGS reactor, that operates at high SR temperature. This is due to the fact than the hydrogen removal from the reaction environment allows to achieve higher performance at lower temperature.

The comparison between the autothermal reforming systems (innovative systems with FP.D and FP.F vs conventional system FP.B) shows that energy efficiency can be improved from 38.5% to values around 48%, if a membrane reactor is employed. To obtain such an energy efficiency improvement, sweep gas addition is required.

The considerations on pressure are the same of what reported for the SR case, although the system with membrane reforming reactor is optimized at pressure values lower that the SR case (7 atm instead of 15 atm) due to the higher value of power required to run the auxiliary units.

It is possible to observe that the value of H_2O/CH_4 that maximize the energy efficiency of the innovative ATR systems, is far lower than what required for the conventional case.

Indeed, in the innovative systems, the steam can be used as reactant and as sweep gas and the energy efficiency resulted to be favoured more by an increase of SG/CH_4 than by an increase of H_2O/CH_4.

System analysis: Results - Ethanol

As reported in the introduction, in recent years, Proton Exchange Membrane Fuel Cells (PEMFC) fed with hydrogen have received a large attention for power generation for mobile and stationary applications, due to the capability of generating power with high efficiency, reduced on-site emissions and fast response to load changes.

When the hydrogen source is a fossil fuel, the advantage of PEMFC based systems is the high fuel to electricity conversion efficiency, significantly higher than what achieved with internal combustion engines [117].

If the fuel is extracted from biomass (bio-fuels), the high energy efficiency is accompaigned by zero CO_2 emissions. Among bio-fuels, bio-ethanol represents a promising hydrogen source, being non toxic, easy to store and transport and with relatively high hydrogen content.

Bio-ethanol is produced by fermentation of biomasses such as organic wastes and energy agricultural plants resulting in a fermentation broth, commonly referred to as crude bio-ethanol, containing ca. 5-10 % molar of bio-ethanol [118-120]. A bio-ethanol rich solution is then generally distilled from the broth to obtain the desired purity level.

Although several authors have addressed the thermodynamic analysis of fuel processor – PEMFC systems [121-124, 84-86], only few contributions are available when ethanol is used as fuel.

In particular, Francesconi et al. [113] analyzed the performance of a SR-based fuel processor – PEMFC system fed with ethanol, concluding that the system is energetically convenient with respect to internal combustion engines.

Manzolini et al. [84] analyzed a SR-based fuel processor coupled with a PEMFC, showing that a higher global energy efficiency can be achieved if a membrane reactor is employed instead of a conventional reactor.

In order to have an idea of the efficiency of the fuel processor – PEM fuel cell systems when a renewable source is employed as fuel, this chapter analyzes the efficiency of the systems fed with ethanol and bio-ethanol. In particular, the analysis was performed on conventional fuel processors (FP.A and FP.B) and innovative fuel processors based on membrane reforming reactors (FP.C and FP.D).

The methology for performing the analysis was the same of what reported for methane. The only difference is in the case of bio-ethanol, that was simulated as a mixture of ethanol and water, with molar ratio of 10 [118-119]. Therefore, also the bio-ethanol fed to the burner will contain water and the simulations were performed without adding water to the fuel processor, since it is already contained in the inlet fuel.

Moreover, the following parameter was defined in order to present the results:

$$f_{ex} = \frac{Q}{(n_E + \iota_{E,B}) \cdot HHV_E}$$

that represents the fraction of ethanol inlet energy lost with the exhaust gases; Q is energy content of the exhaust gas stream, with respect to 25 °C, liquid water.

4.1 Ethanol Reforming

Table 4.1 reports the simulation results and the value of the operative parameters given as simulation input that maximize the global efficiency, η, for conventional systems, when ethanol is employed as fuel. The details of the main streams in terms of product composition, temperature and pressure are reported in Table 4.2.

Simulation results						
	System Efficiency				*Exhaust Gases*	
	α	η_e	f_a	η	f_{ex}	T_{Ex} (°C)
FP.A (SR)	0.0	48.1	-	48.1	10.8	100
FP.B (ATR)	0.0	38.0	-	38.0	29.4	380
Operating Conditions						
	P (atm)	**H_2O/E**	**O_2/E**	**T_{SR} (°C)**	**SG/E**	
FP.A (SR)	1	4.2	-	750.0	-	
FP.B (ATR)	1	5.8	0.7	-	-	

Table 4.1 Simulation results in optimum for FP.A and FP.B. Fuel: Ethanol

Simulations on the conventional systems were performed at 1 atm exploring as operative parameters the molar ratio between water and ethanol at reactor inlet (H_2O/E) and reactor temperature T_{SR}, for the SR based fuel processor (FP.A), and water to ethanol and oxygen to ethanol (O_2/E) inlet ratio, for the ATR based fuel processor (FP.B).

FP.A shows the highest global efficiency (48.1%) at T_{SR} = 750 °C and H_2O/E = 4.2. In the optimum conditions no addition of ethanol to the burner is needed (α = 0) and the maximum possible amount of energy is recovered from the AOG to sustain the endothermicity of the SR reactor, with the given constraint of exhaust gases temperature equals to 100 °C. In these conditions, the amount of ethanol inlet energy lost with the exhaust gases f_{ex} is 10.8%.

FP.B shows the highest global efficiency (38.0%) at O_2/E = 0.7 and H_2O/E = 5.8; the value of η is significantly lower than what achieved with FP.A, mainly due to the autothermal nature of the ATR process, that limits the possibility to recover the energy content of the AOG; indeed, in this condition the exhaust gases temperature reaches 380 °C and f_{ex} = 29.4%.

The simulations on the systems with integrated membrane reactors (FP.C and FP.D) were performed considering also pressure and sweep gas to ethanol inlet ratio (SG/E) as operative parameters to be optimized in the range 3 - 15 atm and 0 - 2, respectively.

FP.A	SR		HTS		LTS		PROX		PEMFC	
	IN	OUT	IN	OUT	IN	OUT	IN	OUT	AOG	H2
E (%)	19.3	-	-	-	-	-	-	-	-	-
H_2 (%)	-	51.9	51.9	59.3	59.3	63.8	59.0	57.8	25.5	100
CH_4 (%)	-	0.1	0.1	0.1	0.1	0.1	0.1	0.1	0.2	-
CO (%)	-	13	13	5.6	5.6	1.1	1	-	-	-
CO_2 (%)	-	8.7	8.7	16.0	16.0	20.6	19.0	20.3	35.9	-
H_2O (%)	80.7	26.3	26.3	19.0	19.0	14.4	13.4	15.5	27.4	-
O_2 (%)	-	-	-	-	-	-	1.5	-	-	-
N_2 (%)	-	-	-	-	-	-	6.0	6.3	11.0	-
T (°C)	750	750	350	434	200	255	90	90	80	80
P (atm)	1	1	1	1	1	1	1	1	1	1
FP.B	**ATR**		**HTS**		**LTS**		**PROX**		**PEMFC**	
	IN	OUT	IN	OUT	IN	OUT	IN	OUT	AOG	H2
E (%)	9.7	-	-	-	-	-	-	-	-	-
H_2 (%)	-	29.3	29.3	32.2	32.2	33.1	32.9	32.7	10.8	100
CH_4 (%)	-	0.2	0.2	0.2	0.2	0.2	0.2	0.2	0.3	-
CO (%)	-	3.8	3.8	0.9	0.9	0.1	0.1	-	-	-
CO_2 (%)	-	10.7	10.7	13.6	13.6	14.5	14.4	14.5	19.2	-
H_2O (%)	56.3	35.3	35.3	32.4	32.4	31.5	31.3	31.5	41.8	-
O_2 (%)	6.8	-	-	-	-	-	0.1	-	-	-
N_2 (%)	27.2	20.7	20.7	20.7	20.7	20.6	21.0	21.1	27.9	-
T (°C)	350	627	350	383	200	210	90	90	80	80
P (atm)	1	1	1	1	1	1	1	1	1	1

Table 4.2 Input and Output data for FP.A and FP.B. Fuel: Ethanol

Table 4.3 reports the simulation results for FP.C when pressure is employed as variable and SG/E is set to zero.

		System Efficiency				*Exhaust Gases*	
P (atm)	**HR**	α	η_e	f_a	η	f_{ex}	T_{ex} (°C)
3.0	31.9	0.0	11.9	0.0	11.9	75.8	992.3
5.0	79.5	0.0	41.6	0.0	41.6	22.5	424.7
7.0	88.5	4.7	51.3	0.0	48.9	9.3	100.0
10.0	93.2	13.7	57.6	0.0	49.7	7.8	100.0
12.0	94.7	16.4	59.7	0.0	49.9	7.3	100.0
15.0	96.0	18.8	61.8	0.0	50.1	6.9	100.0

Table 4.3 Simulation results for FP.C. Operating conditions: SG/E = 0; H_2O/E = 4.0; T_{SR} = 600 °C. Fuel: Ethanol

Hydrogen recovery HR shows a continuous increase with pressure, due to the positive effect of pressure on the hydrogen separation driving force through the membrane.

Global efficiency η shows a continuous increase with pressure, with a plateau equal to ca. 50% reached at the highest pressure values investigated. In order to understand the effect of pressure on η, it should be kept in mind that the global efficiency is the combination of: i) electric energy output η_e, related to the molar flow of hydrogen sent to the fuel cell n_{H2}, ii) fraction of inlet ethanol energy required for reactants compression f_a, iii) fraction of ethanol sent to the burner to sustain the endothermic steam reforming reactions α. In particular, η_e increases with pressure, due to the enhancement of HR that allows to obtain an increase of the molar flow of hydrogen removed from the reforming unit, which, in turn, positively influences the equilibrium of some of the reactions involved in the reforming unit (i.e., methane reforming and water gas shift reactions); α increases with pressure, due to the decrease of the heating value of the retentate; f_a is always negligible in the pressure range investigated, being the feed in liquid state. For pressure values up to 10 atm, the increase of η_e is higher than the increase of α, leading to a positive effect of pressure on η; above 10 atm, the increase of η_e is comparable with the increase of α, leading to a negligible effect of pressure on η.

It is important to note that the maximum global efficiency of FP.C (50.1%) is higher than what is achieved in the conventional case (48.1%). Therefore, less energy is wasted in the exhaust gases of FP.C. This holds true notwithstanding the same exhaust gases temperature (100 °C) in the two fuel processors, due to a higher flow rate of exhaust gases and to their higher water content in FP.A.

Table 4.4 reports the simulation results for FP.D when pressure is employed as variable and SG/E is set to zero.

For P = 3 atm, the power required for reactants compression exceeds the electric power produced by the fuel cell, therefore η becomes negative, and its value was not reported in the table.

As for the case of FP.C, η shows a continuous increase with pressure, but the values are significantly lower, due to limited recovery of the energy contained in

the exhaust gases and to the energy needed for air compression (see T_{ex}, f_{ex} and f_a in Table 4.4). The highest global efficiency η (39.8%) is achieved at P = 15atm.

		System Efficiency				*Exhaust Gases*	
P (atm)	**HR**	α	η_e	f_a	η	f_{ex}	T_{ex} (°C)
3.0	0.6	0.0	0.2	0.9	-	97.5	1322.4
5.0	59.7	0.0	23.6	1.4	22.2	56.0	1162.1
7.0	75.7	0.0	32.0	1.8	30.2	41.3	1059.2
10.0	85.2	0.0	38.0	2.2	35.7	31.0	956.2
12.0	88.3	0.0	40.3	2.5	37.8	27.1	907.3
15.0	91.2	0.0	42.6	2.8	39.8	23.2	851.7

Table 4.4 Simulation results for FP.D. Operating conditions: SG/E = 0; H_2O/E = 2.1; O_2/E = 0.6. Fuel: Ethanol

It should be noted that, in FP.D, the maximum value of η (39.8%) is higher than what obtained with the conventional ATR reactor (η = 38.0% for FP.B). This should be attributed to the lower amount of water needed to optimize FP.D (H_2O/E = 2.1) with respect to the water needed to optimize FP.B (H_2O/E = 5.8). Nevertheless, notwithstanding the employment of the membrane reactor, the global efficiency of FP.D remains well below the values typical of SR-based systems (FP.A and FP.C).

Figure 4.1 a-b reports hydrogen recovery HR and global efficiency η of FP.C and FP.D as a function of SG/E at constant pressure (10 atm). Simulation details are reported in Tables 4.5 and 4.6.

HR shows a continuous increase with SG/E both for FP.C and FP.D; this is due to the positive effect of sweep gas on the hydrogen separation driving force through the membrane.

Global efficiency η shows a non monotone trend as a function of SG/E both for FP.C and FP.D. Indeed, the addition of sweep gas on the permeate side of the membrane leads to: i) increase of the molar flow of hydrogen sent to the fuel cell (see η_e in Table 4.5 and 4.6) due to the increase of HR and, thus, of hydrogen production in the reforming unit, ii) increase of the fraction of ethanol that must

sent to burner α, consequence of the reduction of the heating content of the retentate stream with SG/E. The position of the maximum of the global efficiency depends on the relative weight of these two factors. In particular, the highest global efficiency (50.2%) for FP.C is achieved at SG/E = 0.1, whereas the highest global efficiency (50.5%) for FP.D is achieved at SG/E = 0.7.

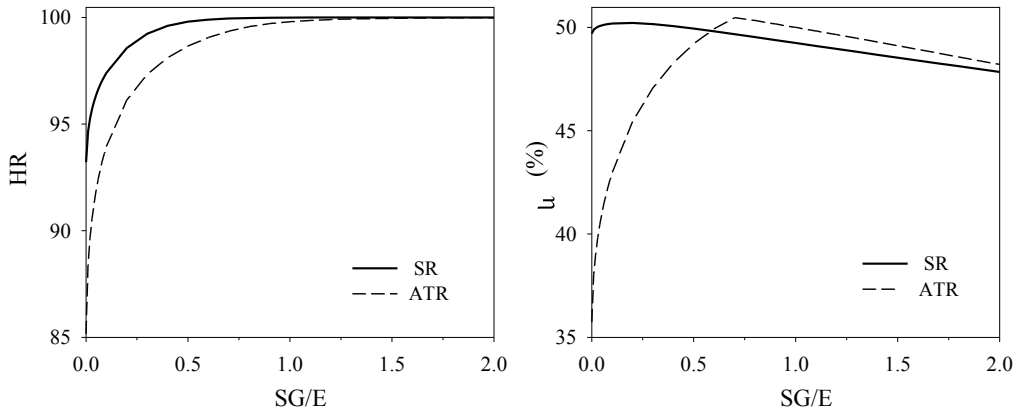

Figure 4.1 Hydrogen recovery HR (a) and global efficiency η (b) as a function of SG/E ratio for FP.C (continuous line) and FP.D (dashed line). Fuel: Ethanol

		System Efficiency				*Exhaust Gases*	
SG/E	**HR**	**α**	**η_e**	**f_a**	**η**	**f_{ex}**	**T_{ex} (°C)**
0.0	93.2	13.7	57.6	0.0	49.7	7.8	100.0
0.1	97.4	21.4	63.8	0.0	50.2	6.6	100.0
0.5	99.8	26.3	67.7	0.0	49.9	6.0	100.0
1.0	> 99.9	27.7	68.1	0.0	49.2	6.0	100.0
1.5	> 99.9	28.8	68.1	0.0	48.5	6.1	100.0
2.0	> 99.9	29.8	68.1	0.0	47.8	6.2	100.0

Table 4.5 Simulation results for FP.C. Operating conditions: $H_2O/E = 4.0$; T_{SR} = 600 °C; P = 10atm. Fuel: Ethanol

It is important to note that global efficiency of FP.D can be highly improved by adding sweep gas, increasing from 35.7% (SG/E = 0) to 50.5% (SG/E = 0.7), reaching values comparable with SR-based systems. Indeed, the presence of

sweep gas allows to recover the energy content of the exhaust gases, reducing their outlet temperature to the minimum one (100 °C).

		System Efficiency				*Exhaust Gases*	
SG/E	**HR**	**α**	**η_e**	**f_a**	**η**	**f_{ex}**	**T_{ex} (°C)**
0.0	85.2	0	38.0	2.2	35.7	31.0	956.2
0.1	93.9	0	45.2	2.2	43.0	18.1	741.6
0.5	98.6	0	51.4	2.2	49.2	7.4	429.4
1.0	99.8	2.9	53.7	2.2	50.0	2.0	100.0
1.5	99.9	5.6	54.2	2.2	49.1	2.1	100.0
2.0	> 99.9	7.6	54.4	2.2	48.2	2.3	100.0

Table 4.6 Simulation results for FP.D. Operating conditions: $H_2O/E = 2.1$; $O_2/E = 0.6$; P = 10atm. Fuel: Ethanol

Table 4.7 reports the simulation results and the value of the operative parameters P and SG/E that maximize the global efficiency for FP.C and FP.D, respectively. The details of the main streams in terms of product composition, temperature and pressure are reported in Table 4.8.

Simulation results						
	System Efficiency				*Exhaust Gases*	
	α	**η_e**	**f_a**	**η**	**f_{ex}**	**T_{ex} (°C)**
FP.C (SR)	23.4	65.8	0	50.4	6.2	100.0
FP.D (ATR)	-	53.1	2.6	50.6	1.9	100.0
Operating Conditions						
	P (atm)	**H_2O/E**	**O_2/E**	**T_{SR} (°C)**	**SG/E**	
FP.C (SR)	14.0	4.0	-	600.0	0.1	
FP.D (ATR)	13.0	2.1	0.6	-	0.6	

Table 4.7 Simulation results in optimum for FP.C and FP.D. Fuel: Ethanol

The results indicate that the best way to operate a membrane SR system (FP.C) is to increase the pressure with no need of sweep gas, whereas the membrane ATR system (FP.D) reaches the best global efficiency by operating at high pressure value with significant amounts of sweep gas.

In particular, the membrane SR system presents a maximum global efficiency of 50.4%, with a gain of 5% with respect to the conventional case, whereas the maximum global efficiency of the membrane ATR system is equal to 50.6%, with a gain of 33% with respect to the conventional case. These results indicate that the introduction of the membrane in the ATR-based systems allows to greatly increase the global efficiency with respect to the conventional case, leading to the same values achieved by the SR-based system.

	FP.C		FP.D	
	RETENTATE	PERMEATE	RETENTATE	PERMEATE
E (%)	-	-	-	-
H_2 (%)	2.6	98.3	0.4	88.6
CH_4 (%)	0.3	-	2E-2	-
CO (%)	2.9	-	2.0	-
CO_2 (%)	59.5	-	39.5	-
H_2O (%)	34.7	1.7	8.2	11.4
O_2 (%)	-	-	-	-
N_2 (%)	-	-	49.9	-
T (°C)	600	600	591	682
P (atm)	14	1	13	1

Table 4.8 Input and Output data of main units for FP.C and FP.D. Fuel: Ethanol

It is worth noting that the negative effect on global efficiency of the power required for reactants compression is much lower than in the case of gaseous fuels [85]. For this reason, the best global efficiency is achieved at high pressure values, both for SR and ATR-based systems.

4.2 Crude-Ethanol Reforming

Table 4.9 reports the simulation results and the value of the operative parameters that maximize the global efficiency η, for conventional systems (FP.A and FP.B), when crude-ethanol is employed as fuel. The details of the main streams in terms of product composition, temperature and pressure are reported in Table 4.10.

Simulations on the conventional systems were performed at 1 atm, exploring as operative parameters reactor temperature T_{SR} for FP.A and oxygen to ethanol O_2/E inlet ratio for FP.B.

Simulation results						
	System Efficiency				***Exhaust Gases***	
	α	**η_e**	**f_a**	**η**	**f_{ex}**	**T_{ex} (°C)**
FP.A (SR)	37.6	48.6	-	30.3	36.9	100.0
FP.B (ATR)	10.1	34.0	-	30.5	36.6	100.0
Operating Conditions						
	P (atm)	**H_2O/E**	**O_2/E**	**T_{SR} (°C)**	**SG/E**	
FP.A (SR)	1.0	10.0	-	600.0	-	
FP.B (ATR)	1.0	10.0	1.0	-	-	

Table 4.9 Simulation results in optimum for FP.A and FP.B. Fuel: Crude-ethanol

FP.A	**SR**		**HTS**		**LTS**		**PROX**		**PEMFC**	
	IN	**OUT**	**IN**	**OUT**	**IN**	**OUT**	**IN**	**OUT**	**AOG**	**H2**
E (%)	9.1	-	-	-	-	-	-	-	-	-
H_2 (%)	-	35.8	35.8	37.9	37.9	38.5	38.3	38.2	13.4	100
CH_4 (%)	-	0.5	0.5	0.5	0.5	0.5	0.5	0.5	0.6	-
CO (%)	-	2.7	2.7	0.6	0.6	5E-2	5E-2	-	-	-
CO_2 (%)	-	10.3	10.3	12.4	12.4	12.9	12.9	13.0	18.2	-
H_2O (%)	90.9	50.7	50.7	48.6	48.6	48.1	47.9	48.0	67.4	-
O_2 (%)	-	-	-	-	-	-	7E-2	-	-	-
N_2 (%)	-	-	-	-	-	-	0.3	0.3	0.4	-
T (°C)	600	600	350	373	200	206	90	90	80	80
P (atm)	1	1	1	1	1	1	1	1	1	1
FP.B	**SR**		**HTS**		**LTS**		**PROX**		**PEMFC**	
	IN	**OUT**	**IN**	**OUT**	**IN**	**OUT**	**IN**	**OUT**	**AOG**	**H2**
E (%)	6.3	-	-	-	-	-	-	-	-	-
H_2 (%)	-	18.7	18.7	20.8	20.8	21.0	21.0	21.0	6.2	100
CH_4 (%)	-	-	-	-	-	-	-	-	-	-
CO (%)	-	2.3	2.3	0.3	0.3	2E-2	2E-2	-	-	-
CO_2 (%)	-	8.2	8.2	10.3	10.3	10.5	10.5	10.5	12.5	-
H_2O (%)	62.5	49.7	49.7	47.6	47.6	47.4	47.3	47.4	56.2	-
O_2 (%)	6.3	-	-	-	-	-	3E-2	-	-	-
N_2 (%)	24.9	21.1	21.1	21.1	21.1	21.1	21.1	21.1	25.1	-
T (°C)	600	600	350	373	200	206	90	90	80	80
P (atm)	1	1	1	1	1	1	1	1	1	1

Table 4.10 Input and Output data for FP.A and FP.B. Fuel: Crude-ethanol

FP.A shows a constant global efficiency (30.3%) in the range T_{SR} = 500-1000 °C. Indeed, as soon as fuel is needed in the burner, the global efficiency levels off.
FP.B shows the highest global efficiency (30.5%) at O_2/E = 1.0.
The global efficiency of both FP.A and FP.B are both much lower when crude-ethanol is employed instead of pure ethanol. Indeed, as reported by Ioannides [125], a decrement in hydrogen production efficiency from ethanol is found when water to ethanol inlet ratio greatly exceeds the stoichiometric value, i.e. 3. Indeed, more fuel needs to be sent to the burner to provide the energy required for feed vaporization. This results in a loss of global efficiency. Furthermore, a higher quantity of water is present in the exhaust gases, thus increasing f_{ex}.
It is important to note that the conventional ATR and SR systems show a similar global efficiency, when crude-ethanol is employed as fuel. This happens because in both processes the energy content of the exhaust gases is recovered up to maximum, i.e. outlet temperature equals to 100 °C.

The simulations on the systems with integrated membrane reactors (FP.C and FP.D) with crude-ethanol were performed considering also pressure and sweep gas to ethanol inlet ratio (SG/E) as operative parameters to be optimized in the range 3 - 15 atm and 0 - 2, respectively.
Table 4.11 reports the simulation results and the value of the operative parameters P and SG/E that maximize the global efficiency η, for FP.C and FP.D. The details of the main streams in terms of product composition, temperature and pressure are reported in Table 4.12.

Simulation results						
	System Efficiency				***Exhaust Gases***	
	α	**η_e**	**f_a**	**η**	**f_{ex}**	**T_{ex} (°C)**
FP.C (SR)	40.5	57.5	0.0	34.1	35.6	100.0
FP.D (ATR)	1.1	37.0	2.8	33.8	34.6	100.0
Operating Conditions						
	P (atm)	**H_2O/E**	**O_2/E**	**T_{SR} (°C)**	**SG/E**	
FP.C (SR)	13.0	10.0	-	600.0	0.0	
FP.D (ATR)	14.0	10.0	0.6	-	0.0	

Table 4.11 Simulation results in optimum for FP.C and FP.D. Fuel: Crude-ethanol

Both for FP.C and FP.D, the best global efficiency is achieved at high pressure values, as in the case of pure ethanol. On the other hand, when crude-ethanol is employed, no sweep gas is required to maximize global efficiency both for the case of FP.C and FP.D. Indeed, at high pressure, the addition of sweep gas is always counterbalanced by the need of more fuel in the burner.

The membrane SR-based system (FP.C) presents a maximum global efficiency of 34.1%, with a gain of 12% with respect to the conventional case, whereas the maximum global efficiency of the membrane ATR-based system (FP.D) is equal to 33.8%, with a gain of 10% with respect to the conventional case.

When compared to systems fed with pure ethanol, the efficiency obtained by feeding crude-ethanol remains much lower.

	FP.C		FP.D	
	RETENTATE	PERMEATE	RETENTATE	PERMEATE
E (%)	-	-	-	-
H_2 (%)	7.6	100	7.0	100
CH_4 (%)	0.2	-	0.8	-
CO (%)	0.8	-	0.4	-
CO_2 (%)	19.1	-	13.1	-
H_2O (%)	72.3	-	60.9	-
O_2 (%)	-	-	-	-
N_2 (%)	-	-	17.8	-
T (°C)	600	600	541	600
P (atm)	13	1	14	1

Table 4.12 Input and Output data for FP.C and FP.D. Fuel: Crude-ethanol

4.3 Final considerations

The results on ethanol processor – PEMFC systems indicate that the introduction of the membrane in the SR-based system increases global system efficiency by 5% with respect to the conventional case, reaching an efficiency value of 50.4%. This optimal condition is achieved at high pressure and with basically no sweep gas.

The introduction of the membrane in ATR-based system leads to a maximum global efficiency of 50.6%, with a gain of 33% with respect to the conventional

case, allowing to reach values typical of the SR-based systems. To obtain such a global efficiency improvement, pressure must be increases and sweep gas is absolutely required. Indeed, without the addition of sweep gas, the introduction of the membrane in the ATR reactor is not energetically convenient even when compared to traditional ATR-based systems.

The results on the conventional crude-ethanol processor – PEMFC systems show lower values of global efficiency with respect to what achieved when pure ethanol is employed, and the values of global efficiency are similar for the steam reforming and autothermal reforming processes. This is due to the large water amount present in the crude-ethanol, whose vaporization requires more fuel to be sent to the burner.

The introduction of the membrane increases the global efficiency of both systems, and the best values are obtained at high pressure values and with no addition of sweep gas. However, when crude-ethanol is employed, the efficiency value is always much lower that what obtained when pure ethanol is used.

Mathematical Model: Method

The system analysis performed with AspenPlus was a thermodynamic analysis of the whole system that does not allow the size of the plant. In order to have an idea of reaction volumes, a detailed mathematical model of reactors must be performed.

Since the work with AspenPlus has shown the great advantages in terms of efficiency that can be achieved when a high selective hydrogen membrane is introduced in the system, it has been chosen to analyze the effect of operating parameters on the size of the CO clean-up section by developing a mathematical model with the software Mathematica.

In particular, the comparison was performed between a conventional CO clean-up section (considering a HTS, an LTS and a PrOx reactor) and a membrane reactor, placed downstream an Autothermal Reforming reactor. It is worth noting that the comparison takes into account only reactors volumes and does not consider the encumbrance of the heat exchangers, since this was beyond the scope of this work.

In this chapter, the main assumption made to develop the mathematical model and the validation of the model both for the conventional reactor and for the membrane reactor is reported.

The model that will be developed is general, since it will be heterogeneous and with axial dispersion, therefore the specification of the application of the model will happen on the basis of the choice of the reaction, that needs to specify the list of components and the reaction kinetic. The first study will refer to the model of a Water Gas Shift reactor. Further studies will be addressed to the sizing of the high

temperature zone of the fuel processor, that is the Reforming reactors, both for the conventional system and for the innovative one.

5.1 Development of the model

A packed bed catalytic reactor is an assembly of usually uniformly sized catalytic particles, which are randomly arranged and firmly held in position within a vessel or tube. The bulk fluid flows through the voids of the bed. The reactants are transported firstly from the bulk of the fluid to the catalyst surface, then through catalyst pores, where the reactants adsorb on the surface of the pores and then undergo chemical transformation. The formed products desorb and are transported back into fluid bulk. Convection of the bulk fluid is tied in with heat and mass dispersion. Dispersion effects are largely caused by the complex flow patterns in the reactor induced by the presence of the packing. Also, the dispersion effects caused by transport phenomena like molecular diffusion, thermal conduction in fluid and solid phases and radiation. In most cases chemical reactions are accompanied with heat generation or consumption. In case of pronounced heat effects the heat is removed or supplied through the tube wall.

Due to the complex physical-chemical phenomena taking place in packed bed reactors, their exact description is either impossible or leads to very complex mathematical problems. The more detailed the mathematical model, the more parameters it will contain. However, many elementary processes taking place in the reactor can hardly be individually and independently investigated, only effective parameters can be measured. Thus, the more detailed models suffer from a lack of accurate parameter estimations. Therefore, for the description of most chemical reactors, we have to rely on simplified models capturing the most crucial and salient features of the problem at hand. This, also means that there is no universal model. The best model is selected on the basis of the properties of the particular system under consideration, the features of the system one is interested in, the availability of the parameters included in the model and the prospects of successful numerical treatment of the model equations. There are several classes of models used for the description of the packed-bed reactors. The most commonly used class of packed bed reactor models is continuum models. In this

type of models the heterogeneous system is treated as a one – or multi-phase continuum. The continuum approach results in a set of differential-algebraic equations for the bulk fluid and solid phase variables [126-131].

To simulate a packed bed reactor, appropriate reaction rate expressions are required and the transport phenomena occurring in the catalyst pellet, bulk fluid and their interfaces need to be modeled. These phenomena can be classified into the following categories:

- ✓ Intraparticle diffusion of heat and mass
- ✓ Heat and mass exchange between catalyst pellet and bulk fluid
- ✓ Convection of the fluid
- ✓ Heat and mass dispersion in the fluid phase
- ✓ Thermal conduction in the solid phase
- ✓ Heat exchange with the confining walls

The degree of sophistication of the model is determined by the accepted assumptions and, consequently, by the way how aforementioned phenomena are incorporated in the model. According to the classification given by Froment and Bischoff [131], which is widely accepted in the chemical engineering society, the continuum models can be divided in two categories: pseudo-homogeneous and heterogeneous models.

In pseudo-homogeneous models it is assumed that the catalyst surface is totally exposed to the bulk fluid conditions, i.e. that there are no fluid-to-particle heat and mass transfer resistances (solid temperature and concentration at gas-solid interface is equal to temperature and concentration in the bulk of the gas phase). On the other side, heterogeneous models take conservation equations for both phases into account separately.

5.2 Water Gas Shift Reactor Model

The mathematical model utilized for the simulation of the water gas shift reactor is one-dimensional, dynamic, and heterogeneous with an axial dispersion term, both for heat and mass transfer.

Mathematical models of Water Gas Shift reactor or, more in general, of fixed bed reactors are widely reported in literature [64,89,106-111], and they have been taken into account in order to develop a valid and functional model.
The mathematical model will be described and reported for the conventional fixed bed reactor, that is the reactor that describes the HTS and LTS reactors. The membrane reactor model will consider the terms related to hydrogen flux through the membrane (both in the mass and energy balance) and will consider the balances in the permeate side of the membrane. Therefore the membrane model will be described later on in the chapter, indicating the differences with the conventional reactor model.

The model of the conventional fixed bed reactor foresees the following equations:

- ✓ One continuity equation
- ✓ Four species balances in the gaseous phase
- ✓ Four species balances in the solid phase
- ✓ One temperature balance in the gaseous phase
- ✓ One temperature balance in the solid phase

The balances are written in the infinitesimal volume dV along the reactor axis z, therefore the infinitesimal volume dV can be expressed as A·dz, where A is reactor cross section (Figure 5.1).

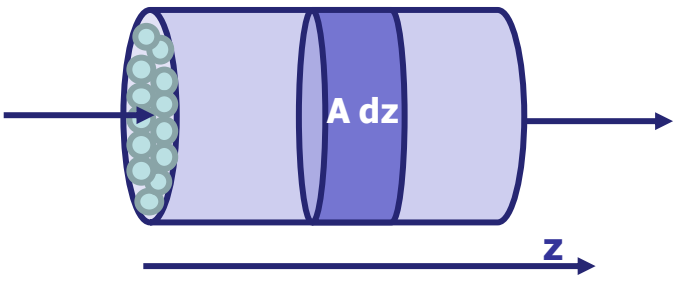

Figure 5.1 Reactor Cross Section

The main assumptions, described in detail later on in the chapter, are that the system is isobaric (verified by means of the Ergun equation), that the gas has an ideal gas behavior, a plug flow regime is developed in the reactor and there are no competitive reactions (experimentally verified).

During water gas shift reaction, the methane can be considered as an inert, since the methanation reactions are suppressed on catalytic systems employed for CO conversion; therefore, the following species are considered: H_2O, CO, CO_2, H_2 and N_2. A mass balance for each chemical species will be written; due to the possibility that the model is heterogeneous, the balance equations will be formulated both for solid and gaseous phase.

The balances in the gaseous phase are the following:

$$0 = \frac{\partial (v \cdot \rho_g)}{\partial z}$$

$$\rho_g \cdot \frac{\partial y_j}{\partial t} = - v \cdot \rho_g \cdot \frac{\partial y_j}{\partial z} + D_{j,eff} \cdot \rho_g \cdot \frac{\partial^2 y_j}{\partial z^2} - k_{g,j} \cdot \frac{a_v}{\varepsilon} \cdot (y_g \cdot y_j - y_S \cdot y_{j,S})$$

$$\rho_g \cdot \frac{\partial T_g}{\partial t} = - v \cdot \rho_g \cdot \frac{\partial T_g}{\partial z} + \frac{k_{e,f}}{C_p} \cdot \frac{\partial^2 T_g}{\partial z^2} - \frac{h_g \cdot a_v}{\varepsilon \cdot C_p} \cdot (T_g - T_S)$$

where j indicated the progressive number of the chemical species and ρ_g is the gas weight density (gr/m^3).
The mass species balances are expressed as a function of the species weight fraction y_j, whereas the energy balance is a function of the gas temperature T_g [K].
The velocity v inside the reactor is evaluated by considering the effective flow section, that is $\varepsilon \cdot A$, where ε is the void fraction of the catalyst bed, evaluated as:

$$\varepsilon = 0.38 + 0.073 \left[1 - \frac{(d_i/d_P - 2)^2}{(d_i/d_P)^2} \right]$$

with d_i reactor diameter and d_P catalyst particle diameter.

a_V represents the interphase exchange surface per volume unit, expressed as it follows:

$$a_v = \frac{6(1-\varepsilon)}{d_p}$$

It is important to note that the continuity equation was written by making hypothesis of pseudo steady-state, that is considering that density and velocity adjust their values according to changes in temperature and weight fractions. In fixed bed reactor, the continuity equation says that the term $\rho_g v$ is constant along the reactor, since no change in the mass of the gas is present; we will see that this condition does not hold in the membrane reactor, as a flux of hydrogen that permeates the membrane at each section is present.

Apart from the continuity equation, the species mass balances and the temperature balance present an accumulation term on the left, whereas on the right there are the convective term, the axial dispersive term, which accounts for flux perturbation effect induced by the presence of catalytic bed, and the term related to the interphase mass transfer.

The symbol S indicates that the weight fractions, the temperature and the gas density are evaluated at the interface with the solid phase.

The parameters present in the equations (effective diffusivity, effective thermal conductivity, mass and heat transfer coefficients from gas to solid phase) will be described in the following paragraphs.

The equations for the solid phase are the following:

$$\rho_S \cdot \frac{\partial \varepsilon_{j,S}}{\partial} = \frac{k_{g,j} \cdot a_v}{(1-\varepsilon)} \cdot (\rho_g \cdot y_j - \varepsilon_S \cdot y_{j,S}) + \rho_{CAT} \cdot \eta \cdot r$$

$$(\rho_S \cdot C_{p,S} + \varepsilon_{CAT} \cdot C_{p,CAT}) \cdot \frac{\partial T_S}{\partial} = \lambda_{e,s} \frac{\partial T_S}{\partial \varepsilon^2} + \frac{h_g \cdot a_v}{(1-\varepsilon)} \cdot (T_g - T_S) + \\ - \varepsilon_{CAT} \cdot \eta_{Th} \cdot r \cdot \Delta H_R$$

The balances present an accumulation term on the left, whereas on the right there are the interphase mass transfer and the generation term. The generation term contains the kinetic of the reaction, r, expressed as mole of CO that reacts per unit of time and of catalyst mass. A catalyst effectiveness factor η_{Th}, evaluated by means of the Thiele modulus, is also introduced in the model in order to take into account intraparticle diffusion. The detail on the kinetic term and on effectiveness factor is reported in the following paragraphs.

The balances are written considering fluid properties constant along the reactor, since the water gas shift reactors does not present a high temperature variation, because the reaction of CO shift is weakly exothermic.

Boundary conditions

The proposed mathematical model is a system of 11 equations: 6 are partial differential equations (PDE) (4 fluid phase mass balances for the four chemical species and 2 for the energy balance of solid and gaseous phases) and 4 ordinary differential equations (ODE) (4 mass balances for the four chemical species in solid phase); the problem is resolved only when the relative initial and boundary conditions are established. The boundary conditions are:

z=0

$$\rho_g \cdot v = \rho_{g,feed} \cdot v_{feed}$$

$$k_{g,j}\left(y_j - y_{j,feed}\right) = D_{e,j}\frac{\partial y_j}{\partial z}$$

$$h_g\left(T_g - T_{g,feed}\right) = k_{e,f}\frac{\partial T_g}{\partial z}$$

z=L

$$\frac{\partial y_j}{\partial z} = 0$$

$$\frac{\partial T_g}{\partial z} = 0$$

Regarding interface section between inert material and catalytic bed it is imposed the continuity of the mass and enthalpy flows, for the compositions, and for the temperatures.

5.3 Analysis of the hypotheses of the model and identification of parameters

In this section, a detailed analysis of the main assumptions made for the development of the mathematical model is reported, which is the outcome of an off-line analysis related to:

- *State of gases*
- *Thermodynamic properties*
- *Analysis of the pressure drop*
- *Kinetic*
- *Effectiveness factor*
- *Axial dispersion*
- *Heterogeneity*

5.3.1 State of gases

The operative conditions of pressure and temperature at which the reactor is analyzed are:

- Pressure relatively low (1-15 atm):

- Temperatures higher than 400K along the length of reactor.

In these conditions, both gas and steam are considered in ideal state, so gas density can be written as follows:

$$\rho_g = \frac{PM \cdot P}{R_g \cdot T_g}$$

$$PM = \sum_j PM_j \cdot y_j^m$$

with P being pressure of the system [atm], R_g the gas constant (0.0821 atm·lt/mol·K), PM_j the molecular weight of specie j and y_j^m the molar fraction of component j.

5.3.2 Thermodynamic properties

Molecular Diffusivity

As regards thermodynamic parameters, data were taken from Perry et al [132] and Poling et al [133]. The diffusion of component i in component j was defined by the following law:

$$D_{i,j} = \frac{A_{i,j} \cdot \Gamma + \ldots_{i,j}}{P} \qquad \left[m^2/s\right]$$

The parameters $A_{i,j}$ and $B_{i,j}$ for each couple of components are reported Table 5.1. The diffusivity of component i in the mixture is defined as:

$$D_{i,m} = \frac{1 - y_i^m}{\sum_{j \neq i} y_j^m / D_{j,i}}$$

		CO	H_2O	CO_2	H_2	N_2
CO	$A_{CO,j}$	-	$0.187 \cdot 10^{-5}$	$3.15 \cdot 10^{-5}$	$15.39 \cdot 10^{-3}$	0
	$B_{CO,j}$	-	2.072	1.57	1.584	0.322
H_2O	$A_{CO,j}$	$0.187 \cdot 10^{-5}$	-	$9.24 \cdot 10^{-5}$	0	$0.187 \cdot 10^{-5}$
	$B_{H2O,j}$	2.072	-	1.5	1.02	2.072
CO_2	$A_{H2O,j}$	$3.15 \cdot 10^{-5}$	$9.24 \cdot 10^{-5}$	-	$3.14 \cdot 10^{-5}$	$3.15 \cdot 10^{-5}$
	$B_{H2O,j}$	1.57	1.5	-	1.75	1.57
H_2	$A_{H2,j}$	$15.39 \cdot 10^{-3}$	0	$3.14 \cdot 10^{-5}$	-	$6.007 \cdot 10^{-3}$
	$B_{H2,j}$	1.584	1.02	1.75	-	-0.9311

Table 5.1 Values of parameters for evaluating molecular diffusivity

Viscosity

The viscosity of each component was evaluated as:

$$\mu_j = \frac{a_j \cdot \Gamma^{b_j}}{1 + \_j/T + \_j/T^2} \qquad \left[Pa \cdot s \right]$$

The parameters a_j, b_j, c_j and d_j for each component are reported in Table 5.2.

The viscosity of the mixture was evaluated as:

$$\mu = \sum_j \frac{\_ \cdot \mu_j}{\_en_j}$$

$$den_j = \_i^m + \sum_{i \neq \_} \_ \cdot \sqrt{\frac{PM_i}{PM_j}}$$

	CO	**H_2O**	**CO_2**	**H_2**	**N_2**
A	$1.113 \cdot 10^{-6}$	$1.71 \cdot 10^{-8}$	$2.148 \cdot 10^{-6}$	$1.797 \cdot 10^{-7}$	$6.559 \cdot 10^{-7}$
B	0.5338	1.1146	0.46	0.685	0.6081
C	94.7	0	290	-0.59	54.714
D	0	0	0	140	0

Table 5.2 Values of parameters for evaluating viscosity

Thermal conductivity

The thermal conductivity of each component was evaluated as:

$$k_j = \frac{e_j \cdot T^{f_j}}{1 + g_j/T + h_j/T^2} \qquad \left[\frac{Kcal}{hr \cdot m \cdot K} \right]$$

The parameters e_j, f_j, g_j and h_j for each component are reported in Table 5.3.
In order to define the thermal conductivity of the mixture, the reduced inverse thermal conductivity of each component Γ_j must be defined:

$$\Gamma_j = \left(\frac{T_{C,j} \cdot PM_j^3}{P_{C,j}^4} \right)^{1/6} \qquad \left[\frac{W}{m \cdot K} \right]$$

	CO	H_2O	CO_2	H_2	N_2
E	$5.149 \cdot 10^{-4}$	$5.334 \cdot 10^{-6}$	3.1728	$2.281 \cdot 10^{-3}$	$2.85 \cdot 10^{-4}$
F	0.6863	1.3973	-0.3838	0.7452	0.7722
G	57.13	0	964	12	16.323
H	501.92	0	$1.86 \cdot 10^{-6}$	0	373.73

Table 5.3 Values of parameters for evaluating thermal conductivity

where $T_{C,j}$ and $P_{C,j}$ indicate the critical temperature (K) and pressure (atm) of species j, respectively.

By introducing the reduced temperature $T_{R,j} = T/T_{C,j}$ of each component and by defining then the following factors for all the couples of species:

$$\varphi_{j,i} = \frac{\Gamma_i}{\Gamma_j} \cdot \frac{e^{0.0464 \cdot T_{R,j} - 0.2412 \cdot T_{R,j}}}{e^{0.0464 \cdot T_{R,i} - 0.2412 \cdot T_{R,i}}}$$

$$A_{j,j} =$$

$$A_{j,i} = \frac{\left(1 + \varphi_{j,i}^{0.5} \cdot \left(PM_j/PM_i\right)^{0.25}\right)^2}{\sqrt{8} \cdot \sqrt{\left(1 + PM_j/PM_i\right)}}$$

it is possible to define the thermal conductivity of the mixture:

$$k_f = \sum_j \frac{m \cdot k_j}{den_j} \qquad \left[\frac{Kcal}{hr \cdot m \cdot K} \right]$$

$$den_j = x_j^m + \sum_i x_i \cdot A_{j,i}$$

In order to obtain the value in W/m·K, the value evaluated by the formula defined above must be multiplied for the factor 1.161.

Specific Heat

The heat capacity of each component was evaluated as:

$$C_{P,j} = \frac{s_j \cdot T^{t_j}}{1 + u_j / T + v_j / T^2} \qquad \left[\frac{cal}{mol \cdot K} \right]$$

The parameters s_j, t_j, u_j and v_j for each component are reported in Table 5.4.

	CO	**H_2O**	**CO_2**	**H_2**	**N_2**
S	6.6	8.22	10.34	6.62	6.5
T	$1.2 \cdot 10^{-3}$	$0.15 \cdot 10^{-3}$	$2.74 \cdot 10^{-3}$	$0.81 \cdot 10^{-3}$	$1.0 \cdot 10^{-3}$
U	0	$1.34 \cdot 10^{-6}$	0	0	0
V	0	0	$-1.995 \cdot 10^{-5}$	0	0

Table 5.4 Values of parameters for evaluating specific heat

The heat capacity of the mixture, was defined as:

$$C_P = \sum_j \frac{y_j \cdot C_{P,j}}{PM_j}$$

Heat of reaction

The heat of reaction at temperature T, $\Delta H_R(T)$, was evaluated according to the following formula:

$$\Delta H_R(T) = \left(C_{P,CO} + C_{P,H2O} \right) \cdot (298 - T) + \Delta H_R^0(298K) + \left(C_{P,CO2} + C_{P,H2} \right) \cdot (T - 298)$$

where the heat of reaction at standard conditions, $\Delta H_R^0(298K)$, is evaluated as the difference of the heat of formations at 298K of products and reactants, reported in Table 5.5.

Water is considered to be formed at gaseous state.

	ΔH_f [cal/mol]
CO	-26416
H_2O	-57797.9
CO_2	-94052
H_2	-

Table 5.5 Heat of formations of reacting species [132]

5.3.3 Analysis of the pressure drop

As regards the analysis of pressure drop in fixed bed reactor, the equation that describes the pressure change along a fixed bed reactor was reported by Froment and Bischoff [131]:

$$-\frac{\partial P}{\partial z} = \frac{2 \cdot f \cdot \rho_g \cdot u_s^2}{g \cdot d_P}$$

Where f is the friction factor for flow in packed beds, u_S is the gas superficial velocity, expressed as $\varepsilon \cdot v$, and g is the acceleration of gravity (9.81 m/s^2).
A well-known equation for the friction factor for flow in packed beds is the Ergun's equation [134]:

$$f = \frac{(1-\varepsilon)}{\varepsilon^3} \cdot \left[1.75 + 150 \cdot \frac{1-\varepsilon}{Re'_p} \right]$$

where Re'_P is Reynolds number evaluated considering catalyst diameter as characteristic length and the superficial gas velocity as characteristic velocity:

$$Re'_p = \frac{\rho_g \cdot u_S \cdot d_P}{\mu}$$

The Ergun's equation for fixed bed reactors was revised from Hicks [135], concluding that it is applicable until the following condition is satisfied:

$$\frac{Re'_p}{1-} \leq 5000$$

For $1000<Re'_P/(1-\varepsilon)<5000$, the Handley and Hegg's [136] equation must be employed:

$$f = \frac{(1-\varepsilon)}{\varepsilon^3} \cdot \left[1.24 + 368 \cdot \frac{1-\varepsilon}{Re'_p}\right]$$

A conservative estimation of pressure drop induced from catalytic bed can be done assuming a temperature of 623K, a GHSV of 1.0 s^{-1}, a reactor diameter of 1 cm, a void fraction of 0.38 (pellet diameter of about 1 mm) and a reactor length of 10 cm; under these circumstances, a value of $Re_p/(1-\varepsilon)$ around 13 is obtained, so the Ergun's equation is applicable; the value of f is about 148, obtaining a pressure loss of about 0.005 bar/m, that is negligible along the narrow length of catalytic bed. This assumption is very common in literature and involves the absence of the equation for conservation of momentum inside the mathematical model.

5.3.4 Reaction kinetic

The kinetic law for the CO shift reaction is a Langmuir-Hinshelwood law [39,106]:

$$r = \frac{k \cdot K_{CO} \cdot K_{H2O} \cdot \left(P_{CO} \cdot P_{H2O} - \frac{P_{CO2} \cdot P_{H2}}{K_{EQ}}\right)}{(1 + \zeta_{CO} \cdot P_{CO} + \zeta_{H2O} \cdot P_{H2O} + \zeta_{CO2} \cdot P_{CO2})^2}$$

where P_j are the partial pressure of reacting components and K_{EQ} is the equilibrium constant, given by:

$$K_{EQ} = e^{\frac{4577.8}{T_g} - 4.33}$$

the kinetic constant k and the adsorption/desorption coefficient K_j are expressed in s^{-1} and in atm^{-1}, respectively, and are defined as it follows:

$$k = \mathrm{Exp}\left\{\left(-\frac{29364}{1.987 \cdot T_g} + \frac{40.32}{1.987}\right)\right\}$$

$$K_{CO} = \mathrm{Exp}\left\{\left(\frac{3064}{1.987 \cdot T_g} - \frac{6.74}{1.987}\right)\right\}$$

$$K_{H2O} = \mathrm{Exp}\left\{\left(-\frac{6216}{1.987 \cdot T_g} + \frac{12.77}{1.987}\right)\right\}$$

$$K_{CO2} = \mathrm{Exp}\left\{\left(\frac{12542}{1.987 \cdot T_g} - \frac{18.45}{1.987}\right)\right\}$$

5.3.5 Effectiveness factor

The majority of catalysts available on the marked have a porous structure, where most of the catalytically active surface resides on the interior surface which can only be accessed via the pores. In a porous catalyst the reaction takes place simultaneously with heat and mass transport and both processes must usually be considered together.

Incorporation of intraparticle resistances into an overall reactor model adds an additional – the intraparticle – dimension into the problem. Generally, due to the non-linearity of the reaction rates and the coupling between several mass and energy conservation equations, the single particle problem can only be solved numerically. This considerably complicates the handling of the differential equations.

To avoid this complication, the idea of the effectiveness factor η_{Th} was introduced independently by Thiele [137] and Zeldowitsch [138]. The effectiveness factor is defined as the ratio of the reaction rate taking transport limitations into account to the reaction rate without transport limitations (i.e. at particle surface conditions).

Expression of the effectiveness factor as a function of reaction and diffusivity parameters are widely discussed in literature [139-141].
The expression employed in this work is reported in [139] and it is the following one:

$$\eta_{Th} = \frac{1}{Th} \cdot \left[\frac{1}{\tanh(3 \cdot Th)} - \frac{1}{3 \cdot Th} \right]$$

The efficiency depends on the Thiele modulus Th, defined as it follows:

$$Th = l_{PORE} \cdot \sqrt{\frac{k''}{D_{CO,ep}}}$$

A reasonable value of pore dimension, d_{PORE}, is around 200 nm.
In the expression, d_{PORE} is expressed in m. k" is the kinetic constant expressed in 1/s. $D_{CO,ep}$ is the effective CO diffusivity in the pores, expresses as:

$$D_{CO,ep} = \left(\frac{1}{D_{k,CO}} + \frac{1}{D_{m,CO}} \right)^{-} \cdot \frac{\varepsilon_P}{\tau_P}$$

where $D_{m,CO}$ is CO molecular diffusivity (defined above in the paragraph) whereas $D_{k,CO}$ is Knudsen diffusivity [m^2/s], defined as it follows:

$$D_{k,CO} = 4.534 \cdot d_{PORE} \cdot \sqrt{\frac{1000 \cdot T_g}{PM_{CO}}}$$

Reasonable values of catalyst parameters, pore fraction ε_P and tortuosity τ_P, are 0.5 and 5, respectively.

It is worth noting that in most practical applications catalyst particles are usually principally isothermal and only external heat transport limitations play a role, whereas resistance to mass transfer inside the particle usually dominates over the interfacial mass transfer resistance.

5.3.6 Axial Mass and Heat Dispersion in the gas phase

Turbulence mixing due to the pellets packing may be incorporated in the model by considering effective axial dispersive coefficients in the gas phase, which include also diffusion and conduction transport phenomena, for the mass and heat balance equations respectively.

A rough estimation of the mixing effects can be done trough the calculation of the ratio L/d_P. If this ratio is higher than 50 [142], then mixing transport phenomena can be neglected. In our case, the pellet diameter is 1 mm and the bed length 10-15 cm, thus leading to L/dp equal to 10, which does allow us to neglect mixing effects.
A more precise evaluation of the mixing relevance on the mass transport phenomena can be done trough the calculation of the mass Peclet number, given by the ratio between the rate of transport by convection and the rate of transport by mass dispersion:

$$Pe = \frac{v \cdot L}{D_m}$$

Considering that the diffusion is more relevant at lower velocities, a flow rate equal to 1 Nm^3/h gives a value of v of around 0.1 m/s (also considering the presence of the catalyst with a bed porosity of 0.4). With a diffusion coefficient D_m of 10^{-4} m^2/s, the mass Peclet number is around 200. By a comparison with data reported in the literature [139,143], at these values of the Peclet number (<500), mass dispersion transport phenomena cannot be neglected. Therefore, the axial dispersion term was introduced both in the mass species balance and in the energy balance.

For the calculation of mass axial dispersion coefficient, the following expression reported in literature [144] are used:

$$D_{e,j} = \gamma \cdot d_P \cdot \left[\frac{0.73 \cdot \varepsilon}{v \cdot d_P / D_{m,j}} + \frac{0.5}{1 + \frac{9.7 \cdot \varepsilon}{v \cdot d_P / D_{m,j}}} \right] \quad m^2/s$$

valid for:

$0.008 \leq Re_P \leq 50$

$0.377 \leq d_P \leq 5$ mm

As regards the axial heat dispersion coefficient, for the gas phase the thermal phenomena that have to be considered are the conductive and radiant dispersion and backmixing, whereas for the solid phase in fixed bed reactors the radiant and conductive thermal phenomena have to be considered.

Obviously, the experimental evaluation of these phenomena is rather difficult; at this purpose, there are many theoretical and experimental works for evaluation of axial thermal dispersion in fixed bed [145-157].

In particular, the first values of axial thermal conductivity in fixed bed were obtained by Yagi et at. [145-148] by means of experimental measures of axial temperature along a fixed bed heated by an infrared lamp and crossed from a known counter-current air stream; the interpolation of these measures with a conductive-convective mathematical model lead to the determination of the parameter of interest.

The experiments, carried out on different materials and dimensions of the catalytic bed, lead to determination of following expression:

$$\frac{k_{e,f}}{k_f} = \frac{k_e^0}{k_f} + 0.5 \cdot Re_P \cdot Pr$$

This expression is then verified from ulterior experimental analysis of the other authors, also with different materials and shapes of the constitutes of the bed, determining its validity for a Reynolds number higher than 0.8.

The first term of this expression, also shown in previous works [145,146,150], represents the effective axial thermal conductivity for bed in a stagnant flow, including also conductive phenomena that interest substantially the solid phase; commonly, Krupiczka's expression is utilized [151,152] according to which:

$$\frac{k_e^0}{k_f} = \left(\frac{k_S}{k_f}\right)^{\alpha}$$

with

$$\alpha = 0.28 - 0.757 \cdot \ln(\varepsilon) - 0.057 \cdot \ln\left(\frac{k_S}{k_f}\right)$$

where k_S is the catalyst thermal conductivity; the effect of this parameter was considered in the analysis of the performance of the reactors; a reasonable value of commercial metal based catalyst is 0.3 W/(m·s·K) [101,102].

The experiments are carried out at low temperatures and in absence of high temperature gradients so, it is evident that in the above expression conductive and convective phenomena are considered, but not the radiation ones.

Instead, when the bed is submitted to high thermal levels and gradients, as in autothermal processes for the hydrogen production, it is necessary to consider also the radiant effects.

With this purpose, Wakao and Kato [153] proposed the following expression:

$$k_e^0 = k_{e,CONDUCTIVE}^0 + k_{e,RADIATIVE}^0$$

Where the conductive term is the one reported above by Krupiczka's expression, whereas the radiative term was evaluated according to:

$$\frac{k_{e,RADIATIVE}^0}{k_f} = 0.707 \cdot Nu_r^{0.96} \cdot \left(\frac{k_S}{k_f}\right)^{0.11}$$

valid for

$$20 \le \frac{\kappa_S}{k_f} \le 000$$

$$Nu_r \le 1.3$$

and where

$$Nu_r = \frac{h_r \cdot d_P}{k_S}$$

with

$$h_r = \frac{0.2268}{2/e - 1.264} \cdot \left(\frac{T}{00}\right)$$

where e is solid emissimivity (reasonable value of 0.8).
For the presence of water and carbon dioxide, also for the gas phase would be considered the radiant phenomenon; with this purpose Wakao [157] proposed also a modified expression of hr for gas phase. But it has to be considered that the emissivity of gaseous compounds is strongly dependent from temperature, void dimension and partial pressure, that in fixed bed generally have very low value and so, in this work, it is neglected.
For example, the emissivity of CO_2 at high temperature (about 1200 K) and in a void radius of 1 cm has a value of just 0.05 [158].

The effective axial thermal conductivity and the effective axial diffusivity were also evaluated on the basis of the correlations proposed by Schlunder and Tsotsas [159], in order to compare the results.

$$D_{e,j} = \left(1 - \sqrt{1 - \varepsilon}\right) \cdot D_{m,j} + \frac{\nu \cdot d_P}{2}$$

$$k_{e,f} = k_f \left[\varepsilon \cdot k_e^0 + 5 \cdot \frac{Pe_x}{K_\infty \cdot f(d_i/d_P)}\right]$$

Where K_∞ is the limiting value of the Peclet number in an unconfined bed, which is about 8, and $f(d_i/d_P)$ is a correction factor accounting for the influence of the tube wall and the resulting flow maldistribution:

$$f(d_i/d_P) = 1 - 1.14 \cdot (d_P/d_i)^2$$

The Peclet number is defined as:

$$Pe_x = \frac{v \cdot \rho_g \cdot C_p}{k_f} \cdot X_F$$

with X_F effective mixing length $F \cdot d_P$ ($F = 1.25$ for spherical particles).

The thermal conductivity of the packed bed at zero flow k_e^0 is calculated by formulas summarized by Zehner and Schlunder [160]:

$$\frac{k_e^0}{k_f} = (1 - \sqrt{1-\varepsilon}) \left(1 + \frac{k_{rad}}{k_f}\right) + \sqrt{1-\varepsilon} \left\{ \frac{2}{1 + \frac{k_f}{k_S} B} \cdot \left[\frac{\left(1 - \frac{k_f}{k_S}\right) B}{\left(1 - \frac{k_f}{k_S} B\right)^2} \cdot \ln\left(\frac{k_S}{k_f B}\right) - \frac{B+1}{2} - \frac{B-1}{1 - \frac{k_f}{k_S} B} \right] + \frac{1}{\frac{k_f}{k_{rad}} + \frac{k_f}{k_S}} \right\}$$

with

$$k_{rad} = \frac{0.23}{\frac{2}{e}} \cdot \left(\frac{T}{100}\right)^3 \cdot d_P$$

and

$$B = C \cdot \left(\frac{1-\varepsilon}{\varepsilon}\right)^{10/9}$$

C = 1.25 (pellets) or 1.4 (broken particles).

The comparison of the axial effective diffusivity of CO evaluated with Edwards and Richardson formula (red circles) and with Schlunder and Tsotsas formula (blue circles) is reported in Figure 5.2. The parameters were evaluated at 350 °C, considering the catalyst properties of a typical commercial WGS catalyst (catalyst density of 2.4 gr/cm^3 and catalyst thermal conductivity of 0.3 W/m·K). The pellets diameter was fixed at 1 mm, whereas reactor diameter was taken as 1 cm and reactor length as 10 cm. In the range of GHSV investigate (0.1 – 2 s^{-1}) the Reynolds number referred to the particle diameter Re_P varied from 1 to 22.

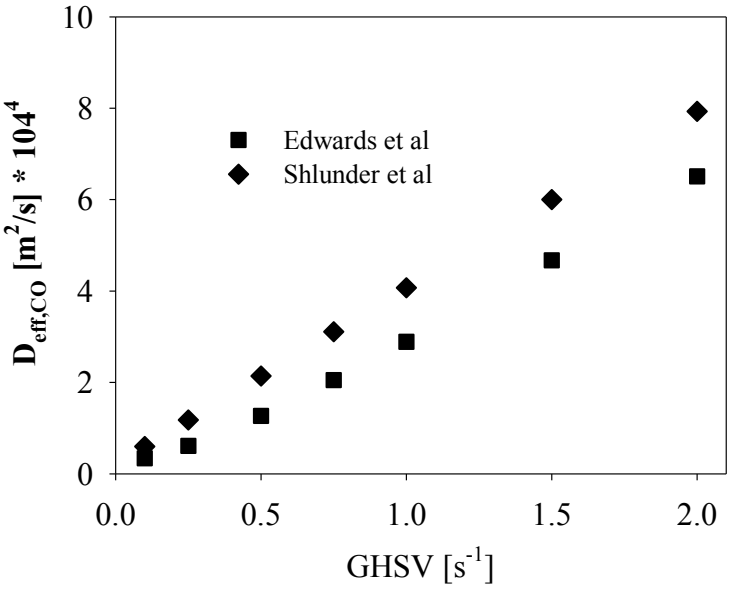

Figure 5.2 CO axial dispersion coefficient $D_{eff,CO}$ as a function of GHSV at T = 350 °C. d_P = 1 mm, d_i = 1 cm

It is possible to observe that there is a good agreement between the two correlations, and in the present work the correlation of Edwards and Richardson was used, since it is reported to be valid for one dimensional models, whereas the Schlunder and Totsas one was employed for two dimensional models and the correlation was found as an adaptation of the radial dispersion coefficient.

As regards the axial heat dispersion coefficient, the comparison of the results obtained with the first correlation described above with the one of Schlunder and Tsotsas is reported in Figure 5.3.

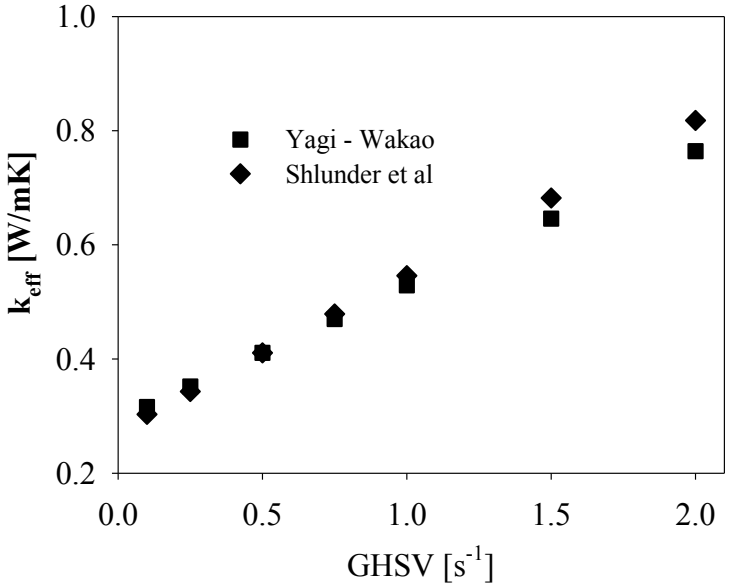

Figure 5.3 Effective axial thermal conductivity k_e as a function of GHSV at T = 350 °C. d_P = 1 mm, d_i = 1 cm

The first correlation is based on the value of radiative conductivity of 0.0215 W/m·K, evaluated by Wakao correlation.

The second correlation is based on the value of radiative conductivity of 0.0371 W/m·K, evaluated by Zehner and Schlunder correlations.

The two values are very similar and they are one order of magnitude lower than the thermal conductivity of the mixture (that is about 0.11 W/ m·K), since the radiative contribution of the solid to the effective thermal conductivity is generally negligible at middle-low temperature, as for the case of the WGS reactor.

As it is possible to observe, the correlations found for this parameter give substantially the same results in all the range of GHSV investigated.

In the present work, the correlations of Yagi and Wakao were employed.

5.3.7 Heterogeneity

The model written above is heterogeneous, that is, it considers that there is a drop of concentration of reactants from the bulk of the gaseous phase to the interface with the solid particle due to mass transport.

A criterion for determining the onset of interphase heat transfer limitation was derived by Mears [161] for the Arrhenius type of reaction rate dependency on the

temperature and under the assumption of negligible direct thermal conduction between spherical particles and negligible interphase mass transfer resistance. The criterion states that the actual reaction rate deviates less than 5% from the reaction rate calculated assuming identical solid phase and bulk fluid conditions, if the following inequality is satisfied:

$$\frac{\left|\Delta H\right| \cdot \bar{r} \cdot d_P^2}{4 \cdot h_g \cdot T} \leq 0.15 \cdot \frac{R_g \cdot T}{E_a}$$

A similar criterion for the interphase concentration difference was derived by Hudgins [162]; $r(C_j,T_g)$ and $r(C_{j,S},T_g)$ do not differ by more than 5% provided that:

$$\frac{\bar{r} \cdot d_P}{2 \cdot r_j \cdot k_{g,j}} \cdot \left| \frac{\partial_j}{\partial \square_j} \right|_{C=\square_j} \leq 0.15$$

For the calculation of solid-gas mass transfer coefficients, the expressions reported in literature will be employed; the details on the evaluation of the physical and transport properties and on the kinetic of reaction is reported in the following sections.

Table 5.6 reports the value of the parameters employed to apply the Mear's criterion. In these conditions, Mears' criterion is satisfied, so it is possible to describe the process with an homogeneous model.

d_P [mm]	1
d_i [cm]	1
L [cm]	10
h_g [J/(m^{2}sK)]	242
$k_{g,CO}$ [m/s]	0.2
C_{CO} [mol/m^3]	0.4
r [mol/m^{3}s]	[97]
T [K]	623

Table 5.6 Model parameters

Another criterion for the evaluation of the heterogeneity of the model can be found on Levenspield [139]; the determination of the significance of the film mass transfer can be done by evaluating the ratio between the rate of reaction in absence of mass transfer and the rate of reaction if film controls. This ratio must be lower than 0.01 in order to affirm that film resistance does not influence the rate of reaction. The ratio is given by the following equation:

$$\frac{\bar{r} \cdot d_P}{6 \cdot k_g \cdot C_{CO}} \leq 0.01$$

Whit the values of employed to model the reactor, this ratio is of the order of 0.006, thus the results show that also according to this criterion the model can be developed as a pseudo-homogeneous one, although the value is not so far from the limit value of 0.01.

In the case of pseudo-homogeneous model, the balance are the following:

$$0 = \frac{\partial (v \cdot \rho_g)}{\partial z}$$

$$\rho_g \cdot \frac{\partial y_j}{\partial t} = - v \cdot \rho_g \cdot \frac{\partial y_j}{\partial z} + D_{e,j} \cdot \rho_g \cdot \frac{\partial y_j}{\partial z^2} - \frac{(1-\varepsilon)}{\varepsilon} \cdot \rho_{CAT} \cdot \eta_{Th} \cdot r$$

$$\varepsilon \cdot \rho_g \cdot C_p + (1-\varepsilon) \cdot \rho_{CAT} \cdot C_{p,CAT} \frac{\partial T_g}{\partial t} = - v \cdot C_p \cdot \rho_g \cdot \frac{\partial T_g}{\partial z} + \varepsilon \cdot k_{e,f} \cdot \frac{\partial T_g}{\partial z^2} - (1-\varepsilon) \cdot \rho_{CAT} \cdot \eta_{Th} \cdot r \cdot \Delta H$$

The balances on species change their generation term, that is, the transport from gas to solid phase is substituted with the reaction term. As regards the temperature balance, the same consideration must be done on the generation term, that changes from a transport to a reaction term. Moreover, the accumulation term is not

defined as the energy change of the gas phase $d(\varepsilon \cdot \rho_g \cdot C_p \cdot T_g)/dt$, but, since $T_g=T_S$, it takes into account also the temperature of the solid phase:

$d[\varepsilon \cdot \rho_g \cdot C_P + (1-\varepsilon) \cdot \rho_S \cdot C_{P,S}] \cdot T_g/dt$.

The boundary condition are the same of the heterogeneous model.

Solid-gas heat and mass transfer coefficients

In order to develop an heterogeneous model or to verify if the pseudo-homogeneous model can be applied (that is, $T_g=T_S$ and $y_j=y_{j,S}$), the solid-gas transfer coefficients must be defined; the value of the heat transfer coefficient h_g can be found in literature [163-166] from the correlations of the Nusselt number as a function of the Reynolds and Prandlt number. The Nusselt number is defined as:

$$Nu = \frac{h_g \cdot d_P}{k_f}$$

The correlations for Nusselt for heat transfer from the gas phase to the catalyst particle are:

- ✓ Frossling equation [132]

$$Nu = 2 + 0.552 \cdot Re_P^{0.6} \cdot Pr^{0.33}$$

where Pr is the Prandlt number:

$$Pr = \frac{c_P \cdot \mu}{k_f}$$

And Re_P is the Reynolds number evaluated using the particle diameter as characteristic length and the gas velocity v is characteristic velocity:

$$Re_p = \frac{\rho_g \cdot v \cdot d_P}{\mu}$$

✓ Bird et al. [163]

$$Nu = 2.27 \cdot (1-\varepsilon)^{0.51} \cdot Re_P^{0.49} \cdot Pr^{0.33} \qquad Re_P/(1-\varepsilon) < 300$$

$$Nu = 1.27 \cdot (1-\varepsilon)^{0.41} \cdot Re_P^{0.59} \cdot Pr^{0.33} \qquad Re_P/(1-\varepsilon) > 300$$

✓ Wakao et al [166]

$$Nu = 2 + 1.1 \cdot Re_P^{0.6} \cdot Pr^{0.33}$$

For calculating the gas to particle mass transfer coefficient for each component j, the Chilton-Colburn analogy between mass and heat can be used, by replacing Nu with the Sherwood number Sh_j and Pr with the Schmidt number Sc_j. The Sh_j number allows to evaluate the mass transfer coefficient $k_{g,j}$ and is defined as:

$$Sh_j = \frac{k_{g,j} \cdot d_P}{D_{m,j}}$$

whereas Sc_j is the Schimdt number:

$$Sc_j = \frac{\mu_j}{\rho_g \cdot D_{m,j}}$$

The trend of the heat transfer coefficient and of CO mass transfer coefficient as a function of the GHSV for the three correlations are reported in Figure 5.4 and Figure 5.5, respectively. The reactor configuration and operating conditions are reported in Table 5.6.

It is possible to observe that, both for the heat and mass transfer coefficient, the correlations proposed by Wakao and Bird allows to obtain the same trend of the parameter with the GHSV. Frossling equation, instead, gives value near to the one evaluated by Wakao correlation at low GHSV, whereas the value at high GHSV

are near the Bird correlation. However, the highest deviation is of about 30% on the value and this deviation had a negligible impact on reactor performance.

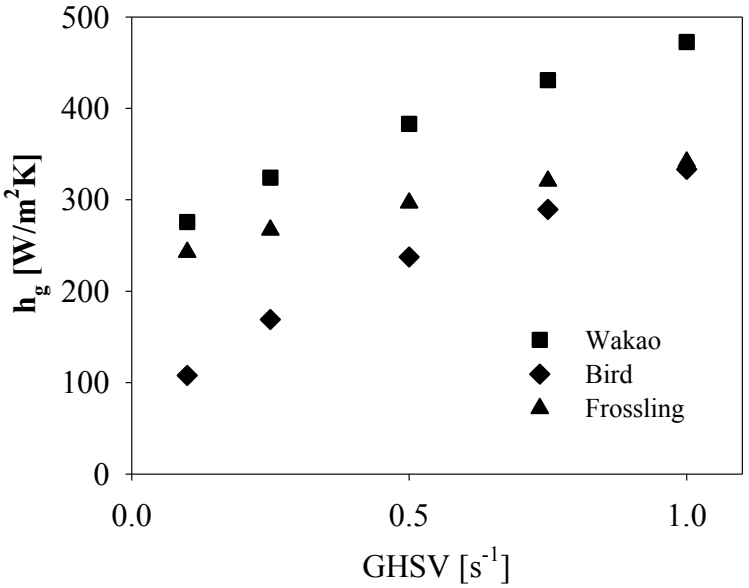

Figure 5.4 Gas to particle heat transfer coefficient as a function of GHSV in a HTS reactor evaluated according to three different correlations

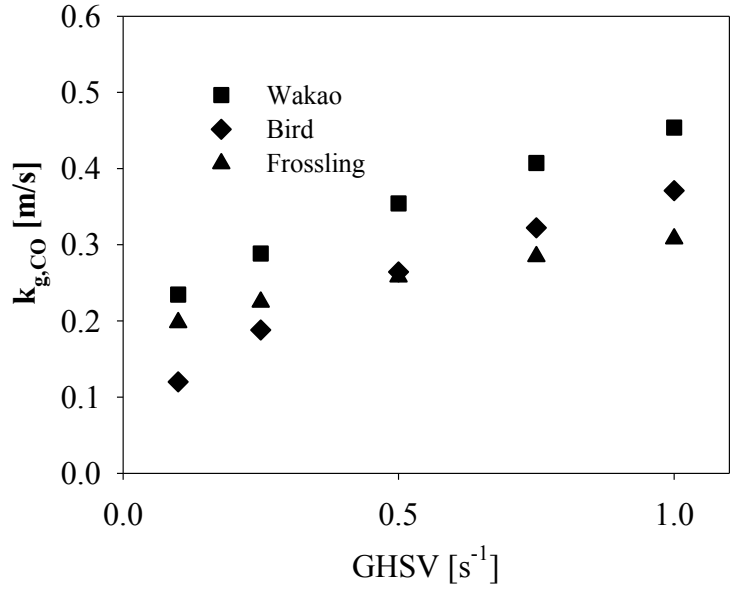

Figure 5.5 Gas to particle CO mass transfer coefficient as a function of GHSV in a HTS reactor evaluated according to three different correlations

The trend of the CO conversion as a function of GHSV is reported in Figure 5.6, evaluated with the three correlations of the coefficients reported above.

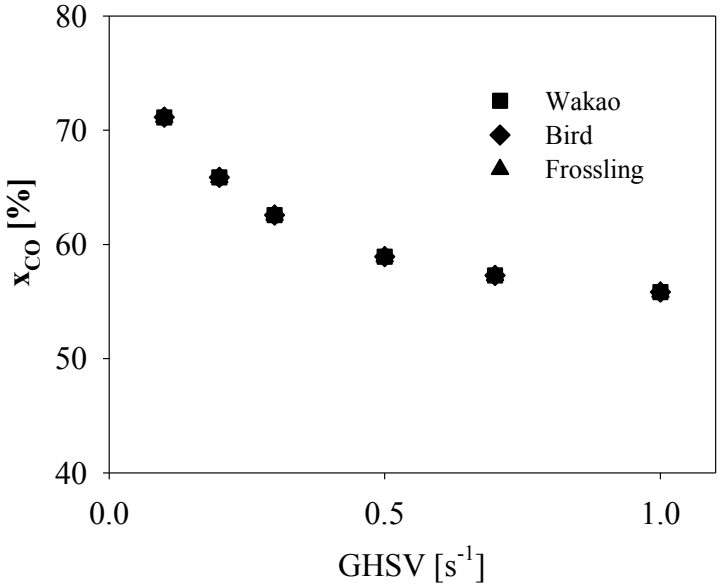

Figure 5.6 CO conversion as a function of GHSV in a HTS reactor evaluated according to three different correlations

It is possible to observe that the values of CO conversion are identical in the three cases; this is due to the fact that the system can be described with a pseudo-homogeneous model, therefore there is not a strong sensitivity in the gas to particle mass and heat transfer coefficient, moreover the values of the coefficients are very similar with the three correlations.

The comparison of the heterogeneous model with the pseudo-homogeneous one is reported in Figure 5.7. The Figure reports the CO conversion as a function of the GHSV for a fixed bed high temperature shift reactor, with reactor details reported in Table 5.6.

It is possible to observe that a slight difference in reactor performance is observed at low GHSV (with a difference in CO conversion of about 4%), whereas a complete accordance is obtained at high GHSV.

In this work we employed the Frossling equation to perform the calculations, since it is reported to be valid for fixed bed reactors at low Re [132, 163].

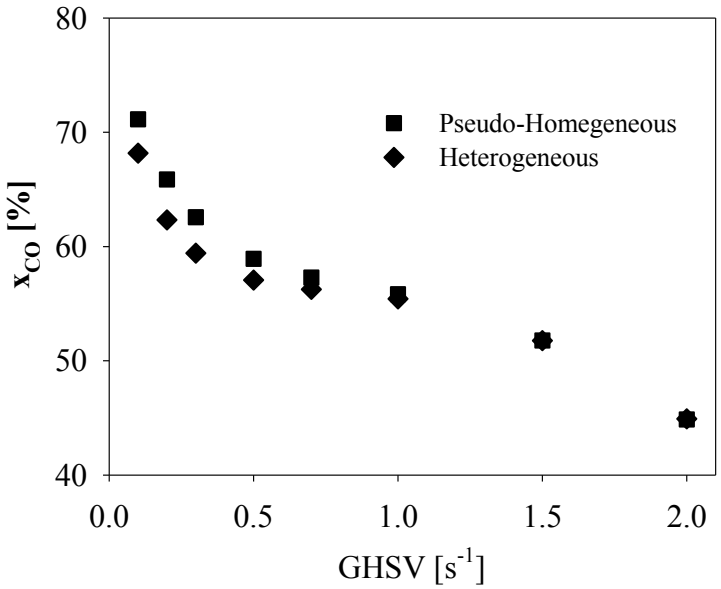

Figure 5.7 CO conversion as a function of GHSV in a HTS reactor with the heterogeneous model (diamonds) and with the pseudo-homogeneous one (squares)

5.4 Membrane reactor model

As regards the membrane reactor, it is constituted by two coaxial tubes, the internal one being the permeate side where hydrogen permeates and the external one being the catalytic bed.

A section of the modeled membrane reactor is reported in Figure 5.8.

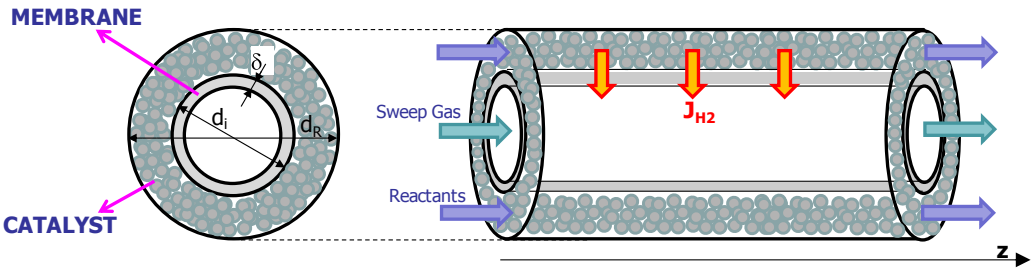

Figure 5.8 Membrane reactor cross-sections

In the mathematical model of a membrane reactor the presence of a hydrogen flux through the membrane must be taken into account. In particular, the continuity equation will present a term of mass variation due to hydrogen permeation, and so will be for the balance on hydrogen.

The energy balance will present two new terms, that is the enthalpy change due to the enthalpy related to hydrogen that permeates and a heat transfer term between the retentate and the permeate side.
Therefore, the balances for the retentate side of the membrane reactor are the following ones:

$$0 = -\frac{\partial(v \cdot \rho_g)}{\partial z} - \frac{PM_{H2} \cdot \pi \cdot (d_i + 2 \cdot \delta)}{\varepsilon \cdot A} \cdot J_{H2}$$

$$\rho_g \cdot \frac{\partial w_j}{\partial t} = -\frac{\partial(v \cdot \rho_g \cdot y_j)}{\partial z} + D_{e,j} \cdot \frac{\partial(\rho_g \cdot y_j)}{\partial z^2} - k_{g,j} \cdot \frac{a_v}{\varepsilon} \cdot (\rho_g \cdot y_j - \rho_{g,S} \cdot y_{j,S}) \qquad \text{for } CO, CO_2, H_2O$$

$$\rho_g \cdot \frac{\partial w_{H2}}{\partial t} = -\frac{\partial(v \cdot \rho_g \cdot y_{H2})}{\partial z} + D_{e,H2} \cdot \frac{\partial(\rho_g \cdot y_{H2})}{\partial z^2} + \\ - k_{g,H2} \cdot \frac{a_v}{\varepsilon} \cdot (\rho_g \cdot y_{H2} - \rho_{g,S} \cdot y_{H2,S}) - \frac{PM_{H2} \cdot \pi \cdot (d_i + 2 \cdot \delta)}{\varepsilon \cdot A} \cdot J_{H2} \qquad \text{for } H_2$$

$$\rho_g \cdot \frac{\partial T_g}{\partial t} = -\frac{\partial(v \cdot \rho_g \cdot T_g)}{\partial z} + \frac{\lambda_{e,f}}{C_P} \cdot \frac{\partial T_g}{\partial z^2} - \frac{h_g \cdot a_v}{\varepsilon \cdot C_P} \cdot (T_g - T_S) + \\ - \frac{PM_{H2} \cdot \pi \cdot (d_i + 2 \cdot \delta)}{\varepsilon \cdot A} \cdot J_{H2} \cdot \frac{C_{P,H2}}{C_P} \cdot (T_g - T_{SG}) - \frac{U_M \cdot \pi \cdot (d_i + 2 \cdot \delta)}{\varepsilon \cdot A \cdot C_P} \cdot (T_g - T_{SG})$$

where d_i is the internal membrane diameter, δ is its thickness, U_M is the heat transfer coefficient through the membrane, taken in this work equal to 2.4 J/m^{2}sK [101,102,109,167], J_{H2} are the moles of hydrogen that permeate per unit of membrane area and time and T_{SG} is the temperature on the permeate side of the membrane.

As described in the following section, J_{H2} depends on temperature and on hydrogen partial pressure on the retentate and on the permeate side of the membrane.

The boundary conditions, the balances in the solid phase and the considerations on the hypotheses of the model, together with model parameters and thermodynamic properties, are the same of what is reported for the conventional WGS reactor.

The expression of the hydrogen flux and also consideration on the kinetic are reported in the following paragraph.

Since the membrane reactor presents a permeate side where hydrogen flows, balances on this side of the membrane are necessary in order to complete the model.

In particular, the permeate side of the membrane requires a mass balance, a balance on hydrogen and an energy balance to be modeled.

The equations are reported as it follows:

$$0 = \pm \frac{\partial (v_{SG} \cdot \rho_{SG})}{\partial z} + \frac{PM_{H2} \cdot \pi \cdot d_i + 2 \cdot \delta}{A_{SG}} \cdot J_{H2}$$

$$\rho_{SG} \cdot \frac{\partial y_{H2,SG}}{\partial t} = \pm \frac{\partial (v_{SG} \cdot \rho_{SG} \cdot y_{H2,SG})}{\partial z} - D_{m,H2} \cdot \frac{\partial (\rho_{SG} \cdot y_{H2,SG})}{\partial z^2} + \frac{PM_{H2} \cdot \pi \cdot d_i + 2 \cdot \delta}{A_{SG}} \cdot J_{H2}$$

$$\rho_{SG} \cdot \frac{\partial T_{SG}}{\partial t} = \pm \frac{\partial (v_{SG} \cdot \rho_{SG} \cdot T_{SG})}{\partial z} + \frac{k_{SG}}{C_{P,SG}} \cdot \frac{\partial T_{SG}}{\partial z^2} + \frac{PM_{H2} \cdot \pi \cdot d_i + 2 \cdot \delta}{A_{SG}} \cdot J_{H2} \cdot \frac{C_{P,H2}}{C_{P,SG}} \cdot (T_g - T_{SG}) + \frac{U_M \cdot \pi \cdot d_i + 2 \cdot \delta}{A_{SG} \cdot C_{P,SG}} \cdot (T_g - T_{SG})$$

where the symbols are the same of what is reported for the conventional fixed bed reactor and for the retentate side of the membrane reactor, but the symbol SG indicates that they are referred to the permeate side of the membrane.

The sign of the convective term depends of the direction of the sweep gas flow with respect to the direction of the reactants flow: if the sweep gas is sent co-currently to the reactive mixture, the convective term is negative, whereas if it is sent counter-currently the convective term is positive.

The boundary conditions for the permeate side of the membrane are:

$$z=0 \quad \begin{cases} \rho_{SG} \cdot v_{SG} = \rho_{SG,feed} \cdot v_{SG,feed} \\ y_{H2,SG} = y_{H2,SG,feed} \\ T_{SG} = T_{SG,feed} \end{cases}$$

$$z=L \quad \begin{cases} \dfrac{\partial y_{H2,SG}}{\partial z} = 0 \\ \dfrac{\partial T_{SG}}{\partial z} = 0 \end{cases}$$

These conditions are valid if the sweep gas is sent co-currently to the reactive mixture; in case of counter-current configuration, the condition at z = 0 and at z = L must be switched.

It is worth noting that the permeate side of the membrane does not present a term of dispersion related to the presence of a fixed bed, therefore only molecular diffusion is present in the hydrogen balance; the molecular diffusion term is generally negligible for Reynolds number lower than one in very short reactors [159]. This situation is avoided in the present model, therefore the equations on the permeate side are generally in the first order derivative with respect to the axial coordinate z.

5.4.1 Reaction kinetic in the membrane reactor

Although the Langmuir-Hinshelwood expression of kinetic is reported in literature for the membrane WGS reactor model, as reported in chapter 1 some authors found that the Temkin [106] expression best fits the equilibrium shift in the membrane reactor due to hydrogen removal:

$$r = \frac{k_C \cdot \rho_g \cdot \left(P_{CO} \cdot P_{H2O} - \right.}{a_k \cdot P_{H2O} +}$$

the kinetic constant k_c and coefficient a_k are defined as it follows:

$$k = \cdot 10^{11} \cdot e^{-\frac{26800}{1.987 \cdot T_g}} \qquad [atm^{-} \cdot s^{-}]$$

$$a_k = .5 \cdot 10^{9} \cdot e^{-\frac{21500}{1.987 \cdot T_g}}$$

Therefore, the simulations of the membrane reactor were performed by employing this kinetic expression. The comparison of the results with the two kinetic expressions is reported below at the end of the chapter.

5.4.2 Hydrogen Flux through the membrane J_{H2}

As reported in the introduction of this thesis, a huge number of studies is present on hydrogen permeation law through a Palladium membrane. In this model, the expression reported by Basile et al [64] was employed, since it was experimentally verified in a WGS reactor. In particular, the hydrogen flux is controlled by two mass transfer resistances; R_f, resistance through the film at the interface between the Pd or Pd/Ag layer and the gas, and R_m, resistance through the Pd or Pd/Ag layer.

The fluxes through the film and the metallic layer are respectively given by:

$$J_f = \frac{P_{H2} - }{R_f}$$

$$J_m = \frac{P_{H2,f} - }{R_m}$$

P_{H2} is the hydrogen partial pressure inside the bulk of the gas phase (retentate side), $P_{H2,SG}$ is the hydrogen partial pressure on the permeate side of the membrane and $P_{H2,f}$ is the hydrogen partial pressure at the membrane interface.

Resistance through the film, R_f, is evaluated as it follows:

$$R_f = \left(k_f \cdot \rho_g / P\right)^{-1} \qquad \left[\frac{m^2 \cdot s \cdot atm}{mol}\right]$$

where k_f is the film coefficient in m/s, evaluated from the Sh number ($Sh = k_f \cdot d_i / D_{m,H2}$) given by [132]:

$$Sh = .615 \cdot \left(\frac{d_i}{L}\right)^{1/3} \cdot \left(Re \cdot Sc_{H2}\right)^{1/3}$$

where Re is the Reynolds number evaluated considering d_i as characteristic length and Sc_{H2} is the hydrogen Schmidt number.

The evaluation of the membrane resistance is done by evaluating hydrogen permeability through the membrane layer; as reported in the introduction, the hydrogen flux through the membrane J_m follows the Sievert's law, therefore R_m is given by:

$$R_m = \left(\frac{Pe}{\delta}\right)^{-1} \qquad \left[\frac{m^2 \cdot s \cdot atm^{0.5}}{mol}\right]$$

where Pe is hydrogen permeability through the membrane; an expression of the permeability for Pd/Ag membrane is reported by Basile et al. [64]:

$$Pe = 3.07 \cdot 10^{-4} \cdot e^{-\frac{3098}{T_g}} \qquad \left[\frac{mol}{m \cdot s \cdot atm^{0.5}}\right]$$

Criscuoli et al [106] reported an expression for the permeability for Pd membrane, experimentally verified on the basis of the experimental data in its work and in the work of Itoh et al [169]:

$$Pe = 2.95 \cdot 10^{-4} \cdot e^{-\frac{5833.5}{T_g}} \qquad \left[\frac{mol}{m \cdot s \cdot Pa^{0.5}}\right]$$

Since the hydrogen fluxes are in series, by imposing $J_f = J_m$ it is possible to obtain the hydrogen flux J_{H2} as a function of P_{H2} and $P_{H2,SG}$:

$$J_{H2} = -\frac{2 \cdot \sqrt{P_{H2,SG}}/R_m + k_f/R_m^2}{2} + \frac{\sqrt{\left(2\sqrt{P_{H2,SG}}/R_m + k_f/R_m^2\right)^2 - 4 \cdot \frac{P_{H2,SG} - P_{H2}}{R_m^2}}}{2}$$

5.5 Numerical method

The mathematical model, constituted by differential equations of material balances and heat balances, has to be numerically solved, so it is necessary to approximate the problem with differential formulas [170].

From the solution of these approximated equations, scalar values of unknown functions can be obtained, that are a series of values that correspond to a set of points on the domain.

These values are the scalar unknown quantity of the “approximate problem”, that substitutes the real problem.

The differential equations with partial derivative represent a good relation on all the points of the integration domain.

For this reason, it is possible to write for each point an equation as long as the partial derivatives are expressed in function of the scalar unknown quantity.

The expressions of the partial derivative approximate from functions with scalar unknown quantity determine the solve method adopted, implicit or explicit. Moreover, depending on the way the partial derivative are expressed, there are discretization errors with respect to integration step in space and in time.

The truncation error, that represents the difference between the solution of the starting differential equation and its approximation, depends on the form of the truncation error itself (round off), related to finite dimension of the machine registry.

Another important information is the definition of local and global truncation error: the first corresponds to the difference between the exact solution starting from the previous step and the calculated value, whereas the second is the difference between the exact solution and the calculated value. In conclusion, the global error is due to combination of the different local errors but is not really the arithmetic sum.

The amplification of the errors in the solutions represents the so-called instability phenomenon of numerical method chosen.

A method is defined stable if the difference between the exact solution of the initial problem (without approximation) and numerically calculated value (with approximation) does not diverge for infinite time.

The stability of a numerical method depends both on the solve method and on the form of the starting differential equation, so if the sample differential equation that have to be solved is fixed, it is possible evaluate the extreme stability of a method.

5.6 Discretization of the system

From previous discussions, it is gathered that, in order to solve the model numerically, it has to be divided in "nodes", that is, a series of volumes with little but finite dimensions.

The nodes are numerated, in the space, along the axis of the system (Figure 5.9); the inlet and outlet nodes (respectively 0 and n+1) are simply nodes of convective transport.

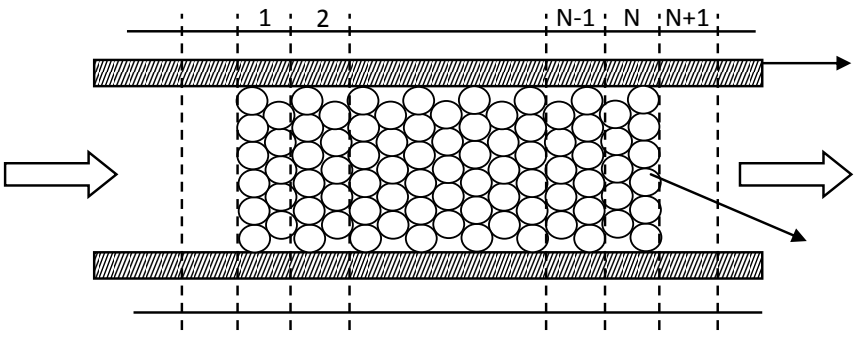

Figure 5.9 Schematization of the spatial discretization of the system

After the discretization of the system in the space, it is possible to formulate a differential equation for each node that will be ordinary type, because it is differentiable only in the time.
The chosen spatial discretization method is the backward finite difference formula, that is, in node i the expression of first derivative (since in this case there are not diffusive terms, so there are not second derivatives) will be approximated:

$$\left.\frac{\partial y}{\partial z}\right|_i = \frac{y_i - y_{i-1}}{\Delta z} + O(\Delta z^2)$$

where y represents the generic unknown function and i the nodes studied.

So the model is constituted of a set of ordinary differential equations (ODE) that are solved by means of numerical methods with a computer.
With this aim it was chosen a solver found in the library of the software of "WolframResearch" Mathematica® that is named NDsolve.
The syntax of this solver is the following:

sol = NDSolve[{SYS, ICs}, SOLs, {t, 0, t_f}]

The final instant of time t_f was set at a large value, since the interest in this work is in the solution at steady state.
The vectors SYS, ICs and SOLs are defined in Figure 5.10 for the case of the pseudo-homogeneous membrane reactor model.
SYS is a vector that contains all the discretized equations that describe the system; each equation is a system of n differential equations in the time.
ICs is the vector of the initial conditions (at t = 0) of each variable (mass species fractions and temperatures).
SOLs is the vector of the solutions, that is the output of the problem.
These vectors are defined in Mathematica through the syntax "Table", that allows to create a vector of a desired number of elements (n elements in our case).
The software calculates the numerical solution of each system, employing the explicit Runge-Kutta method as integration method, which order is automatically

managed by the solver (this is a default option, but a manually management is possible).

```
(*Initial Conditions*)
ic1 = Table[{y_CO,i[0] == y_CO,feed}, {i, 1, n}];
ic2 = Table[{y_H2O,i[0] == y_H2O,feed}, {i, 1, n}];
ic3 = Table[{y_H2,i[0] == y_H2,feed}, {i, 1, n}];
ic4 = Table[{y_CO2,i[0] == y_CO2,feed}, {i, 1, n}];
ic5 = Table[{y_H2SG,i[0] = y_H2SG,feed}, {i, 1, n}];
ic6 = Table[{T_g,i[0] = T_g,feed}, {i, 1, n}];
ic7 = Table[{T_SG,i[0] = T_SG,feed}, {i, 1, n}];

(*Solutions*)
s1 = Table[y_CO,i, {i, 1, n}];
s2 = Table[y_H2O,i, {i, 1, n}];
s3 = Table[y_H2,i, {i, 1, n}];
s4 = Table[y_CO2,i, {i, 1, n}];
s5 = Table[y_H2SG,i, {i, 1, n}];
s6 = Table[T_g,i, {i, 1, n}];
s7 = Table[T_SG,i, {i, 1, n}];

SYS = Join[sys1, sys2, sys3, sys4, sys5, sys6, sys7];
ICs = Join[ic1, ic2, ic3, ic4, ic5, ic6, ic7];
SOLs = Join[s1, s2, s3, s4, s5, s6, s7];
```

Figure 5.10 Definition of the problem in Mathematica

As regards the conventional fixed bed reactor or the membrane reactor with the sweep gas in co-current configuration, the solution of the problem is “standard” since the variables at each node i are influenced by the values at the nodes placed before along reactor axis. The problem arises in the case of the membrane reactor model with sweep gas in counter-current configuration; in this case, the flow of the sweep gas is in the opposite direction with respect to the axis direction (that is reactant flow), therefore the computational efforts are higher.

The discretization of the permeate side of the membrane result to be the same, and a backward formula is applied; the flow direction requires to change the index in the discretization for the balances on the permeate side:

$$\left.\frac{\partial \cdot}{\partial z}\right|_i = \frac{\cdot_{i+} - \cdot_i}{\Delta z} +)(\Delta(^2)$$

Moreover, the membrane reactor model requires a discretization of the continuity equation; while in the conventional reactor it is possible to impose that $\rho_{g,i} \cdot v_i = \rho_{g,feed} \cdot v_{feed}$, this is not possible in the model of the membrane reactor, since there is the flux of hydrogen that makes the mass flux vary. In this case, it was necessary to implement a "For Cycle" in Mathematica, reported as it follows in the case of counter-current sweep gas flow mode:

$$v_0 = v_{feed}$$

$$v_{SG,0} = v_{SG,feed}$$

$$\text{For}\left[i = 1, i < n+1, i+ \text{-}, v_i = v_{i-1} \cdot \frac{\rho_{g,i-1}}{\rho_{g,i}} - h \cdot \frac{PM_{H2} \cdot \pi \cdot (\text{-}_i + 2 \cdot \delta)}{\varepsilon \cdot A} \cdot \frac{J_{H2,i}}{\rho_{g,i}} \right]$$

$$\text{For}\left[i = 1, i < n+1, i+ \text{-}, v_i = v_{SG,i+1} \cdot \frac{\rho_{SG,i+1}}{\rho_{SG,i}} + h \cdot \frac{PM_{H2} \cdot \pi \cdot (\text{-}_i + 2 \cdot \delta)}{A_{SG}} \cdot \frac{J_{H2,i}}{\rho_{SG,i}} \right]$$

Where h in the integration step, defined as the ratio between the reactor length L and the number of nodes n.

As mentioned above, the value of the velocity of the sweep gas at index i depends on the value at index i+1.

5.7 Validation of the conventional fixed bed reactor model

The first step in the development of the model consists in its validation on the basis of the results reported in literature; a first comparison was performed on the basis of the data reported by Choi et al. [104] in a study for the determination of the kinetic mechanism.

The experimental conditions are reported in Table 5.7.

The feed was constituted by CO, H_2O and H_2, and the H_2/CO ratio was kept fixed at the value of 2.

The comparison of the model with the experimental data is reported in Figure 5.11. The figure reports the effect of the water to carbon monoxide inlet molar ratio, H_2O/CO, on the CO conversion x_{CO}, for various reaction temperature.
It is possible to observe that there is a good agreement between experimental data and model results for all the temperature values investigated.

Configuration	Fixed Tubular Reactor
d_i	1.27 cm
m_{CAT}	1 gr
d_P	200-250 μm
GHSV	6100 hr^{-1}

Table 5.7 Experimental condition in the work of Choi et al. [104]

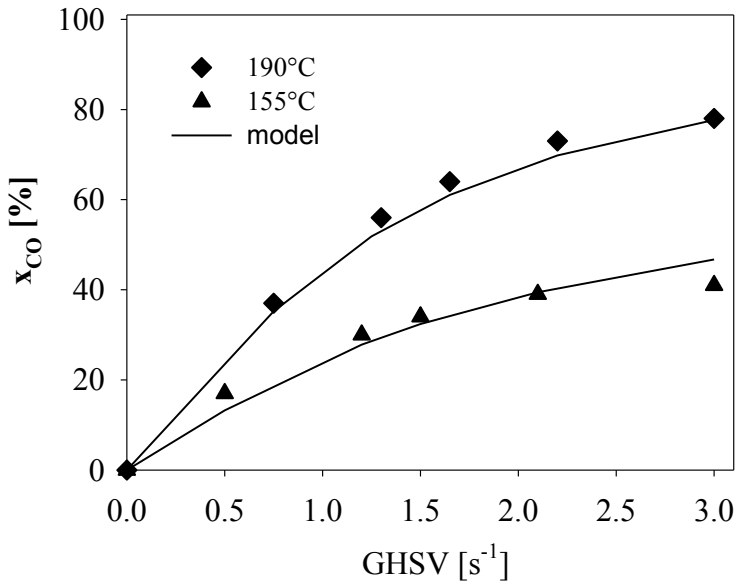

Figure 5.11 Comparison of the model (continuous lines) with the experimental results (diamonds, triangles, [104]) in terms of CO conversion x_{CO} as a function of the inlet water to CO ratio H_2O/CO, for two different temperature values

It is worth mentioning that the experimental conditions were chosen in order to work in conditions that eliminate internal diffusion resistance in catalyst pores (indeed the value of the effectiveness factor was found equal to 1) and also the

operating conditions allow to simulate the system by means of a pseudo-homogeneous model, since the gas to particle resistance was negligible.
The same results were therefore obtained with the heterogeneous model and with the pseudo-homogeneous one.
Moreover, the experiments were performed at constant temperature, therefore the model is isothermal (no energy balance, the temperature is fixed at the inlet value).
The figure reports the results of the model achieved with the heterogeneous model, employing the Frossling equation for the gas to particle heat and mass transfer coefficient calculation.

5.8 Validation of the membrane reactor model

The validation of the membrane WGS reactor model was done on the basis of the data reported by Basile et al [108] for a membrane WGS reactor with a Pd based membrane for hydrogen separation.
The experimental conditions are reported in Table 5.8.
The comparison of the model with the experimental data is reported in Figure 5.12 as CO conversion as a function of sweep gas flow rate to reactants flow rate ratio Q_{SG}/Q. The continuous line is the one calculated with the model that employs the Temkin's kinetic mechanism. The scattered line is the one calculated with the model that employs the Langmuir-Hinshelwood kinetic mechanism.
It is possible to observe that the Langmuir-Hinshelwood mechanism strongly underestimates the CO conversion, due to the underestimation of the equilibrium shift. Therefore, the employment of the Temkin kinetic results to be more appropriate.
The validation of the membrane WGS reactor was done on the basis of the data reported by Criscuoli et al [106], that performed an experimental study on a membrane WGS reactor with a Pd membrane.
The experiments were performed in isothermal and isobaric conditions and reactor characteristics are reported in Table 5.9; a commercial Cu catalyst was employed; before testing the reactor, some permeation tests were performed in order to obtain the hydrogen permeability law.

Configuration	Fixed Tubular Reactor
d_i	1 cm
d_{OUT}	2 cm
L	30 cm
GHSV	1000 hr^{-1}
Δ	70 μm
T	604K
P	1 atm
P_{SG}	1 atm

Table 5.8 Experimental conditions in the work of Basile et al [108]

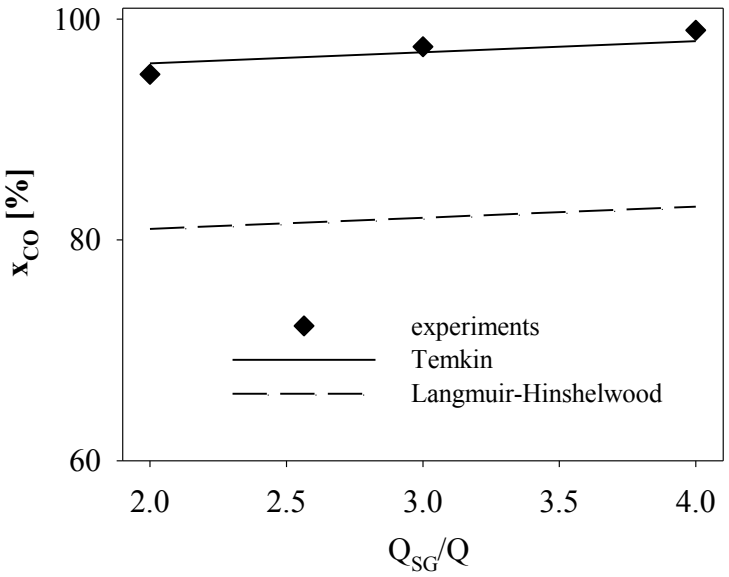

Figure 5.12 Comparison of the model (continuous and dotted lines) with the experimental results (squares, [108]) in terms of CO conversion x_{CO} as a function of the sweep gas to inlet flowrate ratio Q_{SG}/Q

The permeability of hydrogen was expressed by means of the Sievert's law and of the Arrhenius' law and was also verified on the basis of experimental data of Itoh et al [57]. The expression is reported in section 5.4.2.

The experiments were performed with sweep gas in co-current flow mode, with a flowrate of 43.6 ml/min. The comparison between experimental data and the

model is reported in Figure 5.13 for an inlet mixture of $CO/CO_2/H_2/N_2$ = 32/12/48/52 on dry basis.

Configuration	Fixed Tubular Reactor
d_i	0.8 cm
d_{OUT}	4 cm
L	15 cm
d_P	0.8 mm
Δ	70 μm
T	595K
P	1 atm
P_{SG}	1 atm

Table 5.9 Experimental condition in the work of Criscuoli et al. [106]

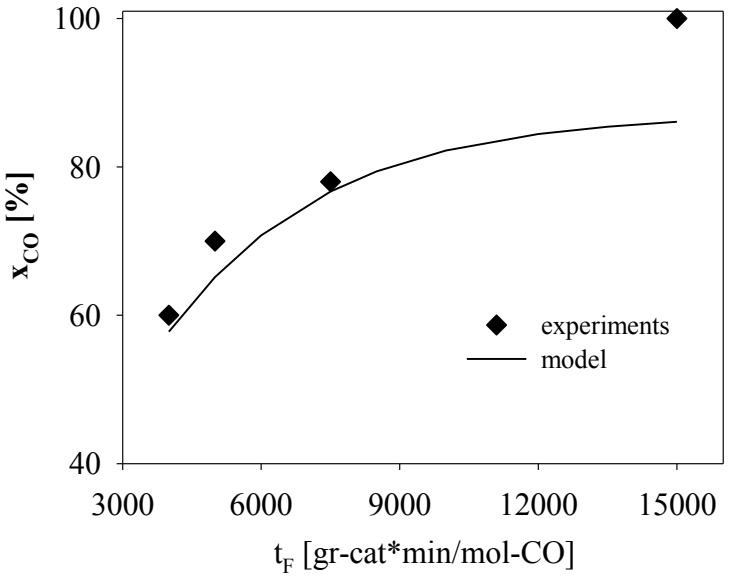

Figure 5.13 Comparison of the model (continuous line) with the experimental results (squares, [106]) in terms of CO conversion x_{CO} as a function of the reactor time factor t_f

The inlet water to carbon monoxide ratio, H_2O/CO, was fixed at 1.1. The figure reports the CO conversion x_{CO} as a function of the time factor t_f, expressed in

terms of m_{CAT}/n_{CO}. The range of t_f 4000-15000 gr-cat·min/mol-CO corresponds to a GHSV range of 0.3-1.2 s^{-1} at reaction temperature.

It is possible to observe that there is a good agreement between experimental data and model results at low time factor (4000-8000), whereas the experimental point at high t_f is not well fitted by the model. However, it is worth noting that this point does not seem to follow the trend of the experiments at low t_f, therefore it is possible that there is an overestimation of the CO conversion for that value of the time factor. The model proposed by Criscuoli in the same work showed the same results. Both our model and the model proposed by Criscuoli employs the Temkin's kinetic expression.

After model development and validation, the sizing of reactors has been performed. In particular, chapter 6 reports the sizing of both conventional HTS and LTS reactor and of the membrane WGS reactors. Together with reactor sizing, the comparison of the results obtained in Mathematica with the results obtained in AspenPlus is also reported.

Mathematical model: Results

As reported in the previous chapters, AspenPlus was employed for system optimization, by performing a thermodynamic analysis. Indeed, AspenPlus allows to perform equilibrium calculation and no sizing of the system is foreseen. Since the hydrogen production with a fuel processor is associated to small scale energy generation, it is important to work not only with a high efficient system, but also with a compact one. Therefore, the mathematical model developed in this work was used to size and compare the reactors wit and without the hydrogen separation membrane. In this way, an idea of the reaction volumes required by the CO clean-up section can be given.

The choice of sizing a water gas shift reactor was made by considering that the hydrogen separation membrane has got a limited thermal stability, therefore the operation of the membrane in a water gas shift reactor seems to be more feasible in the short term, since this reactor operates at temperatures that are compatible with membrane thermal stability.

The inlet compositions and the operating conditions (pressure, sweep gas to reactants inlet flow rate ratio Q_{SG}/Q_{IN}) were fixed at the values found in the optimization of the system configuration with AspenPlus. Both the CO clean-up section of the SR and the ATR systems were modeled.

As regards the conventional systems, the inlet composition to the HTS reactors is reported in Table 6.1, for the SR and the ATR case.

The composition of the inlet mixture to the LTS reactors is equal to the outlet composition of the HTS reactor, with the inlet temperature fixed at 473K.

As regards the membrane WGS reactors, the inlet composition and operating conditions, are reported in Table 6.2, both for the SR and the ATR case.

	HTS (SR system)	HTS (ATR system)
Inlet composition (mol)		
CO	0.099	0.032
H_2O	0.227	0.335
CO_2	0.072	0.081
H_2	0.585	0.293
N_2	0.017	0.259
P [atm]	1	1
$\mathbf{T_{IN}}$ [K]	623	623

Table 6.1 Operating conditions in the modeled HTS reactors in the SR and in the ATR based systems

	Membrane WGS (SR system)	Membrane WGS (ATR system)
Inlet composition (mol)		
CO	0.149	0.094
H_2O	0.171	0.159
CO_2	0.044	0.056
H_2	0.624	0.323
N_2	0.012	0.368
P [atm]	3	3
$\mathbf{T_{IN}}$[K]	573	573
SG configuration	-	Counter-current
$\mathbf{Q_{SG}}$ /$\mathbf{Q_{IN}}$	0.0	0.289
$\mathbf{P_{SG}}$ [atm]	1	1
$\mathbf{T_{SG,IN}}$	573	573

Table 6.2 Operating conditions in the modeled membrane WGS reactors in the SR and in the ATR based systems

The details of the geometry of the reactors and of catalyst characteristics employed in the model are reported in Table 6.3.

	HTS/LTS	Membrane WGS
d_i [cm]	1	1
d_{OUT} [cm]	-	1.2
δ [μm]	-	10-100
L [cm]	1-12.5	1-12.5
d_P [mm]	1	1
ρ_{CAT} [gr/cm^3]	5.9/2.4 [109]	2.4
k_S [W/m·K]	0.3	0.3

Table 6.3 Operating conditions in the modeled reactors.

The determination of reactor volumes was made by fixing the quantity of hydrogen that needs to be produced for generating 1 kW of electric energy in the PEMFC, according to the following formula:

$$P_e = \eta_{FC} \cdot n_{H2} \cdot LHV_{H2}$$

Considering an electrochemical efficiency of the PEM fuel cell equal to 60%, as performed for the calculations made with AspenPlus, the hydrogen flowrate that needs to be produced to get 1 kW of electric energy is equal to 0.6 Nm^3/hr.

Both for the conventional and the membrane reactors, an important parameter often defined in theoretical and experimental works is the Gas Hourly Space Velocity, GHSV [hr^{-1}] defined as the ratio between the inlet gas flowrate Q_{IN} and the catalyst volume V_S:

$$GHSV = \frac{Q_{IN}}{V_S}$$

with $V = \varepsilon \cdot A \cdot L$.

The reactor cross section for the conventional reactor is evaluated as:

$$A = \frac{\tau \cdot d_i^2}{4}$$

whereas reactor cross section for the membrane reactor is evaluated as the annulus area:

$$A = \frac{\pi \cdot \left(d_{OUT}^2 - \left(d_i + 2 \cdot \delta \right)^2 \right)}{4}$$

where d_{OUT} is the internal diameter of the outlet tube, d_i is the internal diameter of the membrane and δ is membrane thickness.

According to these definitions, the GHSV is substantially the reverse of the residence time inside the reactor, defined as L/v. In the present work, since the velocity is not constant along the reactor, it will be defined on the basis of the inlet velocity.

6.1 Modeling of the conventional CO clean-up section

In the case of conventional system, since the stream sent to the PEMFC is the outlet of the PrOx reactor, the loss of hydrogen in this reactor must be taken into account. By employing AspenPlus, with a Design Specification it is possible to find the flowrate at the inlet of the HTS reactor and of the LTS reactor in order to respect the hydrogen flowrate required to the PEM fuel cell. With this calculation, the total flowrate sent to the HTS reactor is equal to 1.2 Nm^3/hr in the SR case and to 2.4 Nm^3/hr in the ATR case.

The effect of main parameters is presented for the HTS reactor in the Steam Reforming case. In particular, Figure 6.1 reports the CO conversion x_{CO} as a function of reactor length L parametric in fluid velocity. As expected, at fixed velocity the CO conversion increases with increasing reactor length. The same trend is observed if reactor length is kept fixed and the velocity is reduced inside the reactor. Indeed, a reduction of velocity, as well as an increase of reactor length, goes in the direction of increasing the residence time in the reactor itself, allowing more time to reactants for conversion to products.

The effect of GHSV, that is the reverse of the residence time L/v, on reactor performance is reported in Figure 6.2, that shows the trend of x_{CO} as a function of GHSV parametric in fluid velocity. It is observed that the velocity does not affect the trend of x_{CO} as a function of GHSV, that shows a plateau until GHSV values of about 3.0-4.0 s^{-1} and then decreases with increasing the GHSV.

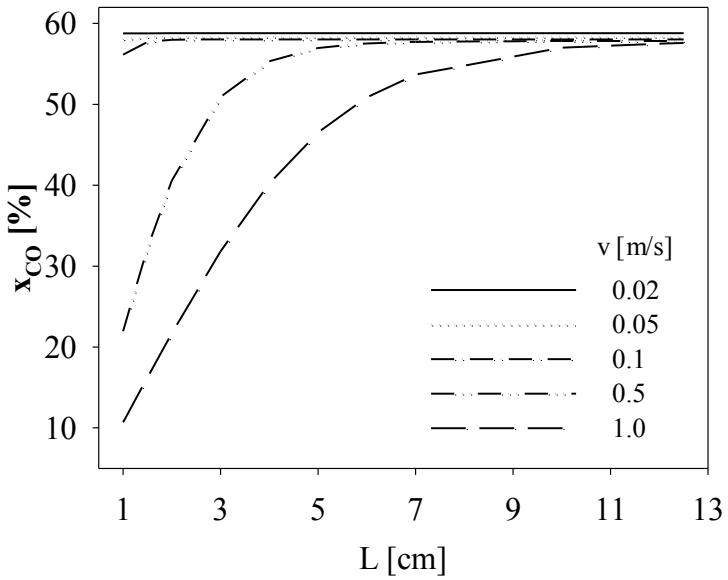

Figure 6.1 CO conversion, x_{CO}, as a function of reactor length L parametric in fluid velocity. k_s = 0.3 W/m·K. HTS reactor model. Inlet composition: SR case.

The negligible effect of velocity is due to the fact that the reactor operates is modeled as a PFR with an axial dispersion term that depends on fluid velocity, in particular on the Peclet number; in the range of v and L investigated, the reactor works in conditions of small deviation from Plug Flow (Levenspield [139]), therefore the trend with the GHSV is basically the same for each fluid velocity investigated.

Figure 6.3 shows x_{CO} as a function of GHSV parametric in catalyst thermal conductivity, for a reactor length of 10 cm. In the conditions investigated, the effect of k_S can be considered as negligible. The highest difference in the CO conversion is observed at low GHSV and is lower than 0.3%. This is due to the fact that the reactor operates in a middle temperature range and that the reaction is

weakly exothermic, therefore the effect of k_s on the temperature profile is negligible.

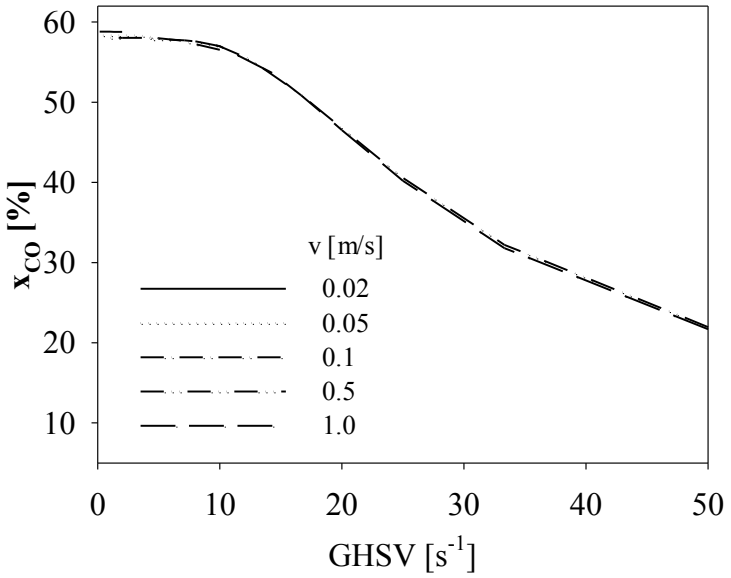

Figure 6.2 CO conversion, x_{CO}, as a function of GHSV parametric in fluid velocity. k_s = 0.3 W/m·K. HTS reactor model. Inlet composition: SR case.

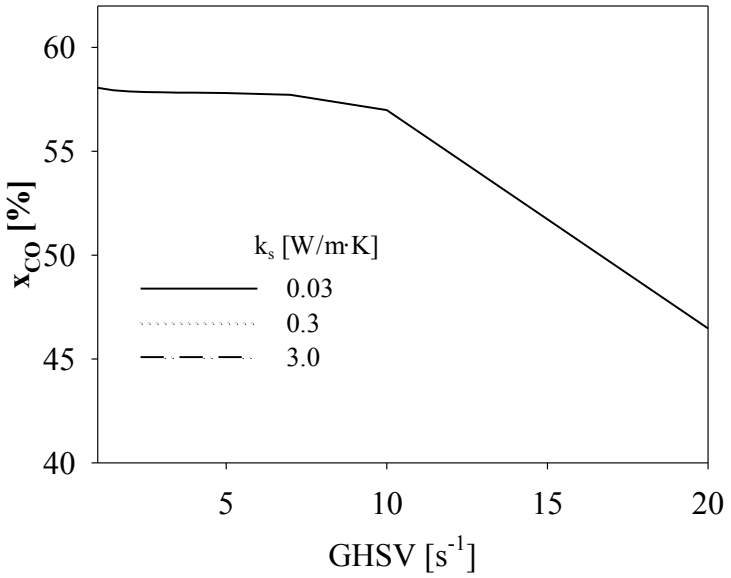

Figure 6.3 CO conversion x_{CO} as a function of GHSV parametric in catalyst thermal conductivity k_s. L = 10 cm. HTS reactor model. Inlet composition: SR case

By observing the trend on the CO conversion as a function of the GHSV, it is possible to observe that a plateau in the conversion is present until GHSV values of 3.3 s^{-1}. If 2.4 Nm^3/hr are fed to the reactor, the corresponding volume is 1.1 lt.

The stream produced in the HTS reactor is used as input to the LTS reactor and the same procedure was applied for sizing LTS reactor; the CO conversion as a function of GHSV is reported in Figure 6.4, for a value of k_S equal to 0.3 W/m·s. Also in this case, the CO conversion has a plateau for low GHSV values and then it starts to decrease with reducing the residence time inside the reactor.
This reactor is optimized for a GHSV of 3.5 s^{-1}, therefore the volume required by this reactor is 0.8 lt.
From literature [171], it was found that a typical GHSV for the PrOx reactor was 1.1 s^{-1}. This reactor was not model in this work since the reaction kinetics on the typical PrOx catalyst are not well defined in literature, therefore the determination of the reactor volumes with the employment of the experimental data seemed to be more accurated. With the flowrate determined in this work, the PrOx reactor volume is equal to 0.3 lt.

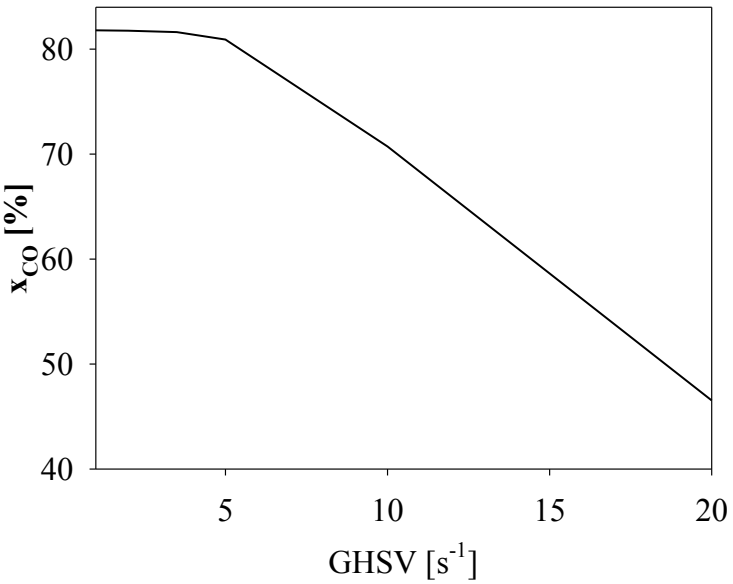

Figure 6.4 CO conversion x_{CO} as a function of GHSV. L = 10 cm, k_s = 0.3 W/m·K. LTS reactor model. Inlet composition: SR case.

From this calculation, the global volume of the three reactors that constitute the CO clean-up section of the conventional fuel processor based on the Steam Reforming process is equal to 1.3 lt.

This value does not take into account the volume of the heat exchangers placed downstream each reactor, but it is only the volume required by reactions for lowering the CO content to less than 10 ppm.

The summary of the results for sizing the conventional CO clean-up section is reported in Table 6.4.

	HTS	**LTS**	**PrOx**
GHSV [s^{-1}]	3.3	3.5	1.1
V [lt]	0.6	0.4	0.3

Table 6.4 GHSV and Volume values that optimize the three reactors of the conventional CO clean-up section. Total flowrate Q_0 = 1.2 Nm^3/hr. SR case.

As regards the comparison with AspenPlus, Table 6.5 reports the outlet conditions from the HTS and LTS reactor obtained both with Aspen Plus and Mathematica.

	AspenPlus	**Mathematica**	**AspenPlus**	**Mathematica**
	HTS	**HTS**	**LTS**	**LTS**
Outlet composition				
CO	0.044	0.042	0.008	0.008
H_2O	0.172	0.170	0.136	0.136
CO_2	0.127	0.129	0.163	0.163
H_2	0.640	0.642	0.676	0.676
N_2	0.017	0.017	0.017	0.017
P [atm]	1	1	1	1
T_{OUT} [K]	686	674	517	512
GHSV [s^{-1}]	-	3.3	-	3.5
x_{CO} [%]	56.0%	58.0%	81.8%	81.6%

Table 6.5 Outlet conditions from the HTS and LTS reactors with AspenPlus model and Mathematica model. SR case

It is possible to observe that only slight differences are observed in the CO conversion due to differences in the predicted outlet temperature. In particular, the CO conversion in the HTS reactor modeled in Mathematica was found equal to 58.0%, with an outlet temperature of 401°C. In AspenPlus, the conversion was found to be equal to 56%, with an outlet temperature of 413°C.

The sizing of the conventional CO clean-up section in the case of Autothermal Reforming system was performed in the same way of what presented for the Steam Reforming case. The qualitative trend of the CO conversion with GHSV is the same in the two cases, both for the HTS reactor and for the LTS reactor. As showed in Figure 6.5, the CO conversion in the HTS reactor shows a plateau with the GHSV, until a GHSV value of around 3.0 s^{-1}, and then it decreases with lowering the residence time in the reactor. The same trend is observed in the LTS reactor, as reported in Figure 6.6. In this case, a plateau value of around 79.0% in the conversion is maintained until a GHSV value of around 5.0 s^{-1}.
The differences in conversion values between the SR and the ATR case are obviously addressed to the different inlet composition to the HTS reactor.

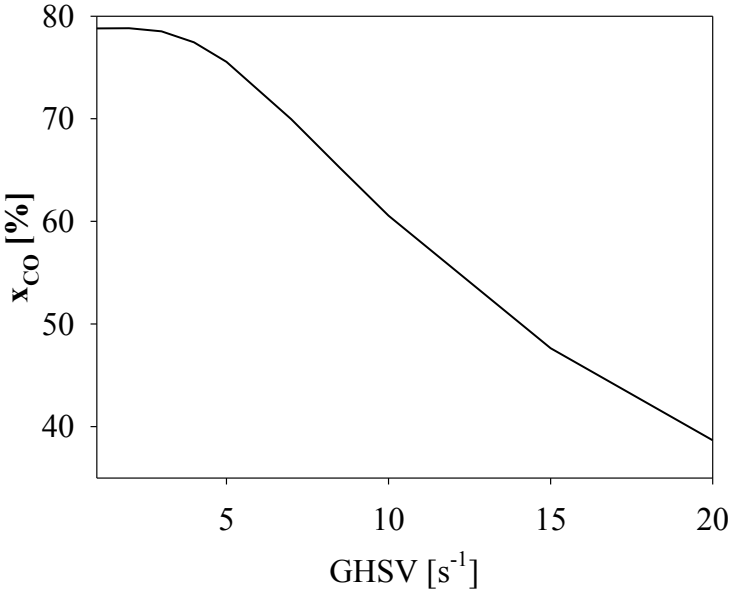

Figure 6.5 CO conversion x_{CO} as a function of GHSV. L = 10 cm, ks = 0.3 W/m·K. HTS reactor model. Inlet composition: ATR case

In order to produce 1 kW of electric energy, the inlet flowrate to the HTS reactor must be equal to 2.4 Nm^3/hr; this corresponds to a volume of 1.2 lt for the HTS reactor and of 0.6 lt for the LTS reactor.

To complete the sizing of the CO clean-up section in the ATR case, the GHSV for the PrOx reactor was fixed at 1.1 s^{-1}, as in the SR case. With the flowrate of 2.4 Nm^3/hr required to produce 1 kW of electric energy in the ATR based system, the PrOx reactor volume is equal to 0.6 lt.

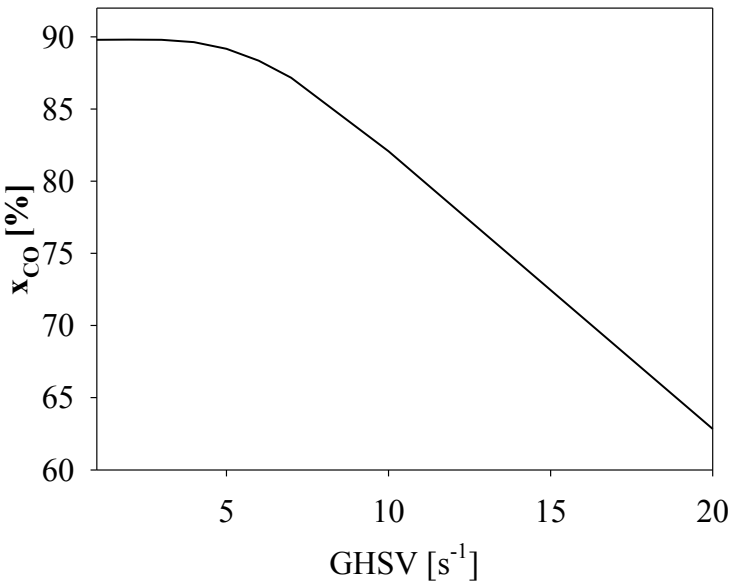

Figure 6.6 CO conversion x_{CO} as a function of GHSV. L = 10 cm, ks = 0.3 W/m·K. LTS reactor model. Inlet composition: ATR case

From this calculation, the global volume of the three reactors that constitute the CO clean-up section of the conventional fuel processor based on the Autothermal Reforming process is equal to 2.4 lt.

Also in this case, this value does not take into account the volume of the heat exchangers placed downstream each reactor, but it is only the volume required by the reaction for lowering the CO content to less than 10 ppm at the outlet of the PrOx reactor.

The summary of the results for sizing the conventional CO clean-up section is reported in Table 6.6.

	HTS	LTS	PrOx
GHSV [s^{-1}]	3.3	5.0	1.1
V [lt]	1.2	0.6	0.6

Table 6.6 GHSV and Volume values that optimize the three reactors of the conventional CO clean-up section. Total flowrate Q_0 = 2.4 Nm^3/hr. ATR case.

The comparison with AspenPlus is reported in Table 6.7. Also in this case there is a good agreement between Mathematica and AspenPlus results, confirming that if the GHSV is low enough the Water Gas Shift reactors reach the equilibrium conversion.

	AspenPlus	Mathematica	AspenPlus	Mathematica
	HTS	HTS	LTS	LTS
Outlet composition				
CO	0.005	0.006	400 ppm	500 ppm
H_2O	0.347	0.348	0.343	0.343
CO_2	0.102	0.101	0.106	0.106
H_2	0.302	0.301	0.306	0.306
N_2	0.244	0.244	0.244	0.244
P [atm]	1	1	1	1
$\mathbf{T_{OUT}}$ **[K]**	646	644	479	479
GHSV [s^{-1}]	-	3.5	-	5
$\mathbf{x_{CO}}$ [%]	80.8%	78.8%	92.0%	89.1%

Table 6.7 Outlet conditions from the HTS and LTS reactors with AspenPlus model and Mathematica model. ATR case.

6.2 Modeling of the membrane WGS reactor

After the modeling of the conventional reactors, the membrane WGS reactors were modeled and dimensioned in the SR and in the ATR case. The first results are presented for the SR case, with an inlet composition to the reactor reported in Table 6.2. The details of the geometry of the reactor are reported in Table 6.3.

Simulation were performed by varying the main operating parameters that size the reactor, that is the reactor length L and the fluid velocity v. The performance in terms of GHSV were also investigated. As already discussed in previous chapters, in the membrane reactor the driving force to hydrogen permeation is the difference of hydrogen partial pressure between the retentate and the permeate side of the membrane; therefore, also pressure, sweep gas to reactants flowrate inlet ratio and membrane thickness were investigated as operating variables.

The trend of the CO conversion x_{CO} and of the hydrogen recovery HR as a function of GHSV parametric in the inlet fluid velocity v are reported in Figure 6.7. The operating conditions in terms of pressure, sweep gas to inlet flowrate ratio and composition are referred to the optimum found in the optimization of the system with AspenPlus, and are reported in Table 6.2.

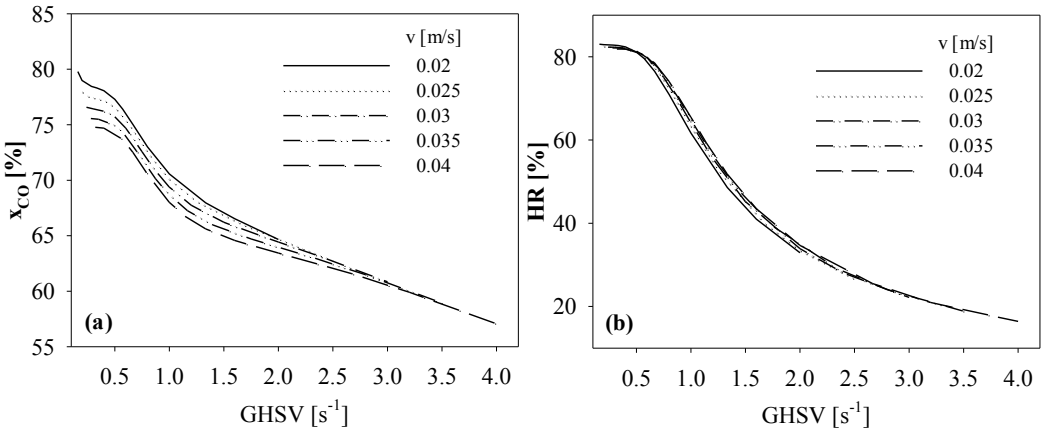

Figure 6.7 CO conversion x_{CO} (a) and hydrogen recovery HR (b) as a function of gas hourly space velocity GHSV parametric in fluid velocity v. Operating conditions: P = 3 atm, Q_{SG}/Q_{IN} = 0, δ = 30 μm. SR case.

It is possible to observe that, at fixed velocity, the performance of reactor increase with increasing the GHSV, since the mixture has got a higher volume for reaction and a higher membrane area for hydrogen permeation.

However, differently from the conventional case, it is possible to observe that the CO conversion trend with GHSV is affected by the mixture velocity, and the plateau reached at low GHSV is different in various cases.

This result suggests that the reactor performance in the case of membrane reactor cannot be described only in term of GHSV. Indeed, if the data showed in Figure 6.7 are reported with the reactor lenght on the horizontal axis (Figure 6.8), it is possible to observe that the CO conversion reaches different plateau with changing the velocity (see Figure 6.8 (a)). The hydrogen recovery is less affected by the fluid velocity in the plateau zone, indeed the curves of HR as a function of L reach the same plateau value of about 80.0% (Figure 6.8 (b)) and the conversion in the graph of HR as a function of GHSV gives substantially and independence from the velocity (Figure 6.7 (b)).

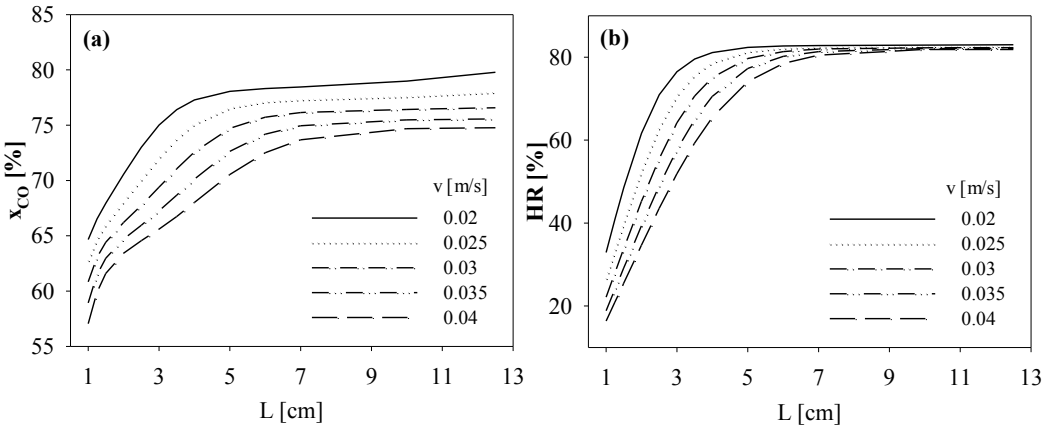

Figure 6.8 CO conversion x_{CO} (a) and hydrogen recovery HR (b) as a function of reactor length L parametric in fluid velocity v. Operating conditions: P = 3 atm, Q_{SG}/Q_{IN} = 0, δ = 30 μm. SR case.

Figure 6.9 shows the trend of x_{CO} and HR as a function of reactor length parametric in membrane thickness at a fixed fluid velocity v of 0.025 m/s. As already observed in Figure 6.7, reactor performance increase with increasing reactor length for all the values of δ investigated. In the case of ultra thin membrane (10 μm) the CO conversion and the hydrogen recovery reach a plateu value of around 78.0% and 80.0%, respectively, for reactor lengths above 2 cm. Quite the same plateau values are reached in the case of low membrane thickness (30 μm), although the corresponding minimum reactor length increases to 5 cm. a higher membrane thickness (100 μm) does not allow to reach the plateau value in the range of lengths investigating, indicating that the quality of the membrane and,

thus, the effectiveness of hydrogen separation strongly affect the performance of the membrane reactor.

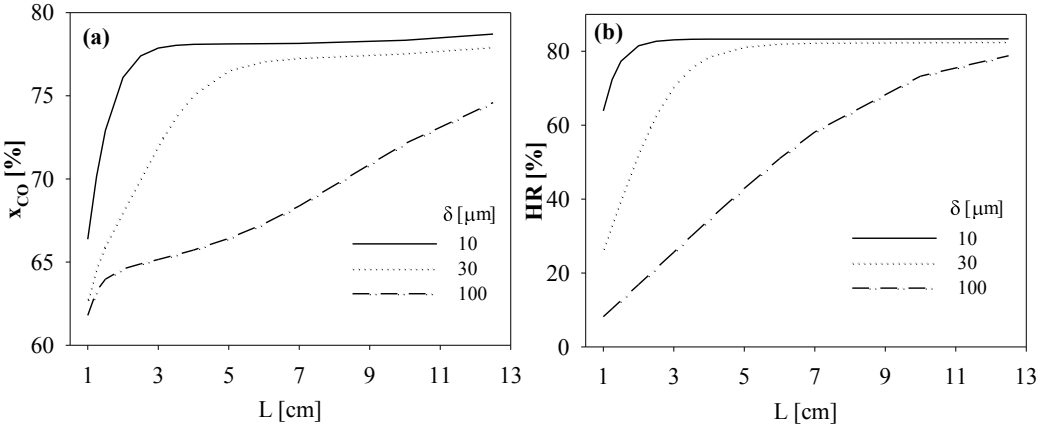

Figure 6.9 CO conversion x_{CO} (a) and hydrogen recovery HR (b) as a function of reactor length L parametric in membrane thickness δ. Operating conditions: P = 3 atm, Q_{SG}/Q_{IN} = 0, v = 0.025 m/s. SR case.

The effect of pressure on system performance is reported in Figure 6.10, for a reactor length of 10 cm, a fluid velocity of 0.025 m/s and a membrane thickness of 30 μm. It is possible to observe that CO conversion and hydrogen recovery increase with increasing pressure, since an increase of pressure favors the hydrogen permeation which in turns acts positively on reaction equilibrium.

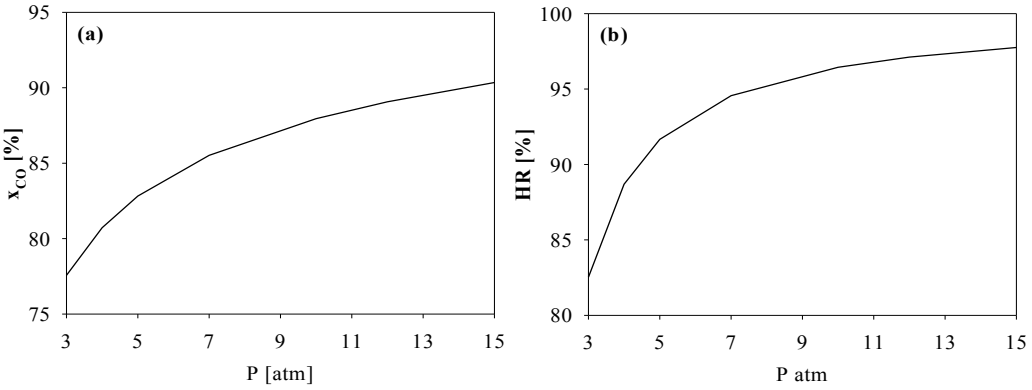

Figure 6.10 CO conversion x_{CO} (a) and hydrogen recovery HR (b) as a function of pressure P. Operating conditions: Q_{SG}/Q_{IN} = 0, v = 0.025 m/s, L = 10 cm, δ = 30 μm. SR case.

However, the value of hydrogen pressure of the retentate side cannot be lower than 1 atm, that corresponds to the hydrogen partial pressure value on the permeate side when no sweep gas is employed in the system, therefore x_{CO} and HR cannot reach the 100%. This condition, instead, is possible in the case of employing sweep gas on the permeate side of the membrane, allowing hydrogen dilution with a consequent increase of the hydrogen separation driving force through the membrane.

The trend of x_{CO} and HR as a function of Q_{SG}/Q_{IN} is reported in Figure 6.11. As it is possible to observe, the conversion can reach the 100% value, as well as the hydrogen recovery, when a high sweep gas flowrate is sent on the permeate side of the membrane. The results showed in Figure 6.11 were obtained in the case of counter-current sweep gas flow mode, that was found to be the best mode in term of distribution of the hydrogen separation driving force along the reactor axis.

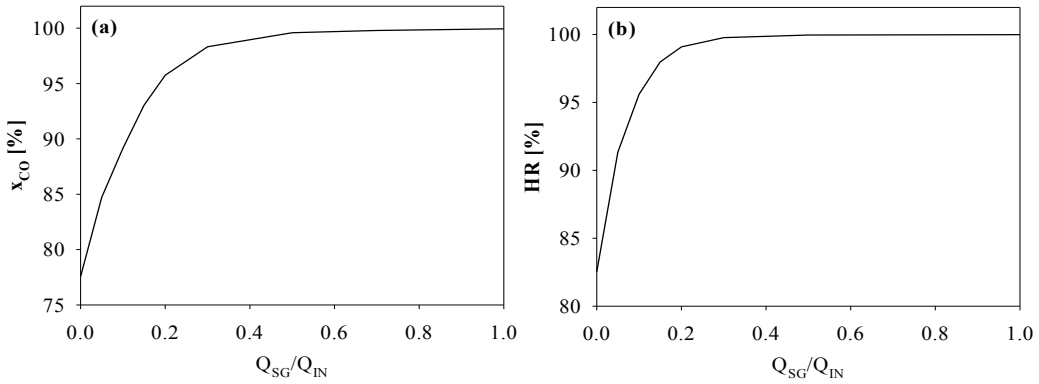

Figure 6.11 CO conversion x_{CO} (a) and hydrogen recovery HR (b) as a function of pressure sweep gas to inlet flow rate ratio Q_{SG}/Q_{IN}. Operating conditions: P = 3 atm, v = 0.025 m/s, L = 10 cm, δ = 30 μm. SR case.

As described in the previous chapters, the membrane WGS reactor placed in a SR based system is not optimized at high sweep gas flowrates and at high pressure because the optimization was made in terms of global energy efficiency of the entire system. The results of Figure 6.10 and 6.11 show that the membrane WGS reactor placed in the SR system operates in conditions that do not maximize the CO conversion and the hydrogen recovery, because the integration of the reactor

in the system requires that not all the CO is converted in H_2 and not all the H_2 permeates the membrane.

In order to size the membrane reactor for producing 1 kW of electric energy, the case of a membrane thickness of 30 μm was considered, as compromise between hydrogen permeability and membrane stability. With this membrane thickness, considering a velocity of 0.025 m/s, the membrane reactor volume is equal to 1.1 lt (1.5 lt considering also the permeate side volume). With this volume, the encumbrance of the CO clean-up section in the SR case is reduced, since are less heat exchangers required in the process. Quite the same values are achieved if a higher velocity is considered for sizing the reactor. At 0.04 m/s of inlet velocity, the reaction volume is equal to 1.5 lt. The reaction volumes can be strongly reduced if ultrathin membranes of 10 μm, such as supported palladium membranes, are employed in the reactor; in this case, the reaction volume lowers to 0.5 lt (0.75 lt with the permeate side volume) at 0.025 m/s and to 0.55 lt (0.8 lt with the permeate side volume) at 0.04 m/s. Therefore, this result shows that the introduction of the membrane in the fuel processor – PEM fuel cell system is convenient both in term of energy efficiency and of system compactness.

The results obtained for the membrane WGS reactor in the ATR case are qualitatively the same of what discussed above. Figure 6.12 reports the trend of x_{CO} and HR as a function of reactor length parametric in the inlet fluid velocity, at P = 3 atm and without sweep gas. The composition of the inlet mixture is the one found in the system optimization with AspenPlus, and reported in Table 6.2. Figure 6.13 reports the same results x_{CO} (a) and HR (b) as a function of GHSV parametric in inlet fluid velocity.

At fixed fluid velocity, x_{CO} and HR increase with increasing the reactor length; the same trend in observed at fixed reactor length with reducing fluid velocity. it is possible to observe that the hydrogen recovery values in the plateau zone are lower than what achieved in the SR case (25.0% against 80.0%) mainly due to the lower hydrogen concentration at reactor inlet.

Also in this case, it is possible to observe that the CO conversion does not reach the same plateau at each velocity investigated, therefore when the results are expressed in terms of GHSV there is a slight dependence from fluid velocity, as reported in Figure 6.13 (a), at low GHSV values.

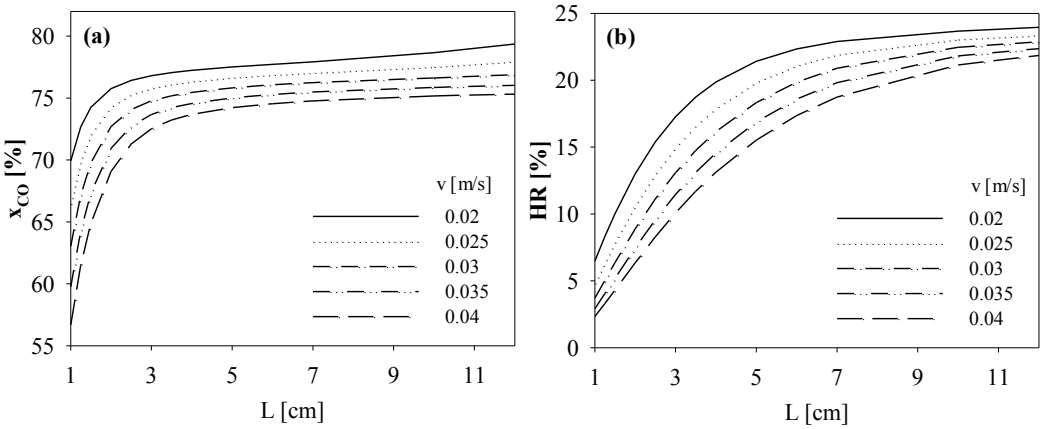

Figure 6.12 CO conversion x_{CO} (a) and hydrogen recovery HR (b) as a function of reactor length L parametric in fluid velocity v. Operating conditions: P = 3 atm, Q_{SG}/Q_{IN} = 0, δ = 30 μm. ATR case.

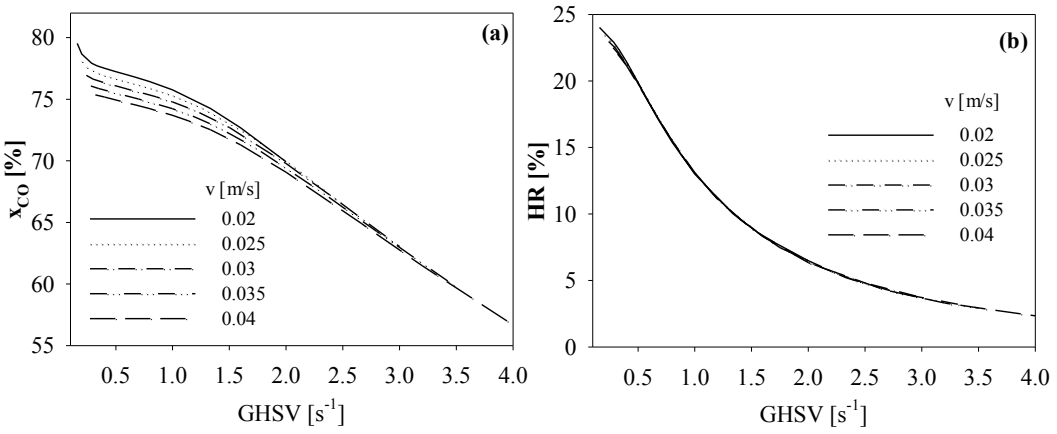

Figure 6.13 CO conversion x_{CO} (a) and hydrogen recovery HR (b) as a function of gas hourly space velocity GHSV parametric in fluid velocity v. Operating conditions: P = 3 atm, Q_{SG}/Q_{IN} = 0, δ = 30 μm. ATR case.

The effect of membrane thickness is reported in Figure 6.14. As for the SR case, the ultrathin membrane allows to reach plateau values of x_{CO} and HR at relatively

short reactor length, whereas the increase of the membrane thickness up to 100 μm does not allow to reach the plateau values. The effect is marked in particular on the HR trend, that is strongly related to the hydrogen separation effectiveness, therefore strongly depends on the quality of the separation and, thus, on the membrane thickness.

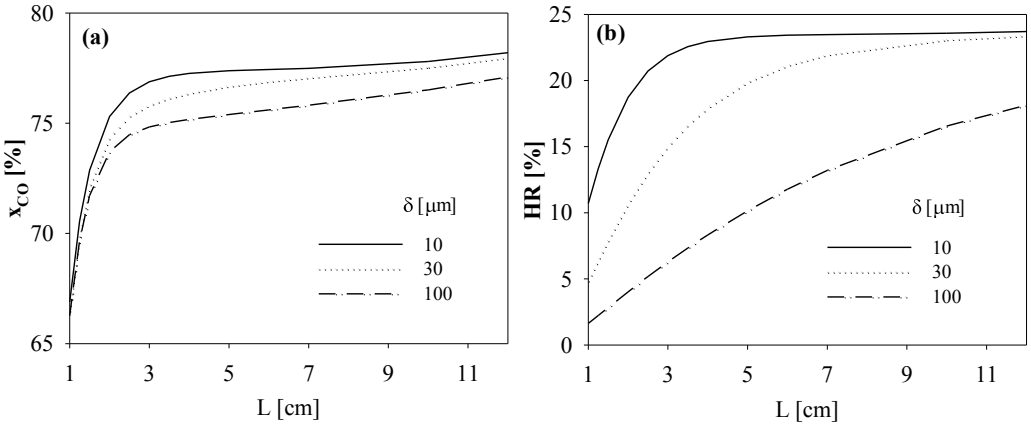

Figure 6.14 CO conversion x_{CO} (a) and hydrogen recovery HR (b) as a function of reactor length L parametric in membrane thickness δ. Operating conditions: P = 3 atm, Q_{SG}/Q_{IN} = 0, v = 0.025 m/s. ATR case.

Figure 6.15 reports the effect of pressure on x_{CO} and HR at Q_{SG}/Q_{IN} = 0 and Figure 6.16 reports the effect of Q_{SG}/Q_{IN} on x_{CO} and HR at P = 3 atm. The results are obtained in the case of reactor length of 10 cm, a fluid velocity of 0.025 m/s and a membrane thickness of 30 μm. It is possible to observe that, without the addition of sweep gas, in the pressure range investigated no plateau values are reached both for CO conversion and hydrogen recovery (see Figure 6.15). This is due to the lower hydrogen concentration at reactor inlet with respect to the SR case, that gives a lower separation driving force, therefore higher pressure values should be required in order to reach plateau values in the conversion and in the hydrogen recovery. With the addition of sweep gas, instead, the CO conversion and the hydrogen recovery reach the 100% values (see Figure 6.16), indicating that the addition of sweep gas allows to improve the hydrogen separation driving force to the highest level despite the lower hydrogen concentration in the feed.

It is worth noting that, due to the autothermal nature of the process, the optimization of the fuel processor – PEM fuel cell system based on ATR requires that the membrane WGS reactor operates in conditions that maximize the CO conversion and the hydrogen recovery. Therefore, in the case of ATR, differently from the SR case, the membrane WGS reactor operates in optimal conditions in terms of hydrogen separation driving force.

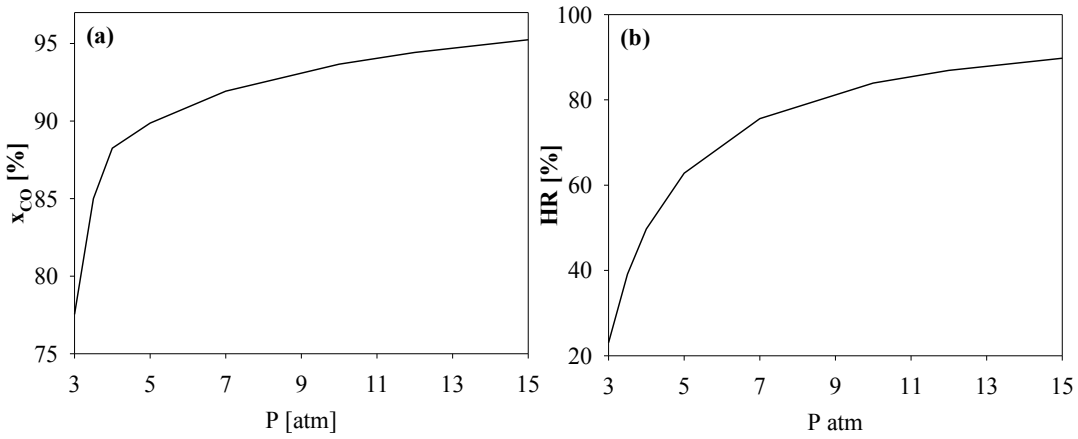

Figure 6.15 CO conversion x_{CO} (a) and hydrogen recovery HR (b) as a function of pressure P. Operating conditions: Q_{SG}/Q_{IN} = 0, v = 0.025 m/s, L = 10 cm, δ = 30 μm. ATR case.

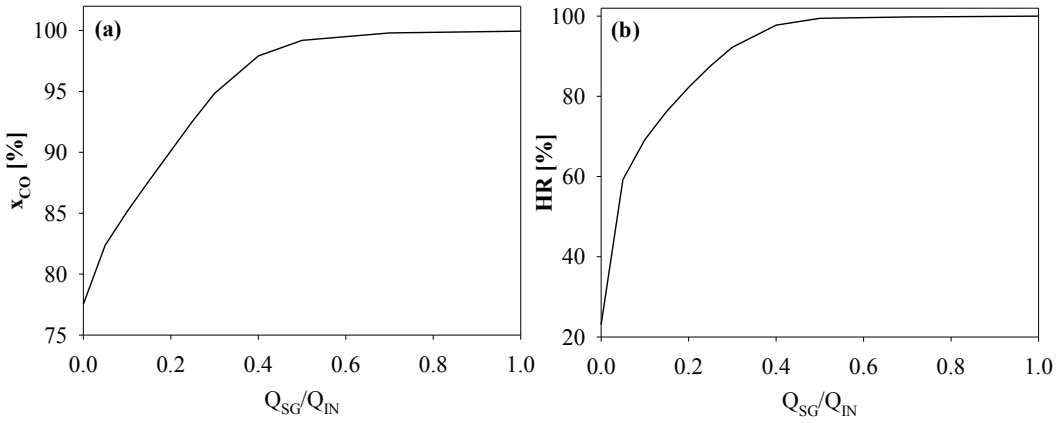

Figure 6.16 CO conversion x_{CO} (a) and hydrogen recovery HR (b) as a function of pressure sweep gas to inlet flow rate ratio Q_{SG}/Q_{IN}. Operating conditions: P = 3 atm, v = 0.025 m/s, L = 10 cm, δ = 30 μm. ATR case.

As regards reactor sizing, the volume required to produce 1 kW of electric energy in the case of ATR in the optimum conditions (P = 3 atm, Q_{SG}/Q_{IN} = 0.289) is equal to 1.8 lt for v = 0.025 m/s and δ = 30 μm (2.6 lt with the permeate side volume), therefore the reaction volume is reduced with respect to the conventional CO clean-up section in the ATR case.

6.3 Consideration on sizing of membrane WGS reactor

In order to compare the Mathematica results with the AspenPlus results in the case of the membrane reactor, some considerations must be done; indeed, the comparison of the membrane reactors modeled with Mathematica and with AspenPlus showed that there is no agreement between them.
This is due to the fact that the model developed in AspenPlus does not take into account the heat exchange between the reactive mixture and the mixture on the permeate side of the membrane, but it considers only the temperature variation of the reactive mixture related to the enthalpy of reaction and to the enthalpy of the hydrogen that permeates.

In order to understand the differences between the detailed model and the staged model employed in AspenPlus, a detailed comparison is reported.

6.3.1 Isothermal reactor model

The first comparison between Mathematica and AspenPlus was made with and isothermal model and without sweep gas. The comparison was made considering the ATR case. The reactor length was fixed at 10 cm and the fluid velocity at 0.025 m/s (conditions that guarantee high residence times inside the reactor).

In order to compare the data of the Mathematica model with the AspenPlus model, Table 6.8 reports the results obtained with AspenPlus in the isothermal case, for different pressure values; reactor performance are reported in terms of CO conversion x_{CO}, hydrogen recovery HR and quantity of hydrogen produced with respect to the total flowrate that enters in the reactor, $Q_{H2,P}/Q_{IN}$. Table 6.9

reports simulation result obtained with Mathematica in the isothermal case, for δ = 10 μm.

It is possible to observe that there is good agreement between the models, confirming that the membrane reactor approaches to equilibrium conditions, if the flowrate is enough low and if a thin membrane is employed.

P	**3**	**5**	**10**	**15**
HR	26.6	63.2	71.0	88.7
$Q_{H2,P}/Q_{IN}$	0.108	0.256	0.329	0.344
x_{CO}	86.7	92.9	93.4	97.8

Table 6.8 Simulation results with AspenPlus. Isothermal model, no sweep gas

P	**3**	**5**	**10**	**15**
HR	26.3	63.7	83.3	88.9
$Q_{H2,P}/Q_{IN}$	0.106	0.26	0.335	0.335
x_{CO}	85.7	92.4	96.7	98.0

Table 6.9 Simulation results with Mathematica. L= 10 cm, v = 0.025 m/s, δ = 10 μm, Q_{SG}/Q_{IN} = 0. Isothermal model.

As regards the sweep gas addition, good agreement between Mathematica and AspenPlus was observed at low velocities and low membrane thickness, for all the sweep gas to inlet flowrate ratio (Q_{SG}/Q_{IN}) investigated. The summary of the comparison is reported in Table 6.10 (simulation results with AspenPlus) and in Table 6.11 (simulation results with Mathematica), for two different values of Q_{SG}/Q_{IN} and for P = 3 atm.

Q_{SG}/Q_{IN}	**0.015**	**0.15**
HR	60.4	96.2
$Q_{H2,P}/Q_{IN}$	0.247	0.400
x_{CO}	90.4	98.1

Table 6.10 Simulation results with AspenPlus. Isothermal model, P = 3 atm

Q_{SG}/Q_{IN}	**0.015**	**0.15**
HR	60.9	93.2
$Q_{H2,P}/Q_{IN}$	0.250	0.412
x_{CO}	87.8	94.9

Table 6.11 Simulation results with Mathematica. L = 10 cm, v = 0.025 m/s, δ = 10 μm. Isothermal model, P = 3 atm.

6.3.2 Non-isothermal reactor model

The non isothermal operation was first modeled in case of operation without sweep gas.

The model considered to make the comparison with AspenPlus was the pseudo-homogeneous one, since the Mear's Criterion allowed to verify that the gas to solid phase transport resistance was negligible, both in the mass species balances and in the energy balance. Therefore, the mass species balances will contain the reaction term in place of the gas to solid phase transport term. As regards the energy balance, at first the following equation was considered to make the comparison:

$$\varepsilon \cdot \rho_g \cdot C_p + (1-\varepsilon) \cdot \rho_S \cdot C_{p,S} \cdot \frac{\partial T_g}{\partial t} = -v \cdot C_p \frac{\partial (v \cdot \rho_g \cdot T_g)}{\partial z} +$$
$$- (1-\varepsilon) \cdot \rho_S \cdot \eta \cdot r \cdot \Delta H - \frac{\pi M_{H2} \cdot \pi \cdot (d_i + 2\delta)}{A} \cdot J_{H2} \cdot C_{P,H2} \cdot (T_g - T_{SG})$$

The terms contained in the equation are the convective term, the reaction term and the enthalpy variation associated to the permeation of hydrogen, therefore the dispersive term is not taken into account. The results obtained in AspenPlus and in Mathematica are reported in Table 6.12. The results obtained with the Mathematica model show that the agreement with AspenPlus is achieved also in this case, when the conditions are high residence times inside the reactor and low resistance to hydrogen permeation thanks to low membrane thickness. Slight differences in the conversion value and in the hydrogen recovery are addressed to slight differences in the outlet temperature from the reactor.

Model	Aspen	Mathematica
HR	22.1	20.8
$Q_{H2,P}/Q_{IN}$	0.086	0.081
x_{CO}	70.8	67.8

Table 6.12 Simulation results at P = 3 atm, Q_{SG}/Q_{IN} = 0. Non-isothermal reactor model. Mathematica details: L = 10 cm, v = 0.025 m/s, δ = 10 µm

As regards the introduction of the energy balance in the model, by comparing the data obtained in AspenPlus (or in Mathematica) in the isothermal and in the adiabatic case (Table 6.8 vs. Table 6.12), it is possible to observe that the non-isothermal model gives little lower performances than the isothermal one. This is due to the fact that the CO shift reaction is adiabatic, therefore the temperature increase inside the reactor leads to a lowering of the CO conversion.

The introduction of the dispersive term in the energy balance makes the results change. In order to understand the effect of the axial dispersion term, Table 6.13 reports the results obtained in Mathematica when the axial dispersion term is introduced in the energy balance, for three different values of catalyst thermal conductivity k_s, at P = 3 atm. The first column refers to the model without the axial dispersion term.

k_s	**-**	**0.03**	**0.3**	**3.0**
HR	20.8	22.4	23.6	88.6
$Q_{H2,P}/Q_{IN}$	0.081	0.086	0.089	0.322
x_{CO}	67.8	73.3	77.8	89.8

Table 6.13 Simulation results with Mathematica. L = 10 cm, v = 0.025 m/s, δ = 10 µm, Q_{SG}/Q_{IN} = 0, P = 3. Non-isothermal reactor model

It is possible to observe that there is a dependence from the thermal conductivity of the catalyst and that a difference is observed when dispersion is introduced in the model, in particular in the CO conversion value.

The introduction of the dispersion term, indeed, leads to a spread of the heat released by the reaction, with a lowering of the temperature reached in the reactor; this temperature difference is the cause of the difference in the CO conversion and hydrogen recovery. It is worth noting that a decrease of the temperature inside the reactor has got a negative effect on HR, since the hydrogen permeability increases with temperature, therefore this factor influences the HR values.

The temperature profiles in the reactor evaluated without considering the dispersive heat transfer term and considering the dispersive heat transfer term with a thermal conductivity of the catalyst of 0.3 W/m·K are reported in Figure 6.17.

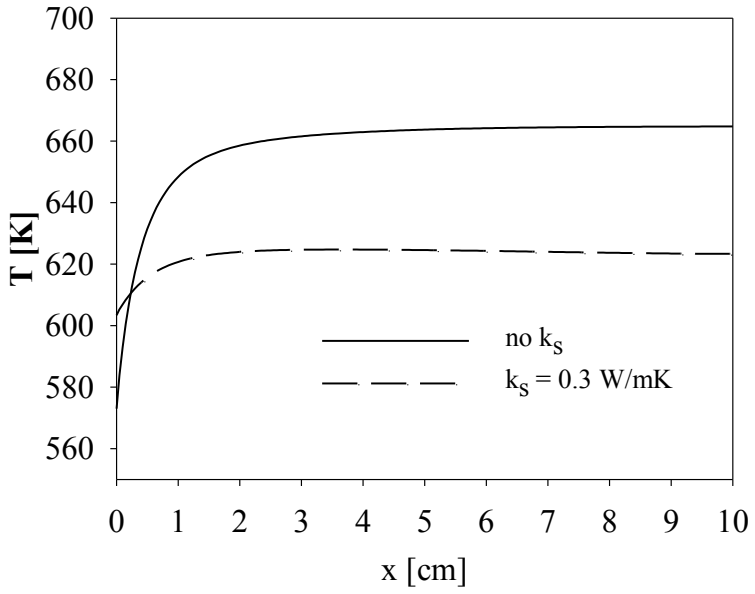

Figure 6.17 Temperature profile along reactor axis without the axial dispersive term (continuous line) and with the dispersive term (dotted line). P = 3 atm, L = 10 cm, v = 0.025 m/s, δ = 10 μm, Q_{SG}/Q_{IN} = 0. Non-isothermal model

The temperature profile is lower when the axial dispersion term is introduced in the model, leading to an increase in the CO conversion with respect to the model without axial dispersion term.

When the sweep gas is added in the system, the considerations made on the axial dispersion term are substantially the same as reported for the model without sweep gas. In addition, it should be said that the heat balance will foresee a term

of heat exchange with the permeate side of the membrane. This term is not considered in the AspenPlus model, since the configuration that simulates the membrane reactor does not take into account an exchange surface between the two zones of the reactor, but the separation is simulated by means of an external separator. Therefore, the temperature variation is associated to the loss of entalphy related to the hydrogen that permeates the membrane. This will cause differences in the reaction side temperature, with consequent differences in the reactor performance that, as reported above, are influenced by the temperature level inside the reactor. Table 6.14 reports the results of the simulation at P = 5 atm, $Q_{SG}/Q_{IN} = 0.015$ obtained with four different non-isothermal models:

a) AspenPlus model.
b) Mathematica model, no axial dispersion term, no heat exchange with permeate side of the membrane.
c) Mathematica model, no axial dispersion term, introduction of the heat exchange term with permeate side of the membrane ($U_M = 2.4$ W/m^2·K).
d) Mathematica model, introduction of the axial dispersion term (with k_S = 0.3 W/m·K) and of the heat exchange term with permeate side of the membrane ($U_M = 2.4$ W/m^2·K).

The simulation in Mathematica are performed always considering L = 10 cm, v = 0.025 m/s and δ = 10 μm. It is possible to observe that the Mathematica model that does not consider the heat exchange between the retentate and the permeate side (Model b) gives different results with respect to the AspenPlus model (Model a), mainly due to an increase in the temperature inside the reactor. The model that takes into account the heat exchange term (Model c), instead, gives results close to the Model a, thanks to a best fitting of the temperature profile inside the reactor.

The introduction of the axial dispersion term (Model d) will cause a spread of the temperature profile with a lowering of the thermal level inside the reactor, causing an increase of the CO conversion; the hydrogen recovery, instead is similar in all cases. The same comparison was performed at a higher sweep

gas to inlet flowrate ratio, $Q_{SG}/Q_{IN} = 0.15$, and the results are reported in Table 6.15.

Model	(a)	(b)	(c)	(d)
HR	82.8	83.3	83.4	82.7
$\mathbf{Q_{H2,P}/Q_{IN}}$	0.331	0.329	0.330	0.333
$\mathbf{x_{CO}}$	87.2	85.7	87.3	95.8
$\mathbf{T_{g,OUT}}$	402.5	425.6	409.8	316.8
$\mathbf{T_{SG,OUT}}$	378.2	333.4	334.5	300.8

Table 6.14 Simulation results. P = 5 atm, $Q_{SG}/Q_{IN} = 0.015$. Non-isothermal model

Model	(a)	(b)	(c)	(d)
HR	99.4	99.9	99.9	99.9
$\mathbf{Q_{H2,P}/Q_{IN}}$	0.407	0.409	0.409	0.410
$\mathbf{x_{CO}}$	98.7	99.9	99.9	99.9
$\mathbf{T_{g,OUT}}$	421.6	406.4	390.6	314.9
$\mathbf{T_{SG,OUT}}$	358.6	301.1	306.2	301.1

Table 6.15 Simulation results. P = 5 atm, $Q_{SG}/Q_{IN} = 0.15$. Non-isothermal model.

The reactor performance when a higher sweep gas flowrate is sent on the permeate side of the membrane are clearly better. It is possible to observe that the high hydrogen separation driving force due to the high Q_{SG}/Q_{IN} allows to obtain basically the same results in all models, unless the temperature values are different. Indeed, as expected, if the heat exchange term is introduced in the model (Model c and d), the temperature on the retentate side is lower than the one predicted in the AspenPlus model (Model a) and in the model without the heat exchange term (Model b).

Conclusions

The Ph.D. Research Program was focused on hydrogen production for energy generation on small scale in PEM fuel cell.

PEM fuel cells fed with hydrogen are the most promising device for decentralized energy production, both in stationary and automotive field, thanks to high compactness and good efficiency, obtained with a high purity hydrogen feed at the anode. Hydrogen, though, is not a primary source, but it is substantially an energy carrier, that needs to be produced from other fuels. Hydrogen production on industrial scale is a well known process, generally based on the Steam Reforming of light hydrocarbons or on Partial Oxidation of higher molecular weight hydrocarbons. Since hydrogen distribution from industrial plants to small scale users meets some limitations related to difficulties in hydrogen storage and transport, research is oriented toward the development of decentralized hydrogen production units, generally named as fuel processors, installed nearby the small scale user.

In literature, generally two kinds of fuel processor are reported: a conventional one, based on traditional fixed bed reactors, and an innovative one, based on membrane reactors that allow to produce pure hydrogen by employing high selective hydrogen membranes. The efficiency of the fuel processor – PEM fuel cell system strongly depends on system configuration, on the process employed in the reforming reactor (endothermic or autothermal process), on the heat integration inside the fuel processor and between the fuel processor and the fuel cell; therefore, in this work a system analysis of the most promising configurations was performed, in order to identify the best solution for energy generation with a fuel processor - PEM fuel cell system.

Since the application of these systems is foreseen on small scale, an important characteristic that must me associated to the high efficiency is the compactness. Therefore, a mathematical model for fixed bed reactors was developed in order to size and compare conventional fixed bed reactor and membrane catalytic reactors. The main results achieved during the three years of Ph.D. are reported in the following paragraph.

Literature Analysis

The first year of the Ph.D. was dedicated to literature analysis and the aim of the study was to achieve a valid background on PEM fuel cell based systems. The main information recovered during the study are the following:

- ✓ The analysis of fuel processor – PEM fuel cell systems is widely reported in literature, since various configurations are possible for the coupling with the PEM fuel cell; both the configuration chosen for the fuel processor and the operating parameters have an impact on the energy efficiency of the system. Moreover, the application on small scale requires not only high energy efficiency, but also a high compactness
- ✓ Fuel processors are generally based on Steam Reforming (SR) or on Autothermal Reforming (ATR) and the fuel for hydrogen generation can be a fossil fuel (methane/liquid) or a renewable source (methanol/ethanol)
- ✓ Membrane reactors for pure hydrogen production result to be really promising for the application in the fuel processor. The highly selective hydrogen membrane allows to produce pure hydrogen that can be fed directly to the PEM fuel cell, without the production of a purge gas stream at the anode (Anode Off-Gas) that is generally produced when the stream fed to the anode is not 100% H_2 pure.
- ✓ The membrane reactor can be either a membrane reforming reactor or a membrane water gas shift reactor placed downstream a traditional reforming reactor. The first configuration guarantees a high fuel processor compactness in terms of number of units, since the fuel processor would be constituted only by a reforming reactor, unless the auxiliary units; the

second configuration, although less compact, allows to work with the membrane in a middle temperature range, typical of the water gas shift reaction, guaranteeing a better thermal stability of the membrane.

- ✓ A crucial issue in the maximization of the energy efficiency regards the heat integration in the system; the reactors inside the fuel processors work at different temperatures, therefore there are streams that need to be cooled and others that need to be heated; in the membrane reactors a sweep gas can be employed to promote hydrogen permeation through the membrane, therefore an evaporator for sweep gas production from water must be foreseen in the system; moreover, if the reforming process is endothermic, the heat for sustaining the reforming reactions must be taken into account. This means that it is really important to recover heat in the various sections of the plant, trying to operate with the most compact configuration, that is reducing the number of heat exchangers in the system, and also to recover the enthalpy of the Anode Off-Gas leaving the cell or of the retentate stream leaving the membrane reactor in an after-burner, in order to reduce or to avoid the feeding of additional fuel to the burner to sustain the process, with an impact on the system efficiency.

Thermodynamic Analysis of Fuel Processor – PEM Fuel Cell Systems

On the basis of the analysis performed during the first year of the Ph.D., the second year was dedicated to the thermodynamic analysis of fuel processor – PEM fuel cell systems for maximization of energy efficiency.

In particular, conventional fuel processors and innovative fuel processors were investigated. Conventional fuel processors are constituted by a reforming unit (SR/ATR) followed by a conventional CO clean-up section (two WGS reactors and a CO preferential oxidation reactor); innovative fuel processors are based on membrane reactors and can be constituted by a membrane reforming reactor (SR/ATR) or by a traditional reforming reactor (SR/ATR) followed by a membrane WGS reactor.

The analysis performed with methane as fuel allowed to understand that:

- ✓ Fuel processors – PEM fuel cell systems can reach high efficiency levels (40-50%), far higher than what is achieved in traditional energy systems
- ✓ Systems based on SR are generally more efficient than ATR based systems for the higher heat recovery
- ✓ Although innovative SR based fuel processor are more efficient than the ATR ones, the introduction of the membrane in the system allows to reduce the efficiency gap between SR and ATR systems; in the conventional case, the ATR system efficiency was around 20% lower than the SR case, whereas in the innovative systems the difference between ATR and SR was reduced to less than 10%
- ✓ In the case of SR, the employment of membrane reactors allows to increase the energy efficiency of the system if pressure is employed to increase the hydrogen separation driving force through the membrane, more than the sweep gas
- ✓ In the case of ATR, the employment of membrane reactors allows to increase the energy efficiency of the system only if a sweep gas stream is sent counter-currently to the reacting mixture in the membrane reactor
- ✓ If renewable sources are employed as fuel for hydrogen generation, the results can vary on the basis of the fuel. For example, when pure ethanol is employed as fuel, the results are substantially the same of what is achieved with methane, whereas the employment of crude ethanol (a mixture of ethanol and water with a water to ethanol ratio of 10) leads to a strong decrease of system efficiency for the high water content in the inlet fuel

Mathematical Model of fixed bed reactors for System Sizing

After system optimization, the Ph.D. was dedicated to the sizing of the reactors in order to quantify system compactness. The first step was model development on the basis of literature data, followed by model validation both for the traditional and the membrane reactor; the results achieved with the model showed that:

- ✓ The mathematical model of traditional and membrane reactors allows to simulate the performance of reactors in conditions that are far from the equilibrium

- ✓ The conventional CO clean-up section has got a reaction volume of 1.3 lt in the SR case and of 2.4 lt in the ATR case for the production of 1 kW of electric energy. This volume is referred only to reactors and does not take into account the encumbrance of the heat exchangers placed between each reactor that constitutes the CO clean-up section.
- ✓ The introduction of the membrane in the WGS reactor allows to reduce the encumbrance of the CO clean-up section. In particular, as reported in the SR case, the volume strictly depends on the effectiveness of hydrogen separation and it can be reduces if thin membrane are employed. In the case of membrane thickness of 30 μm, the reaction volume is equal to 1.1 lt for producing 1 kW of electric energy. The volume of the reactor rises up to 1.5 lt if the permeation side volume is considered. However, the encumbrance of the CO clean-up section is less than the conventional case, since it works with two heat exchangers less. When an ultrathin membrane is employed (10 μm), the volume lowers to 0.75 lt (including the permeation side).
- ✓ In the modeling of the membrane reactors, it was found that, differently from the conventional reactors, the CO conversion depends not only on the GHSV, but also on the fluid velocity inside the reactors. Different plateau values in the CO conversion were observed with varying the inlet fluid velocity.
- ✓ By comparing the results of Mathematica with the results obtained in AspenPlus, differences from the thermodynamic values are achieved if the axial dispersion term is introduced in the model, particularly at low flowrates.
- ✓ In the membrane reactor case, differences between the two models are observed when the sweep gas is introduced in the system, since the AspenPlus model does not take into account the convective heat exchange term between the retentate and the permeate side of the membrane.

References

[1] C. Song, Fuel processing for low-temperature and high-temperature fuel cells. Challenges and opportunities for sustainable development in the 21st century, Catalysis Today, 77 (2002) 17–49

[2] D.L. Trimm, Catalysts for the control of coking during steam reforming, Catalysis Today, 49 (1999) 3-10

[3] Y.Matsumura., T.Nakamori, Steam reforming of methane over nickel catalysts at low reaction temperature, Applied Catalysis A: General, 258 (2004) 107–14

[4] J.H. Ryu, K.Y. Lee, H. La, H.J. Kim, J.I. Yang, H. Jung, Ni catalyst wash-coated on metal monolith with enhanced heat-transfer capability for steam reforming, Journal of Power Sources 171 (2007) 499–505

[5] A.F. Ghenciu, Review of fuel processing catalysts for hydrogen production in PEM fuel cell systems, Current Opinion in Solid State and Materials Science, 6 (2002) 389–399

[6] Q.H. Zhang, Y. Li, B.Q. Xu, Reforming of methane and coalbed methane over nanocomposite Ni/ZrO_2 catalyst, Catalysis Today, 98 (2004) 601-605

[7] J.G. Seo, M.H. Youn, K.M. Cho, S. Park, I.K. Song, Hydrogen production by steam reforming of liquefied natural gas over a nickel catalyst supported on mesoporous alumina xerogel, Journal of Power Sources, 173 (2007) 943-949

[8] MES. Hegarty, AM. O'Connor, JRH. Ross, Syngas production from natural gas using ZrO_2-supported metals, Catalysis Today (1998) 225-232

[9] Y.S. Seo, A. Shirley, S.T. Kolaczkowski, Evaluation of thermodynamically favourable operating condition for production of hydrogen in three different reforming technologies, J. Power Sources, 108 (2002) 213-225

[10] M. Bizzi, G. Saracco, R. Schwiedernoch, O. Deutschmann, Modeling the Partial Oxidation of Methane in a Fixed Bed with Detailed Chemistry, AIChE Journal, 50 (2004) 1289-99

[11] I. Tavazzi, M. Maestri, A. Beretta, G. Groppi, E. Tronconi, Steady-State and Transient Analysis of a CH_4-Catalytic Partial Oxidation Reformer, AIChE Journal, 52 (2006) 3234-3244

[12] L.D. Schmidt, S.S. Bharadwaj, Catalytic partial oxidation of natural gas to syngas, Fuel process technology, 42 (1995) 109-127

[13] L. Ma, D. Trimm, Alternative catalyst bed configurations for the autothermic conversion of methane to hydrogen, Applied Catalyst A: General, 136 (1996) 265-273

[14] S. Fukada, N. Nakamura, Effects of temperature, oxygen-to-methane molar ratio and superficial gas velocity on partial oxidation of methane for hydrogen production, International Journal of Hydrogen Energy, 29 (2004) 619–625

[15] M. Bizzi, L. Basini, G. Saracco, V. Specchia, Short contact time catalytic partial oxidation of methane: analysis of transport phenomena effects, Chemical Engineering Journal, 90 (2002) 97–106

[16] A.C.J. Dias, J.M. Assaf, the advantages of air addition on the methane steam reforming over Ni/Al_2O_3, Journal of Power Sources, 137 (2004) 264–268

[17] A.M. De Grotte, G.F. Froment, Simulation of the catalytic partial oxidation of methane to syngas, Applied Catalysis A: General, 138 (1996) 245-264

[18] J. Zhu, J.G. van Ommen, L. Lefferts, Reaction scheme of partial oxidation of methane to synthesis gas over yttrium-stabilized zirconia, Journal of Catalysis, 225 (2004) 388–397

[19] P. Hurtado, S. Ordónez, H. Sastre, F.V. Dıez, Development of a kinetic model for the oxidation of methane over Pd/Al2O3 at dry and wet conditions, Applied Catalysis B: Environmental, 51 (2004) 229–238

[20] Y. H. Hu, E. Ruckenstein, Transient Kinetic Studies of Partial Oxidation of CH4, Journal of Catalysis, 158 (1996) 260–266

[21] C. Elmasides, X.E. Verykios, Mechanistic Study of Partial Oxidation of Methane to Synthesis Gas over Modified Ru/TiO2 Catalyst, Journal of Catalysis, 203 (2001) 477– 486

[22] Q.G. Yan , T.H. Wub, W.Z. Weng, H. Toghiani , R.K. Toghiani, H.L. Wan, C.U. Pittman Jr, Partial oxidation of methane to H2 and CO over Rh/SiO2 and Ru/SiO2 catalysts, Journal of Catalysis, 226 (2004) 247–259

[23] W.Z. Weng, C.R. Luo, J.J. Huang, Y.Y. Liao, H.L. Wan, Comparative study on the mechanisms of partial oxidation of methane to syngas over rhodium supported on SiO2 and α-Al2O3, Topics in Catalysis, 22 (2003)

[24] W.Z. Weng, Q.G. Yan, C.R. Luo, Y.Y. Liao, H.L. Wan, The concentration of oxygen species over SiO2-supported Rh and Ru catalysts and its relationship with the mechanism of partial oxidation of methane to synthesis gas, Catalysis Letters, 74 (2001)

[25] Q.G. Ya, T.H. Wu, W.Z. Weng, H. Toghiani, R.K. Toghiani, H.L. Wan, C.U. Pittman Jr, Partial oxidation of methane to H2 and CO over Rh/SiO2 and Ru/SiO2 catalysts, Journal of Catalysis, 226 (2004) 247-259

[26] G. Veser, J. Frauhammer, U. Friedle, Syngas formation by direct oxidation of methane Reaction mechanisms and new reactor concepts, Catalysis Today, 61 (2000) 55–64

[27] B. Li, R. Watanabe, K. Maruyama, K. Kunimori, K. Tomishige, Thermographical observation of catalyst bed temperature in oxidative steam reforming of methane over Ni supported on α-alumina granules: Effect of Ni precursors, Catalysis Today 104 (2005) 7-17.

[28] B. Li, K. Maruyama, M. Nurunnabi, K. Kunimori, K. Tomishige, Temperature profile of alumina-supported noble metal catalyst in autothermal reforming of methane, Applied Catalysis A: General 275 (2004) 157-172.

[29] D.L. Hoang, S.H. Chan, O.L. Ding, Hydrogen production for fuel cells by autothermal reforming of methane over sulphide nickel catalyst on a gamma alumina support, Journal of Power Sources 159 (2006) 1248-1257.

[30] D.L. Hoang, S.H. Chan, Modeling of a catalytic autothermal methane reformer for fuel cell applications, Applied Catalysis A: General, 268 (2004) 207-216.

[31] S.H. Chan, H.M. Wang, Thermodynamic analysis of natural-gas fuel processing for fuel cell applications, International Journal of Hydrogen Energy, 25 (2000) 441-449.

[32] D.L. Hoang, S.H. Chan, Experimental investigation on the effect of natural gas composition on performance of autothermal reforming, International Journal of Hydrogen Energy, 32 (2007) 548-556.

[33] B.F. Hagh, Optimization of autothermal reactor for maximum hydrogen production, International Journal of Hydrogen Energy, 28 (2003) 1369-1377.

[34] D.P.J. Barz, U.K. Tragner, V.M. Schmidt, M. Koschowitz, Thermodynamics of hydrogen generation from methane for domestic polymer electrolyte, Fuel Cell, 3 (2003) 199-207.

[35] J.A.C. Dias, J.M. Assaf, Autoreduction of promoted Ni/ γ-Al_2O_3 during autothermal reforming of methane. Journal of Power Sources, 139 (2005) 176-181.

[36] T. Utaka, T. Okanishi, T. Takeguchi, R. Kikuchi, K. Eguchi, Water gas shift reaction of reformed fuel over supported Ru catalysts, Applied Catalysis A: General, 245 (2003) 343–351

[37] N.A. Baronskaya, T.P. Minyukova, A.G. Sipatrov, M.P. Demeshkina, A.A. Khassin, S.V. Dimov, S.P. Kozlov, V.V. Kuznetsov, V.Y. Terentiev, A.P. Khristolyubov, T.M. Yurieva, Compact reactor for water gas shift reaction over thermal-conducting catalysts, Chemical Engineering Journal, 2007; 134: 195–9

[38] J. Sun, J. DesJardins, J. Buglass, K. Liu, Noble metal water gas shift catalysis: Kinetics study and reactor design, International Journal of Hydrogen Energy, 2005; 30: 1259-64

[39] P. Giunta, N. Amadeo, M. Laborde, Simulation of a low temperature water gas shift reactor using the heterogeneous model/application to a pem fuel cell, Journal of Power Sources, 2006; 156: 489–96

[40] J. Pasel, R.C. Samsun, D. Schmitt, R. Peters, D. Stolten, Test of a water–gas-shift reactor on a 3kWe-scale—design points for high- and low-temperature shift reaction, Journal of Power Sources, 2005; 152: 189–95

[41] T.R. de Souza, S.M. Brito, H.M. Andrade, Zeolite catalysts for the water gas shift reaction, Applied Catalysis A: General, 1999; 178: 7-15

[42] M. Echigo, T. Tabata, Development of novel Ru catalyst of preferential CO oxidation for residential polymer electrolyte fuel cell systems, Catalysis Today, 2004; 90: 269–75

[43] M. Echigo, T. Tabata, A study of CO removal on an activated Ru catalyst for polymer electrolyte fuel cell applications, Applied Catalysis A: General, 2003; 251: 157–66

[44] M. Echigo, N. Shinke, S. Takami, S. Higashiguchi, K. Hirai, T. Tabata, Development of residential PEFC cogeneration systems: Ru catalyst for CO preferential oxidation in reformed gas, Catalysis Today, 2003; 84: 209–15

[45] C.D. Dudfield, R. Chen, P.L. Adcock, A carbon monoxide PROX reactor for PEM fuel cell automotive application, International Journal of Hydrogen Energy, 2001; 26: 763–75

[46] E.-Y. Ko, E.D. Park, K.W. Seo, H.C. Lee, D. Lee, S. Kim, A comparative study of catalysts for the preferential CO oxidation in excess hydrogen, Catalysis Today, 2006; 116: 377–83

[47] M. Watanabe, H. Uchida, K. Ohkubo, H. Igarashi, Hydrogen purification for fuel cells: selective oxidation of carbon monoxide on Pt–Fe/zeolite catalysts, Applied Catalysis B: Environmental, 2003; 46: 595–600

[48] F. Mariño, C. Descorme, D. Duprez, Noble metal catalysts for the preferential oxidation of carbon monoxide in the presence of hydrogen (PROX), Applied Catalysis B: Environmental, 2004; 54: 59–66

[49] D.J. Suh, C. Kwak, J.-H. Kim, S.M. Kwon, T.-J. Park, Removal of carbon monoxide from hydrogen-rich fuels by selective low-temperature oxidation over base metal added platinum catalysts, Journal of Power Sources, 2005; 142: 70–4

[50] B. Atalik, D. Uner, Structure sensitivity of selective CO oxidation over Pt/γ-Al_2O_3, Journal of Catalysis, 2006; 241: 268–75

[51] B. Rohland, V. Plzak, The PEMFC-integrated CO oxidation; a novel method of simplifying the fuel cell plant, Journal of Power Sources, 1999; 84: 183–6

[52] Shu, J. Grandjean, BPA. van Neste, A. Kaliaguine, S. (1991). Catalytic palladium-based membrane reactors: a review, Canadian Journal of Chemical Engineering, 69, 1036-1060, ISSN 0008-4034

[53] G.Q. Lu, J.C. Diniz da Costa, M. Duke, S. Giessler, R. Socolow, R.H. Williams, T. Kreutz, Inorganic membranes for hydrogen production and purification: A critical review and perspective, Journal of Colloid and Interface Science, 2007; 589-603

[54] A. Darling, Platinum Met. Rev. 2 (1958) 16–22

[55] V.M. Gryaznov, Platinum Met. Rev. 30 (1986) 68–72

[56] V. Mordkovich, Y. Baichtock,M. Sosna, Platinum Met. Rev. 36 (1992) 90

[57] N. Itoh, AIChE J. 33 (1987) 1576–1578

[58] R. Govind, D. Atnoor, Ind. Eng. Chem. Res. 30 (1991) 591–594

[59] E. Gobina, R. Hughes, Journal of Membrane Science, 90 (1994) 11–19

[60] Z.D. Ziaka, R.G. Minet, T.T. Tsotsis, J. Membr. Sci. 77 (1993) 221–232

[61] R.E. Buxbaum, T.L. Marker, Journal of Membrane Science, 85 (1993) 29–38

[62] S. Yam, H. Maeda, K. Kusakabe, S. Morooka, Ind. Eng. Chem. Res. 33 (1994) 616–22

[63] Z.Y. Li, H. Maeda, K. Kusakabe, S. Morooka, H. Anzai, S. Akiyama, Journal of Membrane Science, 78 (1993) 247–254

[64] A. Basile, G. Chiappetta, S. Tosti, V. Violante, Experimental and simulation of both Pd and Pd/Ag for a water gas shift membrane reactor, Separation and purification technology, 25 (2001) 549-571

[65] S. Uemiya, T. Matsuda, E. Kikuchi, J. Membr. Sci. 56 (1991) 315–325

[66] J.N. Armor, J. Membr. Sci. 147 (1998) 217–233

[67] M.D. Dolan, N.C. Dave, A.Y. Ilyushechkin, L.D. Morpeth, K.G. McLennan, J. Membr. Sci. 285 (2006) 30–55

[68] A. Li, W. Liang, R. Hughes, J. Membr. Sci. 165 (2000) 135–141

[69] J.N. Armor, Catal. Today 25 (1995) 199–207

[70] A.F.Y. Al-Shammary, I.T. Caga, J.M.Winterbottom, A.Y. Tata, I.R. Harris, J. Chem. Technol. Biotechnol. 52 (1991) 571–585

[71] H.S. Chu, F. Tsau, Y.Y. Yan, K.L. Hsueh, F.L. Chen, The development of a small PEMFC combined heat and power system, Journal of Power Sources, 176 (2008) 499–514

[72] M. Dokupil, C. Spitta, J. Mathiak, P. Beckhaus, A. Heinzel, Compact propane fuel processor for auxiliary power unit application, Journal of Power Sources, 157 (2006) 906–913

[73] M. Echigo, N. Shinke, S. Takami, T. Tabata, Performance of a natural gas fuel processor for residential PEFC system using a novel CO preferential oxidation catalyst, Journal of Power Sources, 132 (2004) 29–35

[74] D. Lee, H.C. Lee, K.H. Lee, S. Kim, A compact and highly efficient natural gas fuel processor for 1-kW residential polymer electrolyte membrane fuel cells, Journal of Power Sources, 165 (2007) 337–341

[75] J. Mathiak, A. Heinzel, J. Roes, Th. Kalk, H. Kraus, H. Brandt, Coupling of a 2.5 kW steam reformer with a 1 kWel PEM fuel cell, Journal of Power Sources, 131 (2004) 112–119

[76] A. Docter, A. Lamm, Gasoline fuel cell systems, Journal of Power Sources, 84 (1999) 194–200

[77] S. Ahmed, M. Krumpelt, Hydrogen from hydrocarbon fuels for fuel cells, International Journal of Hydrogen Energy, 26 (2001) 291–300

[78] A. Ersoz, H. Olgun, S. Ozdogan, Reforming options for hydrogen production from fossil fuels for PEM fuel cells. Journal of Power Sources, 154 (2006) 67-73

[79] W.G. Colella, Design considerations for effective control of an afterburner sub-system in a combined heat and power (CHP) fuel cell system (FCS), Journal of Power Sources, 118 (2003) 118–128

[80] G. Gigliucci, L. Petruzzi, E. Cerelli, A. Garzisi, A. La Mendola, Demonstration of a residential CHP system based on PEM fuel cells, Journal of Power Sources, 131 (2004) 62–68

[81] C.E. Hubert, P. Achard, R. Metkemeijer, Study of a small heat and power PEM fuel cell system generator, Journal of Power Sources, 156 (2006) 64–70

[82] J.B. Pearlman, A. Bhargav, E.B. Shields, G.S. Jackso, P.L. Hearl, Modeling efficiency and water balance in PEM fuel cell systems with liquid fuel processing and hydrogen membranes, Journal of Power Sources 185 (2008) 1056-1065

[83] R. Lattner, M.P. Harold, Comparison of methanol-based fuel processors for PEM fuel cell systems, International Journal of Hydrogen Energy, 29 (2004) 393 417

[84] G. Manzolini, S. Tosti, Hydrogen production from ethanol steam reforming: energy efficiency analysis of traditional and membrane processes, International Journal of Hydrogen Energy, 33 (2008) 5571-5582

[85] S. Campanari, E. Macchi, G. Manzolini, Innovative membrane reformer for hydrogen production applied to PEM micro-cogeneration: Simulation model and thermodynamic analysis, International Journal of Hydrogen Energy, 33 (2008) 1361-1373

[86] M. Lyubovsky, D. Walsh, Reforming system for co-generation of hydrogen and mechanical work, Journal of Power Sources, 157 (2006) 430-437

[87] M. Sjardin, K.J. Damen, A.P.C. Faaij, Techno-economic prospects of small-scale membrane reactors in a future hydrogen-fuelled transportation sector, Energy, 31 (2006) 2187–2219

[88] G.F. Froment, Chemical Reaction Engineering, Advances in Chemistry Series, Am. Chem. Soc. 109 (1972)

[89] P. Andrigo, R. Bagatin, G. Pagani, Fixed bed reactors, Catalysis Today, 52 (1999) 197-221

[90] A.I. Anastasov, A study of the influence of the operating parameters on the temperature of the hot spot in a fixed bed reactor, Chemical Engineering Journal, 86 (2002) 287–297

[91] S.H. Chan, D.L. Hoang, O.L. Ding, Transient performance of an autothermal reformer - A 2-D modeling approach, International Journal of Heat and Mass Transfer 48 (2005) 4205–4214

[92] W. Yu, T. Ohmori, S. Kataoka, T. Yamamoto, A. Endo, M. Nakaiwa, N. Itoh, A comparative simulation study of methane steam reforming in a porous ceramic membrane reactor using nitrogen and steam as sweep gas, International Journal of Hydrogen Energy, 33 (2008) 685-692

[93] A. Kleinert, G. Grubert, X. Pan, C. Hamel, A. Seidel-Morgenstern, J. Caro, Compatibility of hydrogen transfer via Pd-membranes with the rates of heterogeneously catalysed steam reforming, Catalysis Today, 104 (2005) 267–273

[94] M.N. Pedernera, J. Pina, D.O. Borio, Kinetic evaluation of carbon formation in a membrane reactor for methane reforming, Chemical Engineering Journal, 134 (2007) 138–144

[95] F.A.N. Fernandes, A.B. Soares Jr, Methane steam reforming modeling in a palladium membrane reactor, Fuel, 85 (2006) 569–573

[96] G. Marigliano, G. Barbieri, E. Drioli, Effect of energy transport on a palladium-based membrane reactor for methane steam reforming process, Catalysis Today, 67 (2001) 85–99

[97] Y.M. Lin, S.L. Liu, C.H. Chuang, Y.T. Chu, Effect of incipient removal of hydrogen through palladium membrane on the conversion of methane steam reforming Experimental and modeling, Catalysis Today, 82 (2003) 127–139

[98] A. Bottino, A. Comite, G. Capannelli, R. Di Felice, P. Pinacci, Steam reforming of methane in equilibrium membrane reactors for integration in power cycles, Catalysis Today, 118 (2006) 214–222

[99] F. Gallucci, L. Paturzo, A. Basile, A simulation study of the steam reforming of methane in a dense tubular membrane reactor, International Journal of Hydrogen Energy, 29 (2004) 611 – 617

[100] A. Basile, L. Paturzo, F. Laganà, The partial oxidation of methane to syngas in a palladium membrane reactor: simulation and experimental studies, Catalysis Today, 67 (2001) 65–75

[101] M. De Falco, L. Di Paola, L. Marrelli, Heat transfer and hydrogen permeability in modelling industrial membrane reactors for methane steam

reforming, International Journal of Hydrogen Energy, 32 (2007) 2902 – 2913

[102] M. De Falco, L. Di Paola, L. Marrelli, P. Nardella, Simulation of large-scale membrane reformers by a two-dimensional model, Chemical Engineering Journal, 128 (2007) 115–125

[103] M. De Falco, Pd-based membrane steam reformers: A simulation study of reactor performance, International Journal of Hydrogen Energy, 33 (2008) 3036–3040

[104] Y. Choi, H.G. Stenger, Water gas shift reaction kinetics and reactor modeling for fuel cell grade hydrogen, Journal of Power Sources, 124 (2003) 432–439

[105] T.A. Adams II, P.I. Barton, A dynamic two-dimensional heterogeneous model for water gas shift reactors, International Journal of Hydrogen Energy, 34 (2009) 8877 – 8891

[106] A. Criscuoli, A. Basile, E. Drioli, An analysis of the performance of membrane reactors for the water–gas shift reaction using gas feed mixtures, Catalysis Today, 56 (2000) 53–64

[107] S. Tosti, L. Bettinali, V. Violante, Rolled thin Pd and Pd-Ag membranes for hydrogen separation and production, International Journal of Hydrogen Energy, 25 (2000) 319-325

[108] A. Basile, L. Paturzo, F. Gallucci, Co-current and counter-current modes for water gas shift membrane reactor, Catalysis Today, 82 (2003) 275–281

[109] A. Brunetti, A. Caravella, G. Barbieri, E. Drioli, Simulation study of water gas shift reaction in a membrane reactor, Journal of Membrane Science, 306 (2007) 329–340

[110] G. Chiappetta, G. Clarizia, E. Drioli, Theoretical analysis of the effect of catalyst mass distribution and operation parameters on the performance of a Pd-based membrane reactor for water–gas shift reaction, Chemical Engineering Journal, 136 (2008) 373–382

[111] M.E. Adrover, E. Lopez, D.O. Borio, M.N. Pedernera, Theoretical Study of a Membrane Reactor for the Water Gas Shift Reaction Under Nonisothermal Conditions, AIChE Journal, 55 (2009) 3206-3213

[112] Aspen Technology Inc. http://www.aspentech.com

[113] J.A. Francesconi, M.C. Mussati, R.O. Mato, P.A. Aguirre, Analysis of the Energy efficiency of a integrated ethanol processor for PEM fuel cell systems, Journal of Power Sources, 167 (2007) 151-161

[114] E.D. Doss, R. Kumar, R.K. Ahluwalia, M. Krumpelt. Fuel processors for automotive fuel cell systems: a parametric analysis, Journal of Power Sources, 102 (2001) 1-15

[115] G.M. Ratnamala, N. Shah, V. Mehta, P.V. Rao, Integrated Fuel Cell Processor for a 5-kW Proton-Exchange Membrane Fuel Cell, Ind. Eng. Chem. Res. 44 (2005) 1535-1541

[116] Y. Hou, M. Zhuang, G. Wan, The analysis for the efficiency properties of the fuel cell engine, Renewable Energy, 32 (2007) 1175–1186

[117] J. Rass-Hansen, R. Johansson, M. Moller, C.H. Christensen, Steam reforming of technical bio-ethanol for hydrogen production, International Journal of Hydrogen Energy, 33 (2008) 4547-4554

[118] M. Ni, D.Y.C. Leung, M.K.H. Leung, A review on reforming bio-ethanol for hydrogen production, International Journal of Hydrogen Energy, 32 (2007) 3238-3247

[119] G. Rabenstein, V. Hacker, Hydrogen for fuel cells from ethanol by steam-reforming, partial-oxidation and combined auto-thermal reforming: A thermodynamic analysis, Journal of Power Sources, 185 (2008) 1293-1304

[120] F. Soyal-Baltacıoglu, A.E. Aksoylu, Z.I. Onsan, Steam reforming of ethanol over Pt–Ni Catalysts, Catalysis Today, 138 (2008) 183–186

[121] A. Perna, Hydrogen from ethanol: Theoretical optimization of a PEMFC system integrated with a steam reforming processor, International Journal of Hydrogen Energy, 32 (2007) 1811-1819

[122] M. Benito , R. Padilla, J.L. Sanz, L. Daza, Thermodynamic analysis and performance of a 1kW bioethanol processor for a PEMFC operation, Journal of Power Sources, 169 (2007) 123-130

[123] F. Gallucci, A. Basile, Pd-Ag membrane reactor for steam reforming reactions: A comparison between different fuels, International Journal of Hydrogen Energy, 33 (2008) 1671-1687

[124] F. Gallucci, A. Basile, S. Tosti, A. Iulianelli, E. Drioli, Methanol and Ethanol steam reforming in membrane reactors: an experimental study, International Journal of Hydrogen Energy, 32 (2007) 1201-1210

[125] T. Ioannides, Thermodynamic analysis of ethanol processors for fuel cell applications, Journal of Power Sources, 92 (2001) 17-25

[126] P.V. Danckwerts, Continuous flow systems. Distribution of residence times. Chemical Engineering Science, 1 (1953) 1-13

[127] V. Hlavacek, H. Hofmann, Modeling of chemical reactors-XVII. Steady state heat and mass transfer in tubular reactors. Numerical investigation of multiplicity, Chemical Engineering Science, 25 (1970) 173-187

[128] V. Hlavacek, H. Hofmann, J. Vortuba, Modeling of chemical reactors-XXVII. Steady state axial heat and mass transfer in tubular reactors. Effect of different values of Peclet numbers on the region of multiplicity. Chemical Engineering Science, 28 (1973) 1897

[129] V. Hlavacek, J. Vortuba, Experimental study of multiple steady states in adiabatic catalytic systems. Chemical Reaction Engineering-II. Advances in chemistry series. American chemical society. Washington D.C. (1974) 545-558

[130] V. Hlavacek, J. Vortuba, Steady-state operation of fixed-bed reactors and monolithic structures. N.Y. (1977) 314

[131] G.F. Froment, K.B. Bischoff, Chemical Reaction Analysis and Design, John Wiley (1979)

[132] R.H. Perry, D.W. Green, Perry's Chemical Engineers Handbook, Seventh Edition McGraw-Hill (1997)

[133] B.E. Poling, J.M. Prausnitz, J.P. O'Connell, The Properties of Gases and Liquids, Fifth Edition, McGraw-Hill

[134] S. Ergun, Mass-transfer rate in packed columns. Its analogy to pressure loss. Chem. Eng. Progress., 48 (1952) 227-236

[135] R.E. Hicks, Ind. Eng. Chem. Fund., 9 (1970) 500

[136] D. Handley, P.J. Heggs, Trans. Instn. Chem. Engrs, 46 (1968) 251

[137] E.W. Thiele, Relation between catalytic activity and size of particle. Ind. Eng. Chem., 31 (1939) 916-920

[138] I.B. Zeldowitsch, Zhur. Fiz. Khim., 13 (1939) 163

[139] O. Levenspield, Chemical Reaction Engineering. JohnWiley & Sons, New York 1962.

[140] R. Aris, The mathematical theory of diffusion and reaction in permeable catalyst I. Clarendon Press. Oxford, 1975a

[141] R. Aris, The mathematical theory of diffusion and reaction in permeable catalyst II. Clarendon Press. Oxford, 1975b

[142] J. Xu, G.F. Froment, Aiche Journal, 35 (1989a) 88

[143] S. Fogler, Elements of chemical reaction engineering 2nd ed. Prentice Hall International Edictions: Englewood Clifs NJ, 1992.

[144] M.F. Edwards, J.F. Richardson, Gas dispersion in packed beds, Chemical Engineering Science, 23 (1968) 109-123

[145] S. Yagi, D. Kuni, Kagaku Kogaky 18 (1954) 576

[146] S. Yagi, D. Kuni, Aiche Journal, 3 (1957) 373

[147] S. Yagi, D. Kuni, Aiche Journal, 6 (1960) 97

[148] S. Yagi, D. Kuni, Aiche Journal, 6 (1960) 543

[149] J. Vortuba, V. Hlavacek, M. Marek, Chemical Engineering Science, 27 (1972) 1845-1851

[150] R. Krupiczka, Chemia Stosowana, 2B (1966) 183

[151] R. Krupiczka, Chim. Ind. Genie Chim, 95 (1966) 1393

[152] R. Krupiczka, Int. Chem. Eng, 7 (1967) 122

[153] N. Wakao, K. Kato, Effective Thermal Conductivity of Packed Beds. J. Chem. Eng. Japan, 2 (1969) 24-33

[154] N. Wakao, D. Vortmeyer, Chemical Engineering Science, 26 (1971) 1753

[155] N. Wakao, S. Kaguei, Heat and Mass Trensfer in Packed Beds. Gordon and Breach. New York (1982)

[156] D. Vortmeyer, Fortschr. Ber. VDI-Z Reihe, VDI-Verlag, Dusseldorf (1966)

[157] N. Wakao, Chemical Engineering Science, 28 (1973) 1117

[158] H.C. Hottel, Heat Trasmission edited by W. C. McAdams, 2nd edition, McGraw-Hill, New York, Ch.2 (1954)

[159] E. Tsotsas, E.U. Schlünder, Some remarks on channelling and on radial dispersion in packed beds, Chemical Engineering Science, *43* (1988) 1200-1203

[160] P. Zehner, E.U. Schlünder, Wärmeleitfähigkeit von Schüttungen bei mässigen Temperaturen, Chemie-Ing.-Techn. 42 (1970) 933-941

[161] D.E. Mears, Diagnostics criteria for heat transport limitations in fixed bed reactors. J. Catalysis, 20 (1971a) 127-131

[162] R.R. Hudgins, A general criterion for avoiding film diffusion control in heterogeneous catalytic reaction. Canad. J. Chem. Eng., 50 (1972) 427-430

[163] R B. Bird, W.E Stewart, E.N. Lightfoot, Transport Phenomena. Wiley, New York (1960)

[164] V. Gnielinski, Berechnung des warme und stoffaustauschs in durchstromten ruhenden schuttungen. VT "Verfahrenstechnik" 16 (1982) 36-39

[165] H. Martin, Chemical Engineering Science, 33 (1978) 913-919

[166] N. Wakao, S. Kaguei, T. Funazkri, Chemical Engineering Science, 34 (1979) 325

[167] G.S. Madia, G. Barbieri, E. Drioli, Theoretical and experimental analysis of methane steam reforming in a membrane reactor, Can. J. Chem. Eng. 77 (1999) 698-706

[168] J.M. Smith, Chemical Engineering Kinetic, McGraw-Hill, New York (1970)

[169] N. Itoh, A.M. Sathe, Hydrogen transport from gas to liquid phase through a palladium membrane, Journal of membrane science, 137 (1997) 251-259

[170] V. Comincioli, Analisi numerica, McGraw-Hill Libri Italia (1995)

[171] F. Cipitì, V. Recupero, Design of a CO preferential oxidation reactor for PEFC systems: A modelling approach, Chemical Engineering Journal, 146 (2009) 128–135

Figure Index

Table Index